Towards external injection in laser wakefield acceleration

Document Version:
Publisher's PDF, also known as Version of Record (includes final page, issue and volume numbers)

Please check the document version of this publication:

• A submitted manuscript is the version of the article upon submission and before peer-review. There can be important differences between the submitted version and the official published version of record. People interested in the research are advised to contact the author for the final version of the publication, or visit the DOI to the publisher's website.
• The final author version and the galley proof are versions of the publication after peer review.
• The final published version features the final layout of the paper including the volume, issue and page numbers.

[Link to publication](#)

Towards external injection in laser wakefield acceleration

PROEFSCHRIFT

ter verkrijging van de graad van doctor aan de
Technische Universiteit Eindhoven, op gezag van de
rector magnificus, prof.dr.ir. C.J. van Duijn, voor een
commissie aangewezen door het College voor
Promoties in het openbaar te verdedigen
op maandag 7 november 2011 om 16.00 uur

door

Xavier Stragier
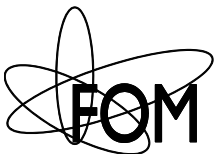
geboren te Roeselare, België

Dit proefschrift is goedgekeurd door de promotoren:

prof.dr. M.J. van der Wiel
en
prof.dr.ir. O.J. Luiten

Copromotor:
dr.ir. G.J.H. Brussaard

A catalogue record is available from the Eindhoven University of Technology Library

Contents

Chapter 1

General Introduction.

1.1 Charged particle acceleration and applications.

The first charged particle accelerators were designed and built nearly eighty years ago. Inspired by Ernest Rutherford, Cockcroft and Walton built the first high voltage accelerator to penetrate the nucleus of an atom in 1932 [1, 2]. Because high voltages are difficult and often dangerous to sustain, Ernest Orlando Lawrence sought a way to accelerate particles in small steps, sending them multiple times through the same accelerating structure using bending magnets. This device, based on the ideas of Rolf Wideröe [3], is known as the cyclotron [4, 5]. Many improvements and refinements have been developed since, but the general principles have remained basically the same, i.e. through generation, in vacuum, of high-voltage DC fields or electric fields that change synchronously with the motion of the particles.

Since these early experiments, the number of accelerators has known an explosive growth. Nowadays the estimated number of operational accelerators worldwide exceeds 30000. The applications of charged particle accelerators are based on the collision between the accelerated particle and material or on the radiation created by the accelerated particles. Charged particle accelerators have become indispensible not only for scientific research, but for many aspects of modern life in general. 44% of these accelerators are used for medical applications, such as diagnostics and radiotherapy. Another 41% is utilized for surface modification of materials and for ion implantation for the production of semi-conductors necessary for the electronics industry. 13% are for industrial applications and for biomedical and other research. Most industrial applications concern the sterilization of products (e.g. medical supplies and

packaging for food), crosslinking molecules, welding of metals, cargo screening and curing of materials (e.g. inks and coatings). The production of medical radioisotopes necessary for diagnostics and cancer treatment, accounts for 1%. Of these accelerators, only 1% exceeds a particle energy of 1 GeV; those are used for fundamental research [6-9]. Those high energy machines are used as a diagnostic tool for materials and to examine the fundamental structure of material and the universal laws of physics. These high energy machines have their large size (kilometer scale) and high cost (billion euro scale) in common.

Conventional charged particle accelerators use electrostatic (DC) or radio frequency (RF) electromagnetic fields in a vacuum environment to accelerate the charged particle to high velocity by increasing its kinetic energy [6, 10]. Dependent on the application, different particles with different charges get accelerated to specific kinetic energies, up to several trillions of electron volts (TeV). To accelerate to high kinetic energy, one can increase the electric field in the accelerating structure or enlarge its accelerating length. Unfortunately, all conventional accelerators are limited by a maximum electric field of typically ~100 MV/m [11, 12]. Exceeding this limit causes electrical breakdown in the wall of the accelerator structure. Therefore, a long accelerator structure is required to accelerate to high energy. An example of such an infrastructure is the 3.2 km long linear accelerator at the SLAC National Accelerator Laboratory at Stanford in the US which accelerates electrons and positrons up to 50 GeV. Another way to create a long accelerating structure is by connecting the entrance of the accelerator to its exit and creating a circular accelerator. The charged particles are kept in circular orbit with the use of external magnetic fields. This concept is applied in synchrotrons. In circular accelerators the charged particles lose energy due to radiation while being forced in circular motion (synchrotron radiation). The power of the radiation emitted by a charged particle depends on the radius of curvature of the trajectory and the kinetic energy of the particle. Some accelerators are specially built to produce synchrotron radiation and are used for fundamental research (e.g. the European Synchrotron Radiation Facility in Grenoble, France, the Diamond Light source at Rutherford Appleton Laboratory in Didcot, UK). Such facilities have a typical accelerator circumference between 0.5 km and 1 km. If charged particles with extremely high kinetic energy are required (TeV range), a low radius of curvature of the accelerating structure is necessary to keep energy loss due to radiation low and the magnetic fields realizable. This results in circular accelerators with a circumference of 6 kilometers (the Tevatron at Fermi National Accelerator Laboratory) and 27 km (the Large Hadron Collider at CERN), which are the largest accelerators on earth. Either way, by using conventional accelerator technology, particles with very high kinetic energy require kilometer scale facilities with the associated billion euro scale cost of the infrastructure.

One way to tackle the breakdown limit of 100 MV/m in conventional accelerators is by using local electric fields that can be generated inside a plasma to accelerate particles. A plasma is not limited by electrical breakdown and the electric field can be 3-4 orders of magnitude larger than in conventional accelerators [12, 13]. As a consequence, plasma accelerators may become a compact alternative for conventional RF-accelerators and may significantly reduce
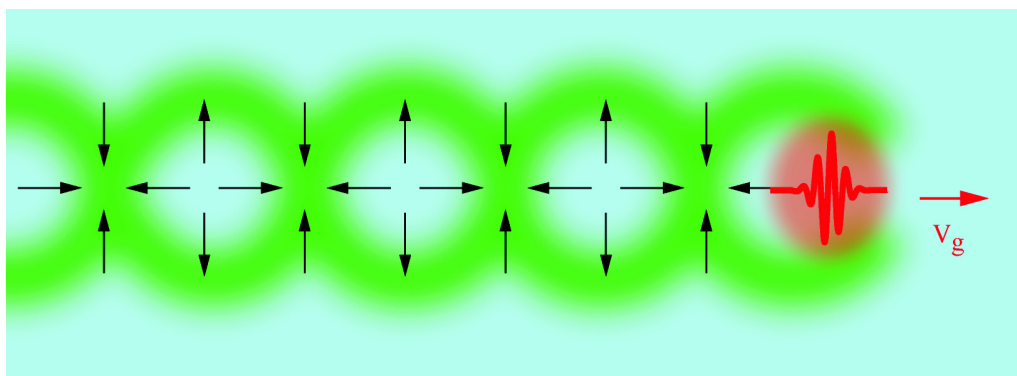
Figure 1.1: Illustation of a laser pulse (red) propagating through a plasma (blue) at group velocity v_g. The laser pulse creates an electron density modulation in its wake resulting in a plasma wave. Green areas indicate a high electron density. Black arrows indicate the electric fields and can be classified as longitudinal accelerating and decelerating and radial focusing and defocusing

the cost. Plasma accelerators also produce electron bunches with interesting properties for new applications. For instance plasma accelerators do not require complicated compression schemes to achieve extreme short electron bunch duration (order femtoseconds) which can be used to study fast dynamics in solid state material, molecules and chemical reactions.The accelerated electron bunches could be used to drive an undulator to create a table-top, tunable X-ray (free electron) laser [14, 15], which is considered the ultimate research tool to study fundamental properties of matter. The plasma accelerator also produces radiation directly, which can be used for different applications. Powerful coherent terahertz radiation is produced by electrons exiting the plasma [16] and short bursts of X-rays are generated by the betatron motion of electrons inside the plasma [17-21]. In principle, plasma accelerators can be driven by relativistic electron bunches (as was demonstrated at SLAC [22]), protons (proposed as a new experiment at CERN [23]) or by intense laser beams [12]. In this thesis only plasma accelerators driven by laser pulses are discussed.

1.2 Laser Wakefield Acceleration

Accelerators based on laser-plasma interaction were first described by Tajima and Dawson in 1979 [13]. In Laser Wakefield Accelerators (LWA) a plasma is used as an accelerating medium for charged particles. When a high intensity laser pulse is focused in a plasma, the ponderomotive force of the laser pulse will repel the electrons from the region of high laser intensity (see figure 1.1). The ions, that are much heavier than the electrons, remain quasi stationary and the result is a positively charged zone behind the laser pulse. Once the laser pulse passes, the Coulomb force pulls the electrons back which results in an oscillation of the electrons. This results in an electron density modulation in the wake of the laser pulse. The electrons oscillate around their equilibrium position and this leads to a (Langmuir) plasma wave

with a phase velocity equal to the group velocity of the laser pulse. The electric fields in the plasma wave have both radial and longitudinal components so that the plasma wave can act as an accelerating and focusing structure propagating at the group velocity of the laser pulse in the plasma. The electric fields in these plasma waves can be of the order of TV/m [12, 24]. The laser intensity needed to drive those plasma waves is in the TW-range; such intensities became possible with the introduction of Chirped Pulse Amplification [25] in 1985 and subsequent developments. Nowadays, TW laser systems up to ~200 TW are commercially available.

In order to accelerate electrons in a plasma accelerator, the electrons need to be trapped by the plasma wave. This can be achieved by so-called wave breaking, where the plasma wave is highly nonlinear due to an over-intense laser pulse. Hot background electrons in the plasma are then trapped and accelerated. In this case, the plasma is both the accelerating structure and the electron source. In this regime, successful acceleration experiments in a plasma were done by focusing a laser pulse with a power of several terawatt into a gas jet. This led to accelerated electrons with energies up to 100 MeV over a distance of a few millimeters [26-30]. The drawback of this method of injection of the hot background electrons in the plasma wave is that the moment of injection cannot be controlled accurately and injection continues while the laser propagates through the plasma. In the early experiments, this led to an energy spread of 100 % with rather poor shot-to-shot reproducibility.

Quasi mono-energetic electron bunches with an energy up to 200 MeV were produced by adapting the plasma density to the laser pulse [31, 32]. With a carefully chosen gas density it turned out to be possible to limit the wave breaking, and therefore the injection of electrons into the accelerating phase of the plasma wave, to just a fraction of the propagation distance of the laser in the plasma. Consequently, the energy spread was reduced to order 1%. Similar results were obtained using a channel with a preformed plasma density profile in the gas jet to guide the laser pulse over a longer distance [33].

To accelerate to higher energies a plasma density lower than $n_e \sim 10^{24}$ m^{-3} is needed. The group velocity of the laser pulse (and with that the phase velocity of the plasma wave) is higher at lower plasma density. Electrons can then be accelerated over a longer distance and to higher energies before they outrun the plasma wave (dephasing). In this regime, the laser pulse needs to be guided over a distance much larger than the Rayleigh length, so that the electrons can be accelerated over the complete dephasing length and gain maximum energy. By combining a 40 TW laser pulse with a slow capillary discharge plasma which guided the laser pulse over a distance of 3.3 cm, quasi mono-energetic electron bunches have been produced with an energy of 1 GeV [24]. Although the energy spread in those schemes is much better than in the earliest results, there is still a large shot-to-shot energy variation of the electron bunches produced.

For LWA to have a future in applications, electron bunches with high reproducibility, consistent energy and (low) energy spread are required. This is not the case with the previously mentioned schemes that are based on wave breaking, which is a highly nonlinear process. Small changes in parameters, such as laser intensity, the laser wave front and plasma density have a considerable influence on the output properties of the accelerated electron bunches. To stabilize

the electron bunch, a controlled injection of electrons in the plasma wave is necessary. One method to achieve this is by shooting a second, counter-propagating ultra short laser pulse with the same central wavelength and polarization into the plasma [34]. The first laser creates the wakefield and the second laser pulse injects the electrons in the plasma wave at the point where the two pulses overlap and briefly form a standing wave. Quasi mono-energetic electron bunches up to 200 MeV with tunable energy and high reproducibility have been made using this 'all-optical injection' method [36-37]. A second approach to injection is creating a density ramp in the plasma channel, which locally leads to wave breaking and thus to injection. Recent experiments have shown the feasibility of this scheme [38] and the results are comparable to optical injection. A third method that has recently been demonstrated is known as ionization triggered injection, in which a helium plasma was seeded with gas containing heavier atoms. This method mainly results in higher accelerated charge at lower electron bunch emittance [39, 40].

Although these injection schemes show promising results, the drawback is that the plasma still acts as accelerating medium and electron source so that one cannot be independently varied with respect to the other. An external electron source in combination with a plasma channel would therefore be most desirable. Since a radio frequency (RF) photogun is one of the brightest pulsed electron sources with high peak current [11], this is the best candidate to serve as external injector. An added advantage of using an external source for the injection of electrons is that acceleration becomes possible not only in nonlinear wakefields [15, 41-43], in which all experiments above are performed, but also in the linear regime with modest sub-10 TW lasers and a higher repetition rate [15, 44-48].

In the nonlinear regime, an electron bunch is injected in front of the laser pulse. If the velocity of the electron bunch is set to be lower than the group velocity of the laser pulse in the plasma, the laser will overtake the electron bunch inside the plasma. When the laser intensity is sufficiently strong, the electrons will be trapped, accelerated and compressed in the first trough of the plasma wave behind the laser pulse. After acceleration only one compressed bunch is produced.

In the linear regime, the electron bunch is injected shortly behind the laser pulse so it can occupy the first troughs, or 'buckets', of the plasma wave. It was believed that the injected bunch had to be shorter than the plasma wavelength (under 50 µm) with a synchronization between electron bunch and the plasma wave driving laser pulse even shorter than the plasma wavelength (sub 10 fs) in order to obtain accelerated electron bunches with low energy spread. It has been shown that in case of an injected bunch which exceeds the plasma wavelength, the wakefield will act as a chopper and transform the injected bunch in a train of accelerated sub-bunches [44, 48]. Because only the accelerating and focusing phase is suitable for acceleration, a maximum of ~10% of the initially injected charge can be accelerated. The trapping conditions are determined by the combination of wakefield amplitude and the injected electron energy. A higher injected electron energy (above the trapping threshold) will results in more accelerated charge but also in a higher energy spread. LWA with a slow capillary discharge plasma in the
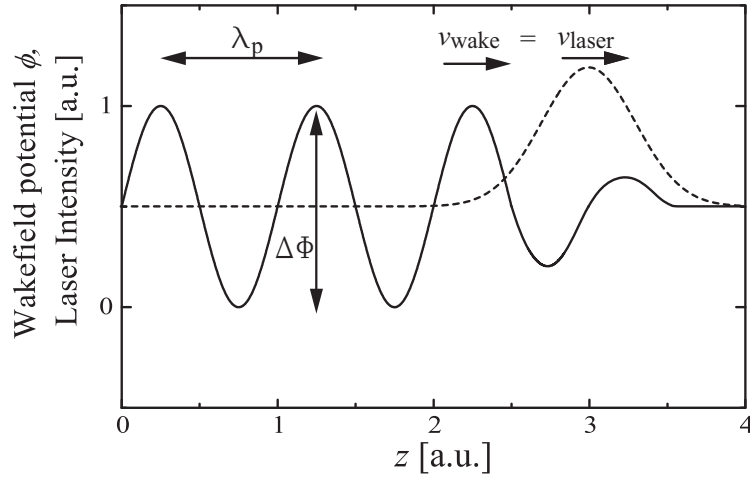
Figure 1.2: Illustration of a wakefield potential (solid line) of a linear plasma wave driven by a Gaussian laser pulse (dashed line).

linear regime and externally injected electron bunches from an RF-photogun is an approach in which most parameters are independently adjustable. This combined setup makes it possible to study the separate effects of source, plasma and laser on the accelerated electron bunch.

1.3 Trapping, energy gain and dephasing

Estimates of the minimum injection energy, the maximum energy gain and the so-called dephasing length (the optimum length of the plasma channel) can be gained from relatively straightforward 1D considerations. Electron density modulations in the plasma, generated by the laser pulse, result in a wakefield potential Φ on which electrons can gain kinetic energy and get accelerated. The relation between charge density in the plasma ρ and the associated wakefield potential is given by the Poisson equation $\nabla^2 \Phi = -\rho/\varepsilon_0$ with ε_0 the permittivity of free space. Figure 1.2 illustrates the wakefield potential in 1D (solid line) for a linear plasma wave with wavelength λ_p driven by a Gaussian laser pulse (dashed line). Plasma wave and laser pulse are propagating through the plasma at the same speed.

Figure 1.3 is used to deduce the minimum energy required for an electron to get trapped and accelerated by the plasma wave. An arbitrary (linear or nonlinear) wakefield potential Φ in the plasma is represented by the black line. Red arrows represent velocities in the frame of the laboratory (subscript l) while blue arrows represent the velocities in the frame of the wakefield potential and laser pulse (subscript w). The wakefield potential propagates at velocity v_p and the electrons at v_e. Due to relativistic effects, the relation between the wakefield potential in the frame of the laboratory Φ_l and the wakefield potential in the frame of the plasma wave Φ_w is given by $\Delta\Phi_w = \gamma_p \Delta\Phi_l$. Here $\Delta\Phi$ is defined as $\Phi_{max}-\Phi_{min}$ and $\gamma_p = \omega/\omega_p$ the Lorentz factor of the laser pulse in the plasma. ω is the angular frequency of the laser pulse and $\omega_p = (e^2 n_0/\varepsilon_0 m_e)^{1/2}$ the
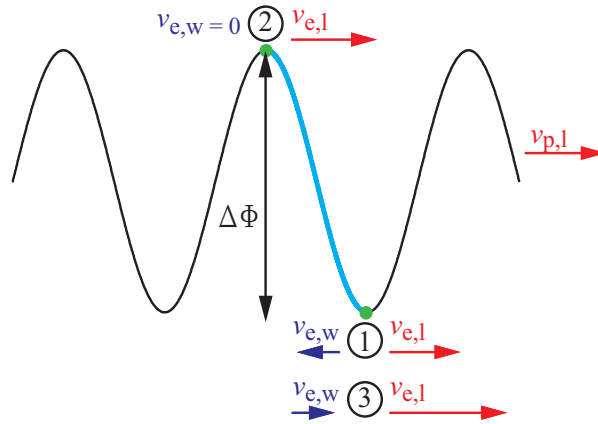
Figure 1.3: Illustration of the trapping mechanism of electrons in a plasma wave. Black line: wakefield potential in the plasma. Red arrows: velocities in the lab frame. Blue arrows: velocities in the frame of the plasma wave. 1: electron (green dots) injected at a trough of the wakefield potential (optimal injection phase), 2: electron slipped to the peak of the wakefield potential. 3: electron slipped back to the trough of the wakefield potential (point of maximum energy gain.)

angular plasma frequency with electron charge e, electron rest mass m_e and the electron density of the plasma n_0.

Electrons can gain a maximum amount of energy when they are injected in the trough of the wakefield potential (point 1 in Fig. 1.3). Injected electrons on this phase of the wakefield potential with a low kinetic energy will be overtaken by the wakefield. In the frame of the wakefield, this represents an electron velocity $v_\mathrm{e,w}$ in the negative direction. While being overtaken by the wakefield, the electron goes up the blue slope of the wakefield potential towards point 2 and gains potential energy (see Fig. 1.3). After the electron reaches a velocity $v_\mathrm{e,w} = 0$, the electron moves down the potential while being accelerated until it is at the trough of the potential well at point 3. At this point the electron has gained maximum kinetic energy. This is the dephasing point. The plasma channel has to be terminated at the point of dephasing to achieve maximum electron acceleration. If the plasma channel is not terminated, the electron goes up the opposite side of the potential well and gets decelerated, ultimately resulting in an oscillation within the wakefield potential.

The condition for the electron to get trapped by the plasma wave is determined by the requirement that the electron velocity $v_\mathrm{e,w}$ has to become zero (in the frame of the wakefield) at least at the top of the wakefield potential (point 2). If not, the electron goes over the top of the wakefield potential towards the next trough and gets decelerated.

The minimum kinetic energy for the electrons to get trapped can be estimated with the considerations above. If an electron is injected in the trough of the wakefield potential and has a velocity $v_\mathrm{e,w} = 0$ at the top of the wakefield potential, it has lost kinetic energy (directed to the left in the frame of the wakefield) to the amount:

$$\left(\gamma_\mathrm{e,w} - 1\right) = \frac{e\Delta\Phi_\mathrm{w}}{m_\mathrm{e}c^2} = \Delta\varphi_\mathrm{w} \tag{1.1}$$

with $\gamma_{e,w}$ the Lorentz factor of the electrons in the frame of the wakefield potential, c the speed of light in vacuum and φ_w the normalized electrostatic wakefield potential. The Lorentz factor is given by $\gamma = (1-v^2/c^2)^{-1/2}$. Transforming $\gamma_{e,w}$ to the laboratory frame and assuming $v_{p,l} \approx c$ and $\gamma_p \Delta \varphi_l \geq 1$ gives [12, 49]:

$$\gamma_{\min} \approx \frac{\Delta \varphi_l}{2} + \frac{1}{2\Delta \varphi_l}, \tag{1.2}$$

with φ_l the normalized electrostatic wakefield potential in the lab frame.

The maximum energy gain in a given wakefield can be estimated in a similar fashion. When a trapped electron in the wakefield potential passes the dephasing point, its velocity $v_{e,w}$ is equal to its velocity at injection in the frame of the plasma wave, but in the opposite direction. For an electron injected with Lorentz factor $\gamma_{\min}$ in the trough of the wakefield the maximum energy at the dephasing point is given by [12, 49]:

$$\gamma_{\max} \approx 2\gamma_p^2 \Delta \varphi_l \tag{1.3}$$

The dephasing length L_d is defined by the propagation distance in the lab frame of the electron injected in the trough of the wakefield with minimal trapping energy and the dephasing point (trajectory 1-2-3 in Fig. 1.3). The dephasing length is approximately [12, 49]:

$$L_d = \gamma_p^2 \frac{2\pi c}{\omega_p} \tag{1.4}$$

As an example: A 2 TW Gaussian laser with a central wavelength of 800 nm focused on a spot with a $1/e^2$ radius of 30 μm at the entrance of a plasma channel has a normalized vector potential, $a_0 = 0.26$. In the 1D approximation, this results in a linear plasma wave with a wakefield potential given by [12]:

$$\Delta \varphi_l = \frac{\pi}{4} a_0^2 \approx 0.05 \tag{1.5}$$

The injected electrons therefore require a minimum $\gamma \approx 10$ ($E_{\mathrm{kin}} \approx 5.5$ MeV) to get accelerated by the plasma (Eq.(1.2)). Using a plasma with an electron density of 0.7×10^{24} m^{-3} results in a maximum $\gamma \approx 250$ ($E_{\mathrm{kin}} \approx 125$ MeV) of the accelerated electrons at dephasing (Eq.(1.2)). The dephasing length for this plasma, according to Eq.(1.4) is ~ 10 mm.

Besides accelerating and decelerating fields, a 3D plasma wave also has focusing and defocusing fields. This highly complicates a straightforward calculation of the minimum injection energy and energy gain in the 3D case, especially for nonlinear plasma waves. Therefore one has to rely on simulations to determine the parameters of the injected and accelerated electrons. Extensive simulations have been done by Urbanus [44] and van Dijk [45-47] for electrons injected behind the laser pulse and by Khachatryan [41] and Luttikhof [43] for injection in front of the laser pulse.

When injecting electrons behind the laser pulse in a linear plasma wave, using the above mentioned laser and plasma parameters, a minimum $\gamma \approx 13$ is required at injection ($E_{kin} \approx 6$ MeV) and the maximum $\gamma \approx 180$ is achieved after acceleration ($E_{kin} \approx 90$ MeV) in a 70 mm long plasma channel.

1.4 Outline of this thesis

This thesis mainly deals with the design, construction and characterization of the various major components of the experimental setup as shown in figure 1.4 and is dominated by practical experimental work. The overall goal was to experimentally establish the suitability of the setup for LWA with external injection, in particular in terms of the crucial qualities of spot size, pointing stability and timing jitter of focused electron bunches and laser pulses at the entrance of the plasma channel.

Before the work described in this thesis commenced, Urbanus [44] and Van Dijk [44-47] had made a design for the setup, based on numerical simulations. It had been decided to construct a setup with a 2 TW laser pulse, to be injected into a 70 mm long plasma channel (creating linear wakefields) combined with a 6.7 MeV RF photogun The development of these three components (laser, plasma and RF accelerator) is described in chapters 2-5:

- Chapter 2: A ~15 GW laser system was available but had to be upgraded to a 2 TW laser system. This work was already underway, but most of the practical implementation and all the measurements and characterizations have been performed within the context of this thesis. Chapter 2 also describes the new compressor setup and the laser beam transport up to the entrance of the plasma channel. In figure 1.4 this is indicated by the red laser path, 'compressor box', 'off-axis parabola' and 'mirror'.

- Chapter 3: A plasma channel had been designed and tested at the FOM Institute for Plasma Physics 'Rijnhuizen' prior to the beginning of this PhD project. Based on this design, the plasma channel that was constructed and the diagnostics to characterize propagation of high power (TW level) laser pulses are described in chapter 3 (see also 'Plasma channel' in Fig 1.4).

- The RF photogun ('RF photogun' in Fig. 1.4) is described in chapter 4 and was already under construction at the beginning of this project. Standard measurements were done to check the accelerator after construction.

- Chapter 5 describes the beam line that was designed and constructed in the present project. The most important electron bunch properties are measured at the position of the entrance of the plasma channel, specifically the smallest focus spot and pointing stability, to determine the suitability of this accelerator as an injector for LWA.
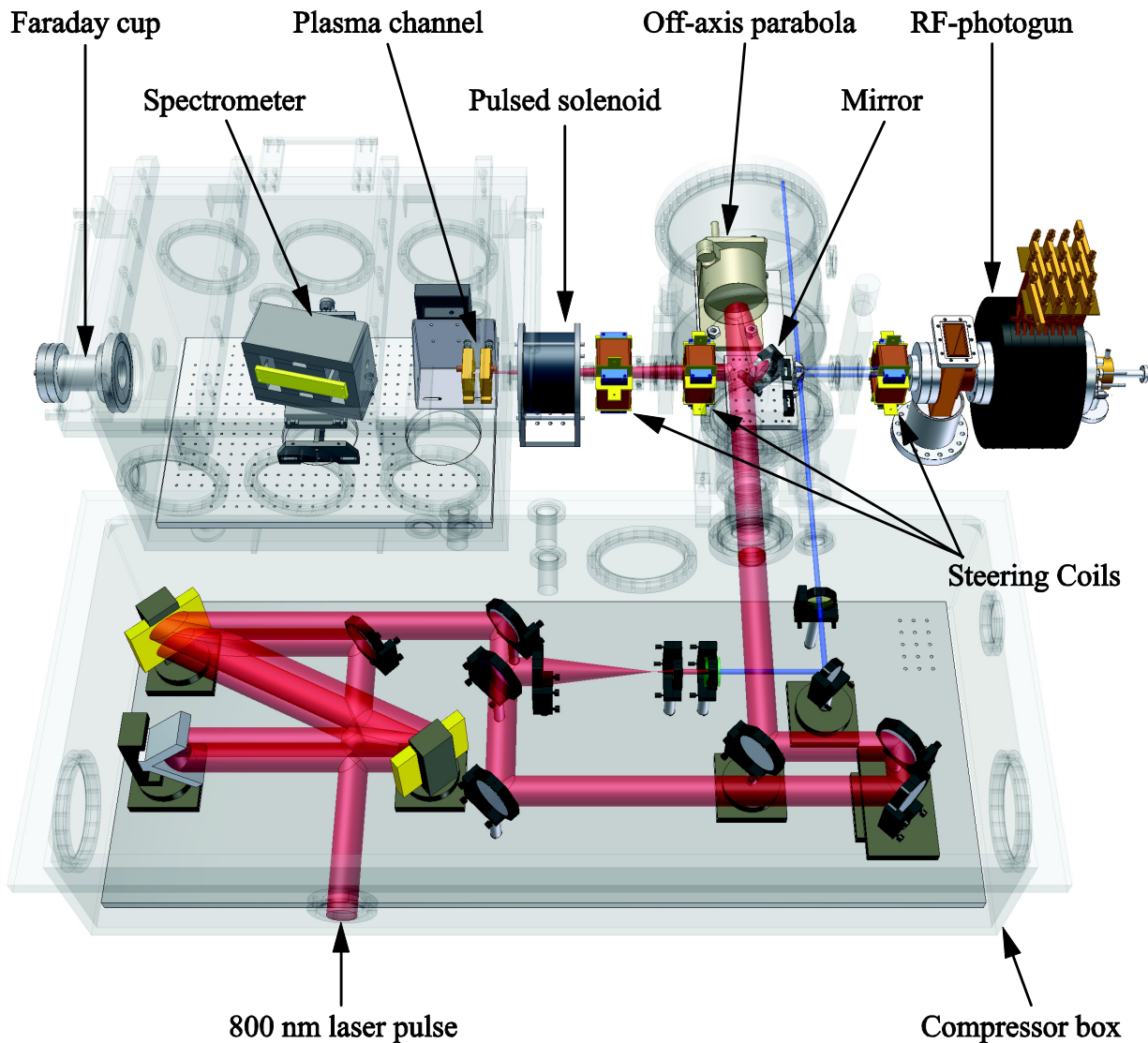
Figure 1.4: Illustration (Autodesk Inventor [50]) of the constructed experimental setup designed and developed at the TU/e for LWA in the linear regime with externally injected electrons from an RF-photogun.

As it turned out, it was not possible - in the time frame of this thesis work - to accelerate electrons beyond approximately 4 MeV. This is possibly due to contamination of the inside of the accelerator after failure of the RF window (which separates the vacuum part of the setup from the high pressure, SF_6-filled waveguides). However, the energy of the electron bunches produced (3.5-4 MeV) is very suitable for injection in front of the laser pulse, as described by, for example, Luttikhof [43]. To show the suitability of the present RF-photogun as electron injector in LWA in the non-linear regime, in front of the laser pulse, simulations have been done for the first time with the actually measured electron bunch properties of chapter 5 as input parameters, instead of the idealized properties used in earlier simulations. With our

simulations, presented in chapter 6, the effects of the laser power and plasma density on the expected charge, collection efficiency, energy and energy spread after plasma acceleration are examined.

In chapter 7, based on the findings in the different parts of the thesis, some general conclusions are drawn and several recommendations are made towards successful LWA experiments with externally injected electron bunches.

References

[1]   J. D. Cockcroft and E. T. S. Walton, *Experiments with High Velocity Positive* Ions, Proc. R. Soc. London A, Vol. 129, pp. 477-489, (1930).

[2]   J. D. Cockcroft and E. T. S. Walton, *Experiments with High Velocity Positive Ions. (I) Further Developments in the Method of Obtaining High Velocity Positive Ions*, Proc. R. Soc. London A, Vol. 136, pp. 619-630, (1932).

[3]   R. Wideröe, *Über ein neues Prinzip zur Herstellung hoher Spannungen,* Archiv für Elektrotechnik, Vol. 21, Issue 4, pp. 387-406, (1928).

[4]   E. O. Lawrence and N. E. Edlefsen, *On the production of high speed protons*, Science, Vol. 72, pp. 376-378, (1930).

[5]   E. O. Lawrence and M. S. Livingston, *The Production of High Speed Protons Without the Use of High Voltages*, Phys. Rev., Vol. 38, Issue 4, pp. 834–834, (1931).

[6]   W . Schaft, *Particle accelerators and their uses (Part 1 and 2,* Harwood academic publishers, ISBN: 3-7186-0318-7, (1986).

[7]   C. S. Nunan, *Present and Future Applications of Industrial Accelerators,* Proceedings of Fermilab industrial affiliates roundtable on Applications of Accelerators, Batavia, Illinois : s.n., pp 004, (26-27 May 1989).

[8]   T. Feder, *W. A. Barletta, in: Accelerator school travels university circuit,* Physics Today, Vol. 63, Issue 2, p. 20, (2010).

[9]   R. W. Hamm and M. E. Hamm, *The beam business: Accelerators in industry*, Physics Today, Vol. 64, Issue 6, p. 46, (2011).

[10] K. S. Krane, *Introductory Nuclear Physics,* John Wiley and Sons, ISBN: 0.471-80553-X. (1988).

[11] R. Akre, D. Dowell, P. Emma, J. Frisch, S. Gilevich, G. Hays, Ph. Hering, R. Iverson, C. Limborg-Deprey, H. Loos, A. Miahnahri, J. Schmerge, J. Turner, J. Welch, W. White, and J. Wu, *Commisioning the Linac Coherent Light Source*, Phys. Rev. ST Accel. Beams, Vol. 11, 030703, (2008).

[12] E. Esarey, P. Sprangle, J. Krall, A. Ting, *Overview of Plasma-Based Accelerator Concepts,* IEEE Trans. on Plasma Science, Vol. 24, Issue 2, (1996).

[13] T. Tajima and J. M. Dawson, *Laser Electron Accelerator*, Phys. Rev. Lett., Vol. 43, pp. 267-270, (1979).

[14] K. Nakajima, *Compact X-ray sources: Towards a table-top free-electron laser,* Nature Physics, Vol. 4, Issue 2, pp. 92-93, (2008).

[15] M. J. van der Wiel, O. J. Luiten, G. J. H. Brussaard, S. B. van der Geer, W. H. Urbanus, W. van Dijk and Th. van Oudheusden, *Laser wakefield acceleration: the injection issue. Overview and latest results,* Phil. Trans. R. Soc. A, Vol. 364, p. 679, (2006).

[16] J. Tilborg *Coherent terahertz radiation from laser-wakefield-accelerated electron beams,* PhD thesis, Eindhoven University of Technology, ISBN: 978-90-386-2521-8, (2006).

[17] A. Rousse, K. T. Phuoc, R. Shah, A. Pukhov, E. Lefebvre, V. Malka, S.Kiselev, F. Burgy, J. P. Rousseau, D. Umstadter, and D. Hulin, *Production of a keV X-Ray Beam from Synchrotron Radiation in Relativistic Laser-Plasma Interaction.*, Phys. Rev. Lett., Vol. 93, 135005, (2004).

[18] K. T. Phuoc, S. Corde, R. Shah, F. Albert, R. Fitour, J.-P. Rousseau, F. Burgy, B. Mercier, and A. Rousse *Imaging Electron Trajectories in a Laser-Wakefield Cavity Using Betatron X-Ray Radiation,.* Phys. Rev. Lett., Vol. 97, 225002, (2006).

[19] F. Dorchies, F. Blasco, C. Bonté, T. Caillaud, C. Fourment, and O. Peyrusse, *Observation of Subpicosecond X-Ray Emission from Laser-Cluster Interactio*n, Phys. Rev. Lett., Vol. 100, 205002, (2008).

[20] S. Kneip, S. R. Nagel, C. Bellei, N. Bourgeois, A. E. Dangor, A. Gopal, R. Heathcote, S. P. D. Mangles, J. R. Marquès, A. Maksimchuk, P. M. Nilson, K. T. Phuoc, S. Reed, M. Tzoufras, F. S. Tsung, L. Willingale, W. B. Mori, A. Rousse, K. Krushelnick and Z. Najmudin, *Observation of Synchrotron Radiation from Electrons Accelerated in a Petawatt-Laser-Generated Plasma Cavity*, Phys. Rev. Lett., Vol. 100, 105006, (2008).

[21] H.-P. Schlenvoigt, K. Haupt, A. Debus, F. Budde, O. Jäckel, S. Pfotenhauer, H. Schwoerer, E. Rohwer, J. G. Gallacher, E. Brunetti, R. P. Shanks, S. M. Wiggins & D. A. Jaroszynski, *A compact synchrotron radiation source driven by a laser-plasma wakefield accelerator,* Nature Physics, Vol. 4, Issue 2, pp. 130-133, (2008).

[22] I. Blumenfeld, C. E. Clayton, F.-J. Decker, M. J. Hogan, C. Huang, R. Ischebeck, R. Iverson, C. Joshi, T. Katsouleas, N. Kirby, W. Lu, K. A. Marsh, W. B. Mori, P. Muggli, E. Oz, R. H. Siemann, D. Walz and M. Zhou, *Energy doubling of 42 GeV electrons in a metre-scale plasma wakefield accelerator*, Nature, Vol. 445, pp. 741-744, (2007).

[23] A. Caldwell, K. Lotov, A. Pukhov and F. Simon, *Proton-driven plasma-wakefield acceleration*, Nature Physics, Vol. 5, Issue 5, pp. 363-367, (2009).

[24] W. P. Leemans, B. Nagler, A. J. Gonsalves, Cs. Tóth, K. Nakamura, C. G. R. Geddes, E. Esarey, C. B. Schroeder, and S. M. Hooker, Nature physics, Vol. 2, p. 696, (2006).

[25] D. Strickland and G. Mourou, *Compression of amplified chirped pulses*, optics communications, Vol. 56, Issue 3, pp. 219-221, (1985).

[26] A. Modena, Z. Najmudin, A. E. Dangor, C. E. Clayton, K. A. Marsh, C. Joshi, V. Malka, C. B. Darrow, C. Danson, D. Neely and F. N. Walsh, *Electron acceleration from the breaking of relativistic plasma waves*, Nature, Vol. 377, pp. 606 – 608, (1995).

[27] R. Wagner, S.-Y. Chen, A. Maksimchuk, and D. Umstadter, *Electron Acceleration by a Laser Wakefield in a Relativistically Self-Guided Channel*, Phys. Rev. Lett., Vol. 78, pp. 3125–3128, (1997).

[28] A. Ting, C. I. Moore, K. Krushelnick, C. Manka, E. Esarey, P. Sprangle, R. Hubbard, H. R. Burris, R. Fischer, and M. Baine, *Plasma wakefield generation and electron acceleration in a self-modulated laser wakefield accelerator experiment*, Phys. Plasmas, Vol. 4, p. 1889, (1997)

[29] V. Malka, J. Faure, J. R. Marquès, F. Amiranoff, J. P. Rousseau, S. Ranc, J. P. Chambaret, Z. Najmudin, B. Walton, P. Mora, and A. Solodov, *Characterization of electron beams produced by ultrashort (30 fs) laser pulses*, Phys. Plasmas , Vol. 8, p. 2605, (2001).

[30] V. Malka, S. Fritzler, E. Lefebvre, M. M. Aleonard, F. Burgy, J. P. Chambaret, J. F. Chemin, K. Krushelnick, G. Malka, S. P. D. Mangles, Z. Najmudin, M. Pittman, J. P. Rousseau, J. N. Scheurer, B. Walton, A. E. Dangor, *Electron acceleration by a wake field forced by an intense ultrashort laser pulse*, Science, Vol. 298, pp. 1596-1600, (2002).

[31] S. P. D. Mangles, C. D. Murphy, Z. Najmudin, A. G. R. Thomas, J. L. Collier, A. E. Dangor, E. J. Divall, P. S. Foster, J. G. Gallacher, C. J. Hooker, D. A. Jaroszynski, A. J. Langley, W. B. Mori, P. A. Norreys, F. S. Tsung, R. Viskup, B. R. Walton, and K. Krushelnick, *Monoenergetic beams of relativistic electrons from intense laser-plasma interactions*, Nature, Vol. 431, p. 535, (2004).

[32] J. Faure, Y. Glinec, A. Pukhov, S. Kiselev, S. Gordienko, E. Lefebvre, J.-P. Rousseau, F. Burgy, and V. Malka, *A laser-plasma accelerator producing monoenergetic electron beam*, Nature, Vol. 431, p. 541, (2004).

[33] C. G. R. Geddes, Cs. Toth, J. van Tilborg, E. Esarey, C. B. Schroeder, D. Bruhwiler, C. Nieter, J. Cary, and W. P. Leemans, *High-quality electron beams from a laser wakefield accelerator using plasma-channel guiding*, Nature, Vol. 431, p. 538, (2004).

[34] E. Esarey, R. F. Hubbard, W. P. Leemans, A. Ting, and P. Sprangle, *Electron Injection into Plasma Wakefields by Colliding Laser Pulses*, Phys. Rev. Lett., Vol. 79, pp. 2682–2685, (1997)

[35] J. Faure, C. Rechatin, A. Norlin, A. Lifschitz, Y. Glinec and V. Malka, *Controlled injection and acceleration of electrons in plasma wakefield by colliding laser pulses*, Nature, Vol. 444, p. 737, (2006).

[36] C. Rechatin, J. Faure, A. Ben-Ismail, J. Lim, R. Fitour, A. Specka, H. Videau, A. Tafzi, F. Burgy, and V. Malka, *Controlling the Phase-Space Volume of Injected Electrons in a Laser-Plasma Accelerator*, Phys. Rev. Lett., Vol. 102, 164801, (2009).

[37] H. Kotaki, I. Daito, M. Kando, Y. Hayashi, K. Kawase, T. Kameshima, et al., *Electron Optical Injection with Head-On and Countercrossing Colliding Laser Pulses*, Phys. Rev. Lett., Vol. 103, 194803, (2009).

[38] J. Faure, C. Rechatin, O. Lundh, L. Ammoura, and V. Malka, *Injection and acceleration of quasimonoenergetic relativistic electron beams using density gradients at the edges of a plasma channel*, Phys. Plasmas , Vol. 17, 083107, (2010).

[39] A. Pak, K. A. Marsh, S. F. Martins, W. Lu, W. B. Mori, and C. Joshi, *Injection and Trapping of Tunnel-Ionized Electrons into Laser-Produced Wakes*, Phys. Rev. Lett., Vol. 104, 025003, (2010).

[40] C. McGuffey, A.G.R. Thomas, W. Schumaker, T. Matsuoka, V. Chvykov, F. J. Dollar, G. Kalintchenko, V. Yanovsky,V.Yu. Bychenkov,I.V. Glazyrin and A.V. Karpeev, *Ionization Induced Trapping in a Laser Wakefield Accelerator*, Phys. Rev. Lett., Vol. 104, 025004, (2010).

[41] A. G. Khachatryan, F. A. van Goor, K.-J. Boller, A. J. W. Reitsma and D. A. Jaroszynski, *Extremely short relativistic-electron-bunch generation in the laser wakefield via novel bunch injection scheme*, Phys. Rev. ST Accel. Beams, Vol. 7, 121301 , (2004).

[42] A. Irman, M. J. H. Luttikhof, A. G. Khachatryan, F. A. van Goor, J. W. J. Verschuur, H. M. J. Bastiaens, and K.-J. Boller, *Design and simulation of laser wakefield acceleration with external electron bunch injection in front of the laser pulse*, J. Appl. Phys., Vol. 102., 024513, (2007).

[43] M. J. H. Luttikhof, *Theoretical investigation of external injection schemes for laser wakefield acceleration*, PhD thesis University of Twente, ISBN: 978-90-365-3071-2, (2010).

[44] W. H. Urbanus, W. van Dijk, S. B. van der Geer, G. J. H. Brussaard, and M. J. van der Wiel, *Front-to-end simulations of the design of a laser wakefield accelerator with external injection*, J. Appl. Phys., Vol. 99, 114501, (2006).

[45] W. van Dijk, S. B. van der Geer, M. J. van der Wiel, and G. J. H. Brussaard, *Parameter study of acceleration of externally injected electrons in the linear laser wakefield regime*, Phys. Plasmas, Vol. 15, 093102, (2008).

[46] W. van Dijk, J. M. Corstens, S. B. van der Geer, M. J. van der Wiel, and G. J. H. Brussaard, *Effects of timing and stability on laser wakefield acceleration using external injection*, Phys. Rev. ST Accel. Beams, Vol. 12, 051304, (2009).

[47] W. van. Dijk, *Simulations and Experiments on External Injection for Laser Wakefield Acceleration*, PhD thesis, Einhoven University of Technology, ISBN: 978-90-386-2316-0, (2010).

[48] D. F. Gordon, R. F. Hubbard, J. H. Cooley, B. Hafizi, A. Ting, and P. Sprangle, *Quasimonoenergetic electrons from unphased injection into channel guided laser wakefield accelerators*, Phys. Rev. E, Vol. 71, 026404, (2005).

[49] E. Esarey and M. Pilloff, *Trapping and acceleration in nonlinear plasma waves*, Phys. Plasmas, Vol. 2, p. 1432, (1992).

[50] http://usa.autodesk.com/autodesk-inventor

Chapter 2

The Laser System.

2.1 Introduction

An ultra-short terawatt laser pulse focused into a spot of tens of micrometer in a plasma and guided through the plasma is necessary to generate a plasma wave on which externally injected electrons can be accelerated. The plasma density of the planned LWA experiments with external injection of electrons is typically around ~10^{24} m^{-3}. The $1/e^2$ radius of the laser spot for laser guiding in such a plasma is around 20-50 μm [1-4]. When electrons with energy of a few MeV are injected in front of the laser pulse, at least a 10 TW laser pulse is required to accelerate the injected electrons in the plasma [1, 2, 5, 6]. In this case, the laser creates a (slightly) non-linear plasma wave. Accelerating electrons in linear plasma waves is already possible with a more modest 2 TW laser system. In the linear plasma waves, the electrons are injected behind the laser pulse. However, for the linear regime, the injected electrons need a kinetic energy over 6 MeV to get trapped and accelerated [3, 4, 7]. At the moment of writing of this thesis, the RF-photogun can not yet deliver the 6 MeV electrons necessary to trap and accelerate electrons in these linear wakefields. Further conditioning of the RF-photogun is therefore needed (see also Chapters 4 and 5).

This chapter describes the construction and properties of the laser system that can produce 3 TW laser pulses at a repetition rate of 10 Hz. Furthermore the focus spot of the laser pulse at the entrance of the plasma channel and its pointing stability are examined. Simulations and measurements of the laser energy and spectral narrowing are examined. Also the generation of the laser pulses necessary to photo-emit the electrons from the cathode plate of the
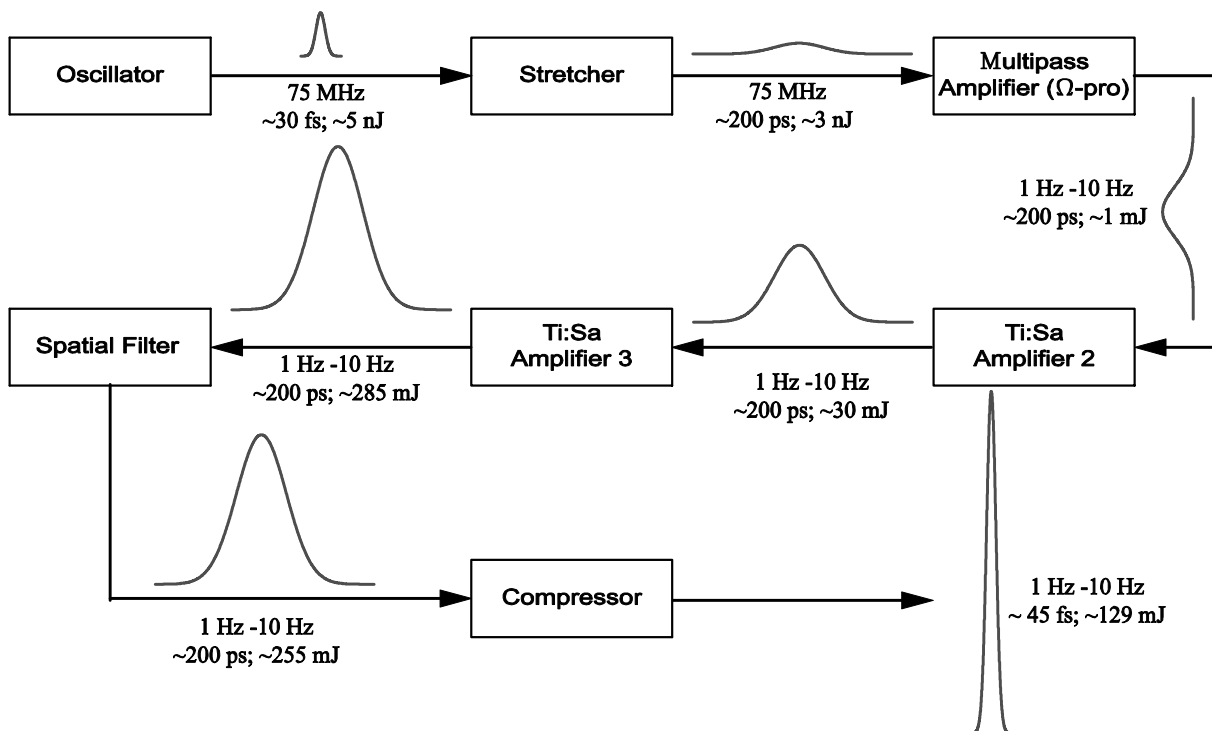
Figure 2.1: Principle of chirped pulse amplification applied to the used laser setup.

RF-photogun is presented. At the time the construction of the laser amplifier was started, the commercially built systems were not yet very reliable, requiring frequent service and maintenance. Because beams at different wavelengths are required, with very specific demands on the beam size and stability, it was decided to build the laser amplifier in-house.

2.2 Overview of the TW laser system

2.2.1 Ultra short laser pulse amplification

The generation of ultra-short high power terawatt laser pulses is a prerequisite to drive a plasma wave suitable for acceleration and became possible with the introduction of the chirped pulse amplification [8]. The principle of chirped pulse amplification applied to the laser setup used can be seen in Figure 2.1. A Titanium:Sapphire (Ti:Sa) modelocked Femtosource oscillator (Femtolaser Productions GmbH) produces laser pulses of ~25 fs (FWHM) with an energy of ~5nJ at a repetition rate of 75 MHz and a central wavelength of 800 nm. These pulses of ~ 150 kW need to be amplified to reach the desired power of ~ 3 TW. Because such a high intensity would damage the amplifier crystals, the laser pulses first need to be stretched to a length of 200 ps.

The stretcher design is based on the design proposed by Banks [9] with two spherical mirrors and one grating. The stretcher introduces a path length difference dependent on the wavelength. The lower frequencies in the laser pulse propagate along a shorter path than the higher frequencies, which results in a stretched pulse of 200 ps. The advantage of this system over the use of two gratings as stretcher is that it is relatively insensitive to alignment errors. Two thirds of the initial laser energy is lost in the stretcher, due to the reflectivity of the gratings (~90% at each of the four reflections) and in part because of the limited bandwidth of the setup due to the finite size of the optical components. A more thorough description and alignment procedure of the stretcher can be found in the report by De Milliano [10].

The stretched pulses are sent to the 'Omega Pro' (Ω-pro), a 9-pass amplifier (Femtolaser Productions GmbH). The original internal stretcher and compressor in the Omega Pro multi-pass amplifier are bypassed as this stretcher does not sufficiently stretch the laser pulse. The pulses pass through a Ti:Sa crystal which is pumped by a frequency doubled Nd:YLF (Neodymium-doped yttrium lithium fluoride) pump laser type 621-D (Thomson-csf). The pump laser produces laser pulses at 527nm with a pulse length of 500 ns and energy of ~ 8 mJ per pulse at a repetition frequency of 1 kHz. In the Ω-pro, the laser pulses first pass 4 times through the pumped crystal. This results in amplification of almost a factor 10^3. A Pockell's cell selects pulses at an adjustable repetition frequency between 1 Hz and 1 kHz. The selected pulse passes five more times through the Ti:Sa crystal, which results in a 800 nm pulse with an energy of ~1mJ per pulse at a frequency between 1 Hz and 1 kHz. A complete overview of the Omega Pro multi-pass amplifier can be found in the report by Barros [11, 12].

The 800 nm laser pulses need further amplification to achieve the desired energy. On a second optical table, the pulse passes through two additional, separately pumped Ti:Sa crystals (Ti:Sa amplifier '2' and '3', see section 2.2.2). After the last amplification stage, the laser pulse passes through a spatial filter to achieve a smooth, Gaussian radial intensity profile (section 2.2.3). Finally the 800 nm pulses are compressed to pulses of ~ 45 fs with energy of 130 mJ, resulting in a laser pulse of 2.9 TW (section 2.2.4) which is sufficient for laser wakefield experiments in the linear regime. The second and third amplification stage, the spatial filter and the compressor are new, in-house built, and are therefore described and discussed in more detail in the next sections.

2.2.2 Second and third amplifier stages

The 800 nm laser pulses coming from the Ω-pro multi-pass amplifier require further amplification and are sent to a second optical table, shown schematically in Figure 2.2. All mirrors on this optical table used for the transportation of the 800 nm pulse are dielectric mirrors made by CVI Melles Griot (type TLMB-800-45) because of their high damage threshold for ultra short high intensity 800 nm and high reflectivity for p-polarized laser pulses.
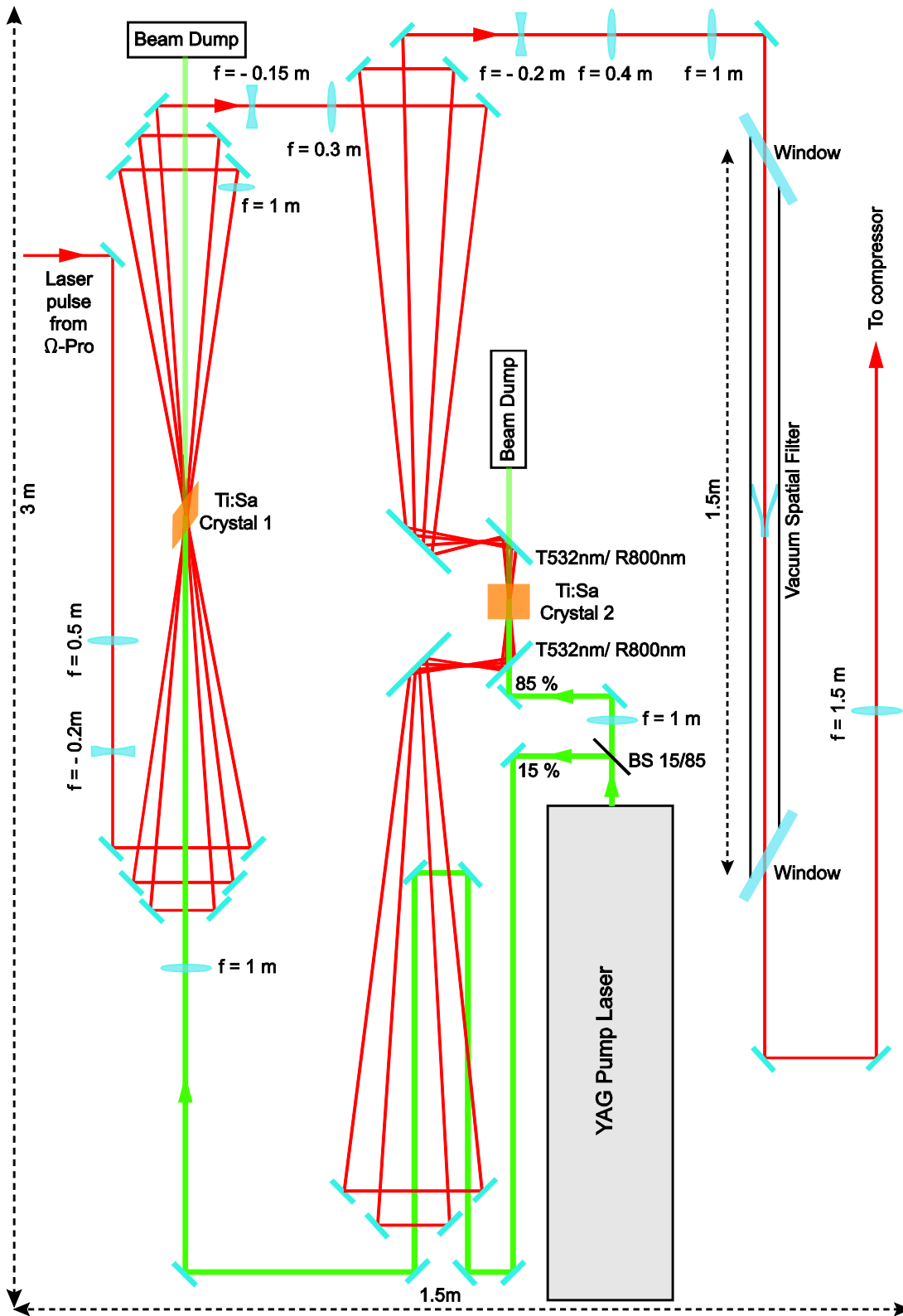
Figure 2.2: Optical table with second and third amplifying Ti:Sa crystals and spatial filter. Ti:Sa crystal are pumped by a Nd:YAG laser (green laser path). Red laser path are the 800 nm laser pulses.

A frequency doubled Nd:YAG (neodymium-doped yttrium aluminum garnet; Nd:Y$_3$Al$_5$O$_{12}$) pump laser type SAGA 230 (Thomson-csf) produces 532 nm laser pulses at a repetition frequency of 10 Hz with an energy of ~ 1 J and a pulse length of 6-8 ns. A beam splitter reflects 15% of the pump laser energy toward the second amplification crystal and transmits 85% toward the third amplification crystal. The pump laser has a flat-top transverse intensity profile and is imaged to a spot of 3 mm on the second Ti:Sa crystal, using a lens with a focal length of 1 m. The part of the pump laser energy which is not absorbed by the crystals is absorbed in a beam dump. The second crystal has a diameter of 10 mm, a length of 10 mm and the entrance and exit planes of the crystal are cut at Brewster angle (60º with respect to the central axis), to optimize laser transmission.

The radius of the 800 nm laser pulse coming from the Ω-pro is reduced to a $1/e^2$ radius of 1.7 mm, using two lenses with focal lengths of 0.5 m and -0.2 m, respectively. The laser pulse passes five times through the second crystal. For optimal amplification, a third lens, with a focal distance of 1 m, was placed between pass one and two. The exact position of the three lenses was designed and later optimized experimentally, to image the plane of the crystal of the Ω-pro on the plane of the second amplifier crystal in the fifth pass, while keeping the beam small through all five passes. After five passes, the energy of the laser pulse is ~ 33 mJ per pulse. These pulses are sent to the third Ti:Sa amplifying crystal.

The third Ti:Sa crystal is cylindrical with a length of 22 mm, a diameter of 20 mm. Because crystals with Brewster angle end-configurations require more crystal volume during production and are thus more expensive, this crystal has anti-reflection coating (for 532 nm and 800 nm pulses) at the entrance and exit planes. The intensity profile of the pump-laser pulses is flat top, with a diameter of 13 mm. For optimum amplification (see section 2.5), the beam is focused using a lens with a focal distance of 1 m, placed 30 cm in front of the crystal. The pump laser beam then has a diameter of 9 mm inside the crystal. Imaging the exit of the pump laser onto the crystal was not deemed necessary in this case, because of the relatively short distances between the laser exit, the lens and the crystal. The profile is still more or less flat-top in the crystal. The 800 nm pulses after the second amplification crystal are expanded to a $1/e^2$ radius of 5 mm and are slightly divergent, in order not to damage the third crystal. After 4 passes through the third crystal the final energy of the 800 nm pulses is 285 mJ per pulse.

2.2.3 Spatial filter

The transverse laser profile after final amplification can be seen in Figure 2.3.b. The laser pulse shows spots with high spatial frequencies. Although we are aiming for a Gaussian laser pulse, this profile is mainly caused by the semi flat-top profile of the pump laser at the third crystal in combination with the different angles that the paths of the 800 nm laser pulses make when passing through the crystal.
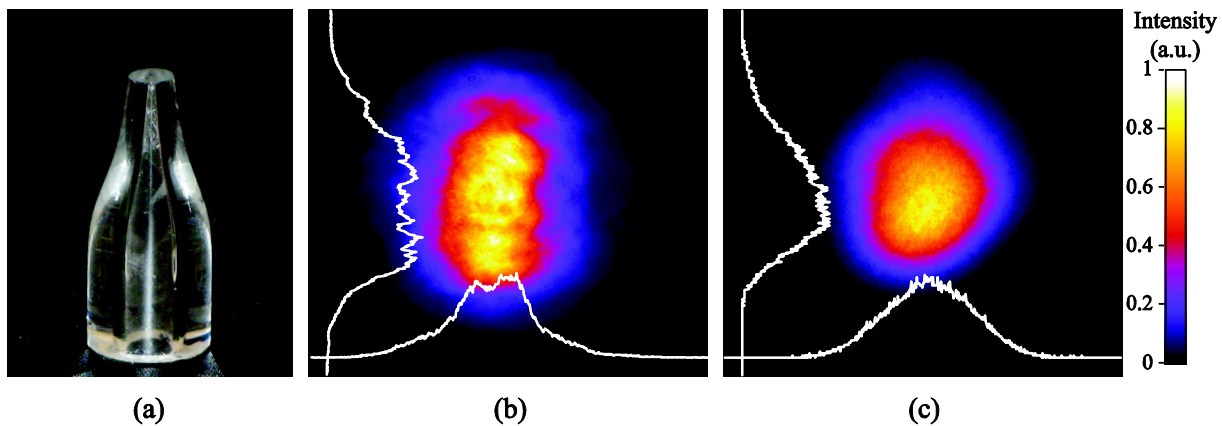
Figure 2.3: (a) Picture of the pinhole used in the spatial filter. (b) Transverse laser pulse profile 1 m in front of the spatial filter and (c) 1 m after the exit of the spatial filter.

After compression, these high spatial frequencies will evolve to spots with very high intensity which can damage the optical components of the laser system. Therefore the laser pulse has to be spatially filtered to create a smooth transverse Gaussian intensity profile before it is sent to the compressor. This is commonly done by focusing the laser beam through an aperture or 'pinhole' in a metal plate. The aperture has the same dimensions as the waist of the laser. The zero-order Gaussian mode of the beam will pass through the aperture. The higher order modes will be focused in front or behind the aperture and will be blocked.

The place of the spatial filter in the setup is found in Figure 2.2. The laser pulse is expanded after the last pass through the Ti:Sa crystal and focused by a 1 m lens through the pinhole. The pinhole has to be placed in vacuum because of the high intensity of the laser pulses near focus. Focusing the laser in air leads to ionization of the molecules close to focus resulting in an unusable laser pulse. The vacuum windows transmitting the laser pulse are placed at a distance of ~ 750 mm from the pinhole to keep the intensity of the laser pulse on the windows low. The windows are placed at Brewster angle to minimize reflection. The pinhole with a diameter of 150 μm is made of BK7 glass in the shape of a bottleneck, made at the TU/e glass workshop. A photograph of one of these pinholes is shown in Figure 2.3.a. The part of the laser beam hitting the glass around the pinhole will be reflected and refracted out of the laser beam, leaving a smooth Gaussian laser pulse after the pinhole. A non-transparent pinhole would be destroyed by the high intensity focus of the laser pulse. The transverse laser profile after the spatial filter is shown Figure 2.3.c. Approximately 10% of the initial laser energy gets lost during the spatial filtering process, resulting in a laser pulse with a fairly smooth transverse Gaussian laser profile and an energy of ~255 mJ per pulse. Finally, the laser pulse is collimated with a FWHM radius of 1 cm by a lens with a focal length of 1.5 m and sent to the compressor.

2.2.4 Vacuum compressor.

The laser pulse coming from the amplifier and spatial filter has to be compressed again to 50 fs before it is focused at the entrance of the plasma channel. Compression results in a maximum laser pulse of ~3 TW. This is sufficient to perform LWA experiments in the linear regime, with electron injection behind the laser pulse.

To keep the laser pulse stable, the compressor is operated in vacuum. The total index of refraction of an isotropic medium is dependent on the intensity of the laser and is given by: $n = n_0 + n_2 I(t,r)$, with I the intensity of the laser pulse as function of radius r and time t. n_0 is the refractive index and n_2 is the nonlinear refractive index. At high laser intensities, like those of TW laser pulses, this nonlinear effect cannot be neglected. The higher refractive index at the centre of the laser pulse in the medium will act as a focusing lens (*Kerr-Lens effect*) and cause self-phase modulation [13]. To limit these effects, the pressure inside the compressor box has to be lower than 1 mbar. Because the compressor box is also directly connected to the RF-photogun, the compressor was operated at ~10^{-6} mbar.

The p-polarized 800 nm laser pulse with a length of 200 ps and an energy of 255 mJ coming from the spatial filter enters the vacuum compressor box through a window (see figure 2.4). As the laser pulse is still stretched, its intensity is sufficiently low to avoid a significant Kerr-Lens effect in the window. The diameter (FWHM) of the laser pulse is 1 cm. A motorized mirror MM1 reflects the laser pulse to diffraction grating 1. The angle θ_i between the incoming laser pulse and the normal to the surface of the grating is 46.5°. The gratings have a 1500 lines/mm pattern, gold coated. A fraction of ~ 90% of the energy is reflected in the -1 order reflection. The -1 order reflection of the central wavelength (800 nm) makes an angle $\theta_m = -28.4°$ with the normal to the surface of the grating according to [14]:

$$a(\sin\theta_m - \sin\theta_i) = m\lambda \qquad (2.1)$$

with m the order of reflection, λ the wavelength and a the spacing between the lines on the grating. As the laser pulse spectrum consist of frequencies between 750 nm and 850 nm (see figure 2.9), the wavelengths are reflected under an angle between -23.6° and -33.4° with the normal to the surface of the grating. The laser pulse is reflected to grating 2 which is placed parallel to grating 1. After the second grating, the pulses are sent to a stepping mirror to separate the incoming and outgoing paths. After reflections on the second and first gratings, the pulses exit the compressor parallel to the incoming path. The separation between the gratings determines the path length for different wavelengths and compresses the stretched laser pulse [10]. The laser pulses reflect 4 times off a grating with a reflection of ~ 90%, resulting in a maximum efficiency of ~ 65%. The compressed laser pulse is sent on to a variable delay line and finally toward motorized mirror MM3 which reflects the laser pulse out of the compressor box towards the off-axis parabola (see Fig. 1.2). At the exit of the compressor box the energy of the 800 nm pulse was measured to be 129±8 mJ. This pulse is focused by the off-axis parabola at the entrance of the plasma channel and will be used to generate the plasma wave.
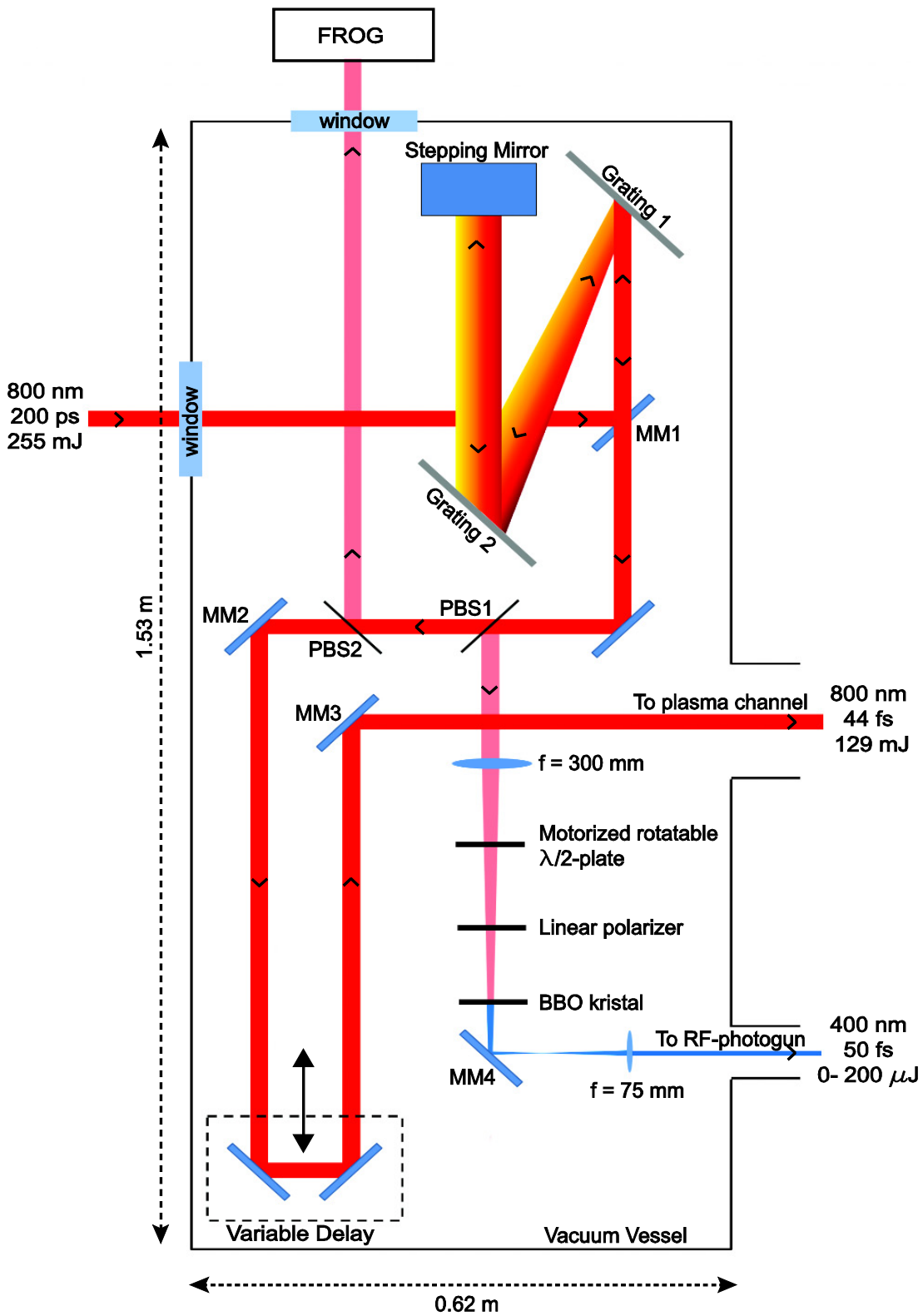
Figure 2.4: Schematic overview of the compressor box to generate the 3 TW laser pulses to drive the plasma wave and the 400 nm laser pulses to photoemit the electrons on the cathode of the RF-photogun.
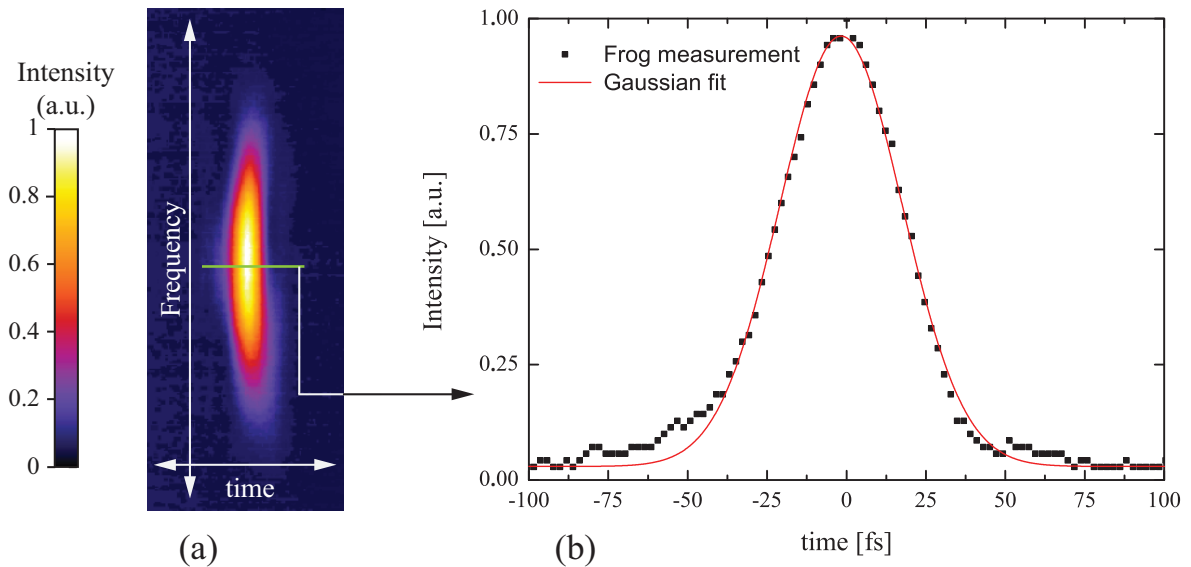
Figure 2.5: (a) FROG trace of a 129 mJ laser pulse. (b) Intensity profile (dots) through the point of highest intensity of the FROG trace versus time (green line). The red line is a Gaussian fit with a FWHM of 45±5 fs, resulting in a 2.9 TW laser pulse.

The pellicle beam splitter PBS2 splits of ~ 2% of the 2.9 TW laser pulse and is directed toward a FROG (Frequency-Resolved Optical Gating) outside the vacuum to measure and adjust the laser pulse length [15]. A FROG is an autocorrelation device which is used to determine the length of ultra short (sub ps) laser pulses. The FROG trace gives the intensities as a function of frequency and time. Fig. 2.5.a shows a picture of a FROG trace of the compressed laser pulse, with the laser operating at full power, 129±8 mJ pulse energy at the exit of the compressor box. Time is given in horizontal direction and frequency in vertical direction. The laser pulse is almost fully compressed. To determine the length of the laser pulse, the intensity profile through the point of highest intensity of the FROG trace versus time is taken i.e. the green line in Figure 2.5.a. The measured intensity profile (along the green line) is shown by the dots in Fig 2.5.b. The red line represents a Gaussian fit through the data. The FWHM of the Gaussian fit was 45±5 fs. Combined with the measured energy at the exit of the compressor box, this results in a (2.9±0.3) TW laser pulse.

To change the compression during operation, the angle and position of the gratings are separately adjustable from outside the vacuum for maximum compression of the laser pulse. The motorized mirrors MM2 and MM3 are needed to assure the right angle of incidence on the delay line and focusing parabola, respectively. The delay line, placed on a motorized stage with a 1 μm precision, is necessary to fine-tune the arrival time between TW laser pulse and electron bunch at the entrance of the plasma channel.

2.2.5 Frequency doubler

Part of the laser pulse energy is used to generate a 400 nm pulse which will be used to photoemit electrons from the cathode plate of the RF-photogun (see chapter 5). The 400 nm and the 3 TW laser pulse have to be generated from the same laser pulse to minimize timing jitter between TW laser pulse and electron bunch at the entrance of the plasma channel. This is done by splitting off approximately 2% (5 mJ) of the TW laser pulse using a pellicle beam splitter (PBS1 in Fig 2.4). The 5 mJ pulse is sent through a birefringent 0.5 mm thick BBO (Beta Barium Borate) crystal for second harmonic generation, to produce pulses at 400 nm [16]. After experimental investigation of the charge produced, it was decided use a 400 nm laser pulse instead of the more commonly used 266 nm (third harmonic of 800 nm) laser pulse (see Sec 5.4 and 5.5 for the investigation and discussion of the effects of a 266 nm and 400 nm laser pulse on the production of electrons). Generating 400 nm laser pulse is technically much easier than 266 nm and requires fewer optical components; moreover, it was observed that there is no noticeable difference in electron bunch properties generated by 266 and 400 nm laser pulses in our setup. A technically simple setup is highly desirable, as the compressor and frequency doubler operate in vacuum where adjustments cannot be easily made.

The 800 nm pulse is focused by a lens with a focal distance of 300 mm (see Fig 2.4). This is done to have a smaller laser spot and thus a higher intensity on the BBO crystal. This is necessary to efficiently produce the 400 nm pulses by the second order process in the crystal which is proportional to the square of the intensity of the 800 nm laser pulse. Too high intensity can damage the BBO crystal and therefore the BBO crystal is positioned at the place where the FWHM of the laser radius is ~ 2 mm. The 400 nm laser pulse after the BBO crystal is reflected by a dichroïc mirror MM4 which reflects the 400nm pulse and transmits the remains of the 800 nm laser pulse. The 400 nm laser pulse is imaged on the centre of the cathode in a spot with FWHM intensity profile of 1.7 mm. This is done by a fused silica lens with a focal distance of 75 mm. The position of the 400 nm laser pulse on the cathode can be adjusted with the motorized dichroïc mirror MM4.

The energy of the 400 nm laser pulse has to be adjustable to change the accelerated charge coming out of the RF-photogun. This is done by reducing the power of the 800 nm laser pulse on the BBO crystal, using a (motorized) rotatable half- lambda plate in combination with a linear polarizer between the lens and the BBO crystal. The polarization of the 800 nm laser pulse is rotated by the half lambda plate (still linear polarized). The rotated polarized laser pulse passes through the linear polarizer which only transmits the p-polarized part of the 800 nm laser pulse and results in lower power on the BBO crystal without changing the other laser pulse properties. The energy of the 400 nm laser pulse required to photo-emit ~ 10 pC is around 20 μJ (see section 5.4.2). In this setup the 400 nm laser pulse energy is adjustable up to 100 μJ.
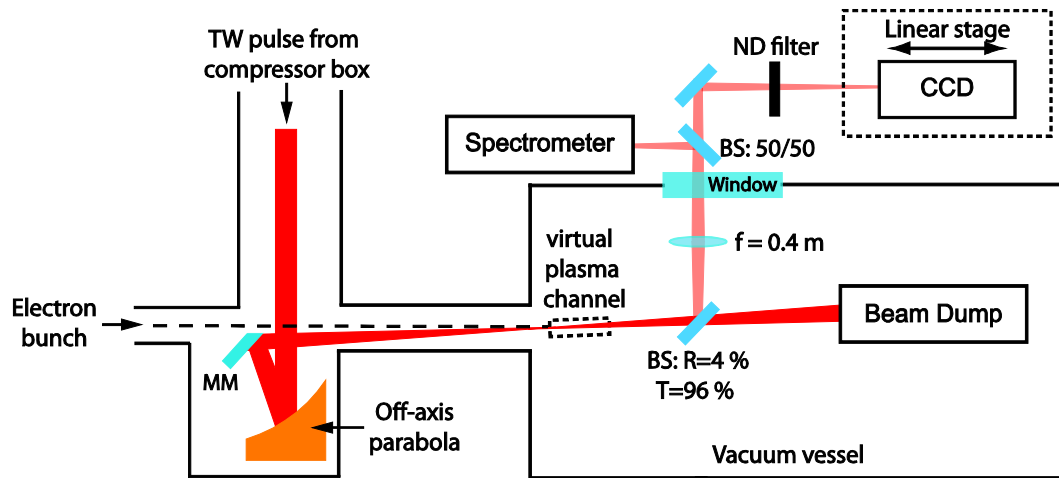
Figure 2.6: System to focus the 3 TW laser pulses at the entrance of the (virtual) plasma channel and the optical components to measure the laser waist and the stability of the focus.

2.3 Focus and pointing stability

The 2.9 TW 800 nm laser pulse needs to be focused on a spot with a typical $1/e^2$ radius of 20-50 μm at the entrance of the plasma channel to perform LWA experiments [1-4]. A gold coated off-axis parabolic mirror is used to focus the 2.9 TW laser pulse coming from the compressor box (see Fig. 2.6). The off-axis parabola has a focal length of 102 cm (40 inch), an f-number of f/10 and an off-axis distance of 19 cm (7.5 inch). The parabola reflects the laser pulse towards a motorized mirror MM which reflects the laser pulse towards the entrance of the plasma channel. To characterize the laser focus, the plasma channel was removed during the experiments described in this section. The entrance of the plasma channel will be placed at the focal point of the laser. The position of the plasma channel is indicated as 'virtual plasma channel' in Fig 2.6.

The electron bunch coming from the RF-photogun also needs to be injected in the plasma channel, while avoiding hitting the motorized mirror. The smallest possible angle between laser path and electron path is between 5 and 10 mrad to allow electron passage. Although the path of the electrons can be adjusted using steering coils (see Sec. 5.2 and Fig. 1.4), this adjustment needs to be as small as possible. It is therefore necessary that the laser pulse is reflected as close as possible to the edge of the motorized mirror, but without introducing too much diffraction. The back of the glass substrate of the motorized mirror (at the side of the electron path) was cut at an angle of 45º to enable electron passage as close as possible to the reflective coating of the motorized mirror.

To image the focus spot, a beam splitter is placed in the vacuum chamber, behind the focus of the laser pulse; it transmits ~ 96 % of the TW laser pulse toward a beam dump and reflects ~ 4 %. A lens with a focal distance of 0.4 m is placed in the vacuum chamber and makes an

Figure 2.7: Focal spot of a single 0.13 TW (a) and a 0.75 TW (b) laser pulse at the place of the entrance of the future plasma channel. The intensity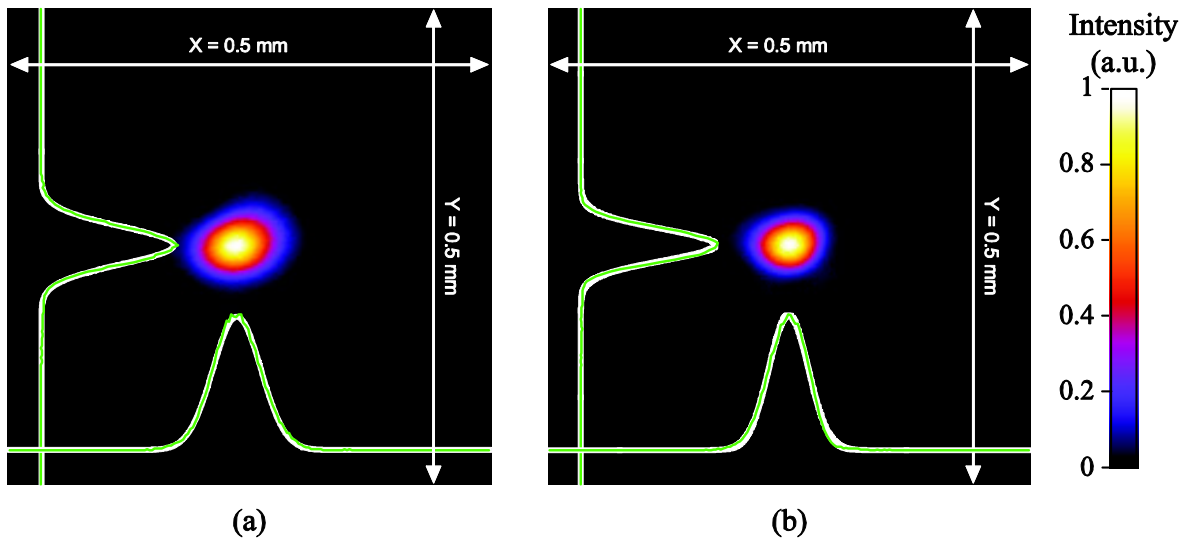 profile at the point of max intensity (green line) with a Gaussian fit (white line) gives a waist with a $1/e^2$ radius of 41 μm respectively 39 μm. Similar intensity profiles at focus are observed up to 2 TW laser pulses.

image of the focus spot on a CCD camera (Point Grey type Flea2) outside the vacuum. In order not to overexpose or damage the CCD camera, neutral density (ND) filters are inserted in the laser path when necessary. The CCD camera is placed on a linear stage. By changing the position of the camera, it is possible to make an image of the plane at the exit of the plasma channel. This will be necessary to perform guiding experiments and measure the properties of the laser at the exit of the plasma channel which is done and described in chapter 3. When changing the position of the camera, a new calibration of the camera is required and this is done for the entrance and exit planes of the plasma channel. Finally, a beam splitter placed outside the vacuum splits off ~ 50 % of the laser pulse energy towards a spectrometer. The laser spectrum is discussed in section 2.4.

For LWA, one of the most important parameters is the spot size of the laser at focus. A picture of the focus spot of a single 0.13 TW and a 0.75 TW laser pulse at the entrance of the plasma channel can be seen in figure 2.7.a respectively b. The green lines are line- outs of the intensity through the center of the spot. The white lines are Gaussian fits to these line- outs. Measurement and fit are almost identical. This is partially caused by the optical resolution of ~ 10 μm of the imaging system. The $1/e^2$ radius of the focal point is in x-direction is found to be 45 μm and 36 μm y-direction and gives an average $1/e^2$ radius of 41 μm for the 0.13 TW laser pulse (corrected for optical resolution). For the 0.75 TW laser pulse, the radii were found to be ~ 2 μm smaller than for the 0.13 TW laser pulse. The experiments in this section were not done at full laser power (2.9 TW) to prevent damage to the detection optics. Raising the laser power from 0.13 TW to 0.75 TW has little effect on the radius and profile of the laser pulse (see fig 2.7). Also the transverse laser profile at the exit of the compressor box shows no noticeable
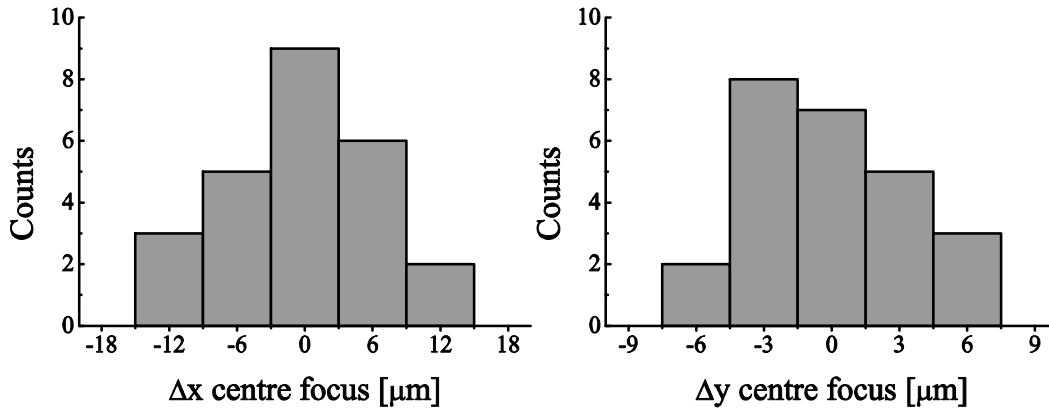
Figure 2.8: Shot-to-shot stability of the centre of the focused 0.25 TW laser pulse for 25 consecutive shots in x- and y-direction.

difference between full (2.9 TW) and reduced power. Therefore it is reasonable to expect the $1/e^2$ radius to be ~ 40 μm for the 2.9 TW laser pulse. This is in the range for the planned LWA experiments with external injection with a plasma density of ~ $10^{24}\,\text{m}^{-3}$.

Another important laser parameter for LWA experiments with external injection is the shot-to-shot stability of the center of the focused laser pulse, because the position of the focus needs to remain stable within a fraction of the spot size to have a consistent overlap between the wakefield generated by the laser pulse and the injected electron bunches. A measurement of this parameter can be seen in Fig. 2.8. This figure shows the number of laser pulses counted as a function of the distance between the centre of each focus and the average position of the centers. This is done in *x*- and *y*-direction for 25 consecutive shots for a 0.25 TW laser pulse. This gives a shot-to-shot stability of the centre of the focused bunch with a RMS spread in *x*- and *y*-direction of respectively 5 μm and 3 μm. It is well below the measured ($1/e^2$ intensity) spot size of 41 μm. Changing the laser power has no noticeable effect on the measured shot-to-shot stability of the focus spot. Similar results concerning focal spot and focus stability of the electron bunch at injection can be found in section 5.5.4.

2.4 Laser spectra

Laser pulses with power over a terawatt are required to drive a plasma wave for LWA. Such an extreme laser power can be achieved by creating ultra short laser pulses. Short laser pulses consist of a broad spectrum. A broader spectrum results in a shorter laser pulse and thus a higher power.

Here we will derive a formula to quickly relate the FWHM of the measured spectrum to the minimum pulse length that can be produced. The spectrum is measured as a function of wavelength. A laser pulse with a Gaussian spectral distribution (in the frequency domain) has

an intensity per unit wavelength, as function of wavelength, $I_\lambda(\lambda)$, given by:

$$I_\lambda(\lambda) = I_{0\lambda} \exp(-\alpha(1 - \lambda_0/\lambda)^2),$$ (2.2)

with maximum intensity $I_{0\lambda}$, central wavelength λ_0 and the constant α depending on the width (FWHM) and central wavelength of the spectrum (because Eq. (2.2) is written as a function of wavelength rather than frequency, it is no longer a Gaussian distribution). The FWHM length of a fully compressed (Fourier or bandwidth limited) laser pulse, Δt_{FWHM} is given by:

$$\Delta t_{FWHM} = \frac{\ln(2)\lambda_0^2}{\pi c \Delta\lambda_{FWHM}} \left(1 + \sqrt{1 + \left(\frac{\Delta\lambda_{FWHM}}{\lambda_0}\right)^2}\right),$$ (2.3)

with $\Delta\lambda_{FWHM}$ the FWHM (bandwidth) of the intensity spectrum as function of the wavelength (i.e. FWHM of Eq. (2.2)).

For laser spectra with $\Delta\lambda_{FWHM} \ll \lambda_0$, such as the Ti:Sa laser used, Eq. (2.2) can be approximated by a Gaussian function:

$$I_\lambda(\lambda) \approx I_{0\lambda} \exp\left(-\frac{\alpha}{\lambda_0^2}(\lambda - \lambda_0)^2\right) = I_{0\lambda} \exp\left(-\frac{4\ln 2 (\lambda - \lambda_0)^2}{\Delta\lambda_{FWHM}^2}\right)$$ (2.4)

and Eq. (2.3) by:

$$\Delta t_{FWHM} \approx \frac{2\ln(2)\lambda_0^2}{\pi c \Delta\lambda_{FWHM}}$$ (2.5)

For an optimally compressed Ti:Sa laser pulse with a central wavelength of 800 nm, Eq. (2.5) simplifies to:

$$\Delta t_{FWHM}\,[\text{fs}] \approx \frac{940}{\Delta\lambda_{FWHM}\,[\text{nm}]}$$ (2.6)

The spectra of the laser have been measured at different places in the laser setup and are shown in Figure 2.9. Measurement of the spectrum has been done at the exit of the oscillator, the stretcher, the third amplification Ti:Sa crystal and after the compressor. Equation 2.4 is fitted on the intensity profiles of Fig. 2.9 to determine $\Delta\lambda_{FWHM}$ of the measured spectra. With the use of Eq. (2.6) the theoretical laser pulse length at optimal compression can be calculated. The bandwidth $\Delta\lambda_{FWHM}$ and the theoretical value of Δt_{FWHM} are found in Table 2.1.

The bandwidth of the spectrum of the laser pulses is broadest at the exit of the oscillator and the pulse can theoretically be as short as 8 fs. In the stretcher, part of the spectrum is cut off due to the limited size of the optical components in the stretcher. Wavelengths between ~ 730 nm and ~ 850 nm are within range of the stretcher. The emission spectrum of Ti:Sa has a peaked shape with a maximum around 800 nm [17]. Therefore the part of the laser spectrum with wavelengths closest to the central 800 nm is amplified most which results in a narrower spectrum after each amplification pass through the crystal. This is known as spectral gain
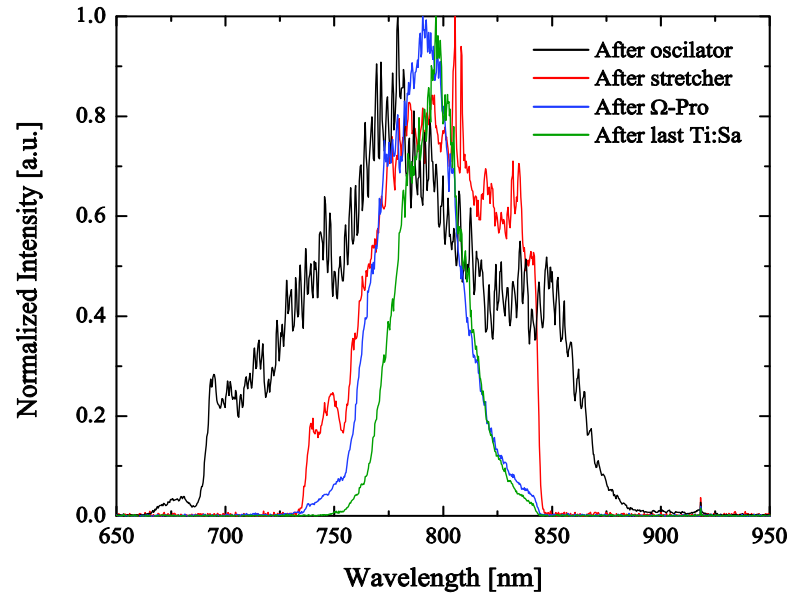
Figure 2.9: Spectrum of the 800 nm laser pulses at the exit of the oscillator (black), the stretcher (red), the Ω-Pro (blue) and the last Ti:Sa crystal. Spectral gain narrowing can be observed, characteristic to Ti:Sa amplification [13].

narrowing. The bandwidth goes from 67 nm after the stretcher to 42 nm after the Ω-pro, 40 nm after the second and finally to 35 nm after the third Ti:Sa crystal. A stretcher with larger optical components would not result in a significantly broader bandwidth after the last amplification in the third Ti:Sa crystal because of this spectral gain narrowing effect. The measured bandwidth of the spectrum after the compressor gives a theoretical pulse length of ~30 fs at optimal compression. A measurement of the pulse length after compression can be seen in Fig 2.5 and was found to be (45±5) fs. This is slightly higher than the theoretical value and could indicate a small misalignment of stretcher and/or compressor or the presence of higher order terms in the chirp. In fact, looking closely at figure 2.5, some higher order is still recognizable. The measured value is also close to the detection limit of the FROG (given as 30 fs according to the manufacturer [15]), so that a slight overestimation of the pulse length is made in the measurement.

Table 2.1: Bandwidth of the spectra of the laser pulse and associated theoretical pulse length at optimal compression at the exit of different components of the laser system.

	$\Delta\lambda_{FWHM}$ [nm]	Δt_{FWHM} [fs]
After oscillator	120	8
After stretcher	67	15
After Ω-pro	42	23
After Second Ti:Sa crystal	40	24
After Third Ti:Sa crystal	35	27
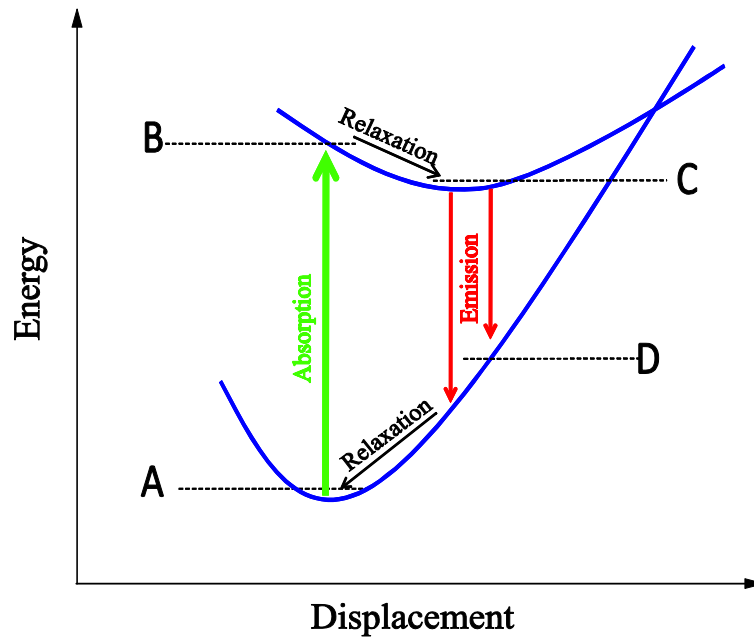
Figure 2.10: Schematic representation of the energy levels of the titanium ions in the sapphire lattice as a function of the displacement of the Ti^{+3} ion [18].

2.5 Measurements and simulations of the laser pulse energy

In this section measurements and simulations of the energy of the 800 nm laser pulses are done after each pass through the pumped Ti:Sa crystal [19]. This is done for the second and third amplifying crystal (see Sec. 2.2.2 and Fig.2.2). A thorough theoretical description of the rate equations used in the simulations and properties of Ti:Sa crystals can be found in Barros [12].

Ti:Sa crystals have several benefits to serve as amplifying medium for ultra short laser pulses [17]. The emission and absorption spectrum are clearly separated and the emission spectrum covers a broad bandwidth of 400 nm around the central 800nm. A broad emission bandwidth is a prerequisite to create short laser pulses. Ti:Sa also has a relatively large absorption cross section with a broad bandwidth of 200 nm around the central 500 nm. Solid state pumping lasers such as Q-switched frequency doubled YAG and YLF lasers emit laser pulses with a single wavelength of typical ~ 530 nm and are very well suited to pump Ti:Sa crystals. Furthermore Ti:Sa crystals are good heat conductors which makes it possible to use relatively high pump power at comparatively high repetition frequencies (up to ~1 kHz). For those reasons Ti:Sa crystal are now commonly used to create and amplify short laser pulses.

The energy diagram of the titanium ions in the sapphire lattice is schematically shown in Figure 2.10. When the crystal is pumped, the ions are excited from the ground state (A) to an

electronically and vibrationally excited state (B). The system quickly relaxes by a fast phonon transition to state (C). This state is a metastable state with a lifetime of the order μs. Transition from (C) to (D) takes place through spontaneous and stimulated emission. The transition from the vibrationally excited state (D) back to (A) is again a fast (phonon) transition. To model the system we only take into account the density of ions in states (A) and (C) for absorption, spontaneous emission and stimulated emission. Because the transitions from (B) to (C) and from (D) to (A) are fast, stimulated emission from (B) back to (A) by the pump laser, and re-absorption from (D) to (C) can be neglected.

The absorption rate for electrons from the ground state (A) to the excited state (C) in the crystal is proportional to the intensity (flux density) of the pump laser I_p, to the density n_0 of the electrons in the ground state and to the absorption cross section σ_{abs}. The absorption cross section is wavelength dependent and the absorption rate becomes:

$$\left(\frac{\partial n_1(t,\vec{r})}{\partial t}\right)_{abs} = -\left(\frac{\partial n_0(t,\vec{r})}{\partial t}\right)_{abs} = \int_{\omega} \frac{I_p(t,\vec{r},\omega)}{\hbar\omega} n_0(t,\vec{r})\sigma_{abs}(\omega)d\omega, \tag{2.7}$$

with n_1 the density of the electrons in the excited state at position $\vec{r}$ at time t. This equation is integrated over the emitted frequencies ω of the pump laser. The pump laser used in this setup is a Nd:YAG laser emitting laser pulses of 532 nm. The bandwidth of the pump laser is very small so that Eq. (2.7) simplifies to:

$$\left(\frac{\partial n_1(t,\vec{r})}{\partial t}\right)_{abs} = -\left(\frac{\partial n_0(t,\vec{r})}{\partial t}\right)_{abs} \approx \frac{I_p(t,\vec{r},\omega_p)}{\hbar\omega_p} n_0(t,\vec{r})\sigma_{abs,p}, \tag{2.8}$$

with ω_p the frequency of the Nd:YAG laser and $\sigma_{abs,p}$ the absorption cross section at 532 nm.

In a similar way as Eq. (2.7), the stimulated emission rate is proportional to the intensity of the 800 nm laser pulse I_L, the density of the electrons at excited state and the emission cross section σ_{stim}:

$$\left(\frac{\partial n_0(t,\vec{r})}{\partial t}\right)_{stim} = -\left(\frac{\partial n_1(t,\vec{r})}{\partial t}\right)_{stim} = \int_{\omega^-}^{\omega^+} \frac{I_L(t,\vec{r},\omega)}{\hbar\omega} n_1(t,\vec{r})\sigma_{stim}(\omega)d\omega. \tag{2.9}$$

As the 800-nm laser pulses consist of a broad spectrum of frequencies (Fig. 2.9), one has to integrate between the lowest (ω^-) and highest (ω^+) frequency of the 800 nm laser pulse.

The rate of spontaneous emission is proportional to the excited state density n_1 and inversely proportional to is lifetime τ_{spon}:

$$\left(\frac{\partial n_0(t,\vec{r})}{\partial t}\right)_{spon} = -\left(\frac{\partial n_1(t,\vec{r})}{\partial t}\right)_{spon} = \frac{n_1(t,\vec{r})}{\tau_{spon}}. \tag{2.10}$$

The photons emitted by spontaneous emission pass through a part of the crystal and will generate extra photons by means of stimulated emission, so-called Amplified Spontaneous Emission.

The intensity of the pump laser and the 800 nm laser pulse is given by:

$$\left(\frac{\partial I_p\left(t,\vec{r},\omega_p\right)}{\partial t}\right)_{abs} = v_c \left(\frac{\partial I_p\left(t,\vec{r},\omega_p\right)}{\partial z}\right)_{abs} = -I_p\left(t,\vec{r},\omega_p\right)n_0(t,\vec{r})\sigma_{abs,p} \qquad (2.11)$$

$$\left(\frac{\partial I_L\left(t,\vec{r},\omega\right)}{\partial t}\right)_{stim} = v_c \left(\frac{\partial I_L\left(t,\vec{r},\omega\right)}{\partial z}\right)_{stim} = I_L\left(t,\vec{r},\omega_p\right)n_1(t,\vec{r})\sigma_{stim}(\omega), \qquad (2.12)$$

with v_c the speed of light in the Ti:Sa crystal and z the depth in the crystal along the z-axis (axis of the crystal).

The properties of the crystal, supplied by the manufacturer (CRYSTAL SYSTEMS, inc), are summarized in Table 2.2. During simulation it was found that the fraction of the emitted photons by spontaneous emission and amplified spontaneous emission is small compared to the fraction of stimulated emission (1/1000). Therefore, these terms can be neglected in the model presented here.

Simulations are done in Matlab by dividing the Ti:Sa crystal in segments with inner radius r, external radius $r + dr$ and thickness dz. For both crystals 100 segments in r-direction are used in combination with 100 segments in z-direction resulting in a total of 10000 segments per crystal. With the use of Eq. (2.8), the excited state density in the first layer of segments in the z-direction is calculated. The intensity of the pump laser, when entering the second layer of segments in the z-direction, is calculated with Eq. (2.11). The excited state density in the second layer can now be calculated with Eq. (2.8) and the new-found intensity of the pump laser, etc. This way, the excited state density of the Ti:Sa crystal is found as a function of z and r.

Table 2.2: Crystal and laser input parameters used for Matlab simulations

	Parameter	Second Ti:Sa crystal	Third Ti:Sa crystal
Crystal (Cylindrical)	Radius	5 mm	10 mm
	Length	10 mm	22 mm
	Absorption coefficient	300 m^{-1}	300 m^{-1}
	Absorption cross section	1×10^{-23} m^2	1×10^{-23} m^2
	Emission cross section	4.1×10^{-23} m^2	4.1×10^{-23} m^2
Pump Laser (Top Hat)	Energy per pulse	153 mJ	730 mJ
	Width	2.9 mm	9 mm
	Length	6 ns	6 ns
	wavelength	532 nm	532 nm
800 nm pulse (Gaussian)	Energy per pulse	0.44 mJ	33.1 mJ
	FWHM radius	2 mm	6 mm
	Length	200 ps	200 ps
	wavelength	795 nm	795 nm
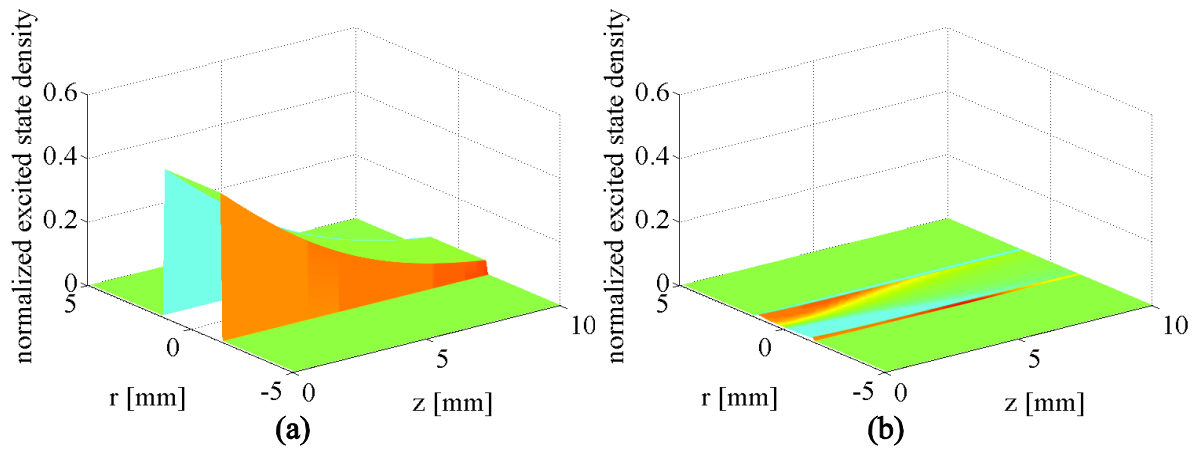
Figure 2.11: Simulated normalized excited state density of the second Ti:Sa (Brewster angel) crystal before the 800 nm laser pulse has passed through the crystal (a) and after 5 passes of the 800 nm laser pulse (b). The crystal is pumped by a 153 mJ laser pulse from the YAG laser.
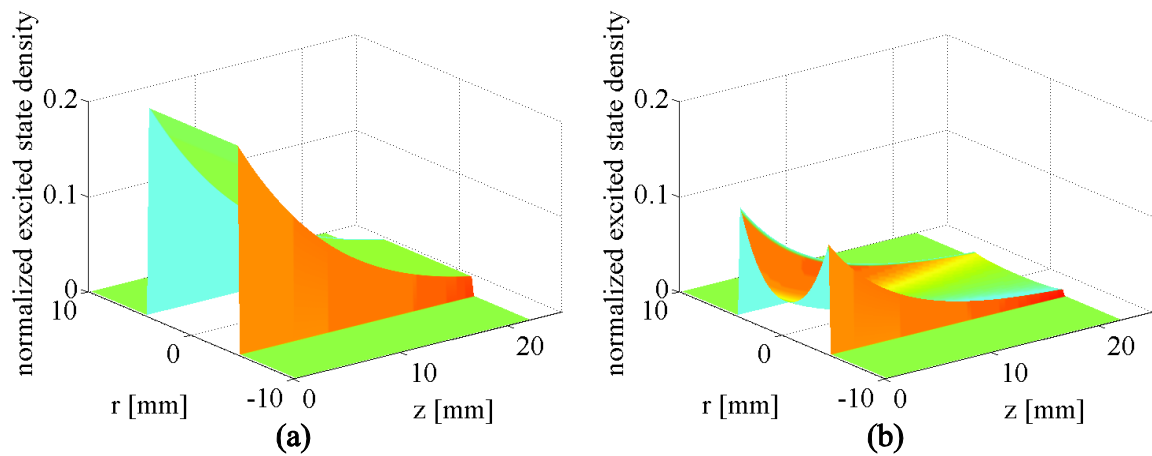
Figure 2.12: Simulated normalized excited state density of the third Ti:Sa (cylindrical) crystal before the 800 nm laser pulse has passed through the crystal (a) and after 4 passes of the 800 nm laser pulse (b). The crystal is pumped by a 730 mJ laser pulse from the YAG laser.

The same is done for the stimulated emission of the 800 nm laser pulse by combining Eq. (2.9) and Eq. (2.12), with the excited state density calculated earlier as the initial condition. The 800 nm laser pulse passes the second Ti:Sa crystal 5 times and the third Ti:Sa crystal 4 times. During simulations also the direction of passage of the 800 nm laser pulse through the crystal is taken into account.
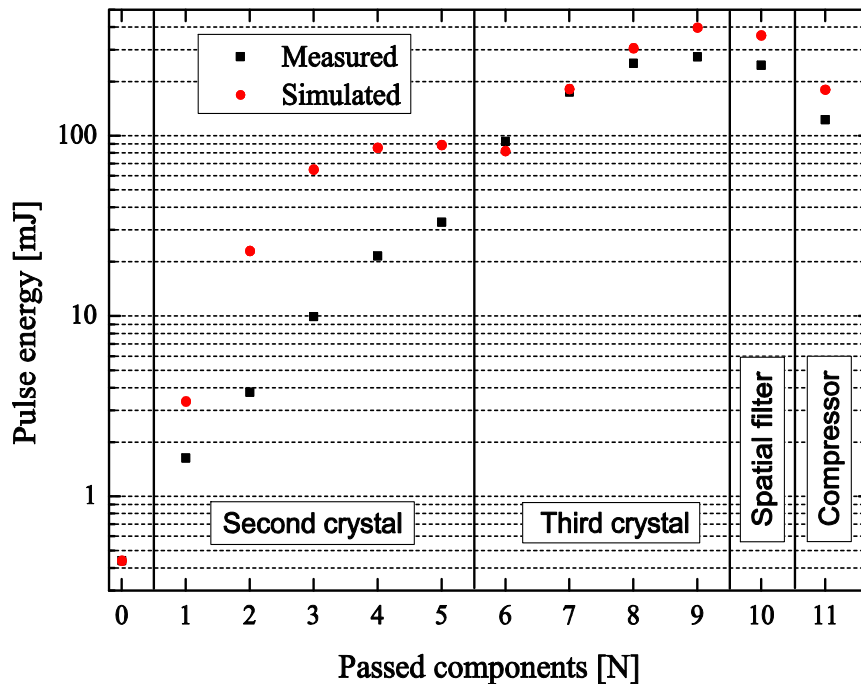
Figure 2.13: Measured (black dots) and simulated (red dots) energy of the 800 nm laser pulse after each pass through the second and third amplifying Ti:Sa crystal and after the spatial filter and the compressor.

The model was used to design the laser system. After the system was built and the parameters tweaked (beam sizes, alignment), the model was run again, but now with the measured parameters of the laser beams as input. The input parameters of the pump laser and 800 nm laser pulse used for these simulations are found in Table.2.2. The pump laser has a transverse top hat profile while the 800 nm pulses have Gaussian profile in transverse direction. The energy of the pump laser and 800 nm laser pulses are measured using an Ophir PE50BB-DIF pyroelectric energy sensor.

The simulated normalized excited state density (the fraction of excited titanium ions) versus radius and *z*-direction can be seen in Figure 2.11 and 2.12 for the second respectively third amplifying Ti:Sa crystal. Figure 2.11.a represents the excited state density of the second 10 mm long Ti:Sa crystal after being pumped by a 153 mJ YAG laser pulse with a 2.9 mm diameter top hat profile. In Figure 2.11.b the excited state density is given after 5 passes of a 800 nm laser pulse through the crystal with initial excited state density as in Figure 2.11.a. The 800 nm laser pulse before amplification (coming from the Ω-pro) has a measured energy of 0.44 mJ and Gaussian transverse profile with a FWHM of 2 mm. In Figure 2.12.a the excited state density is shown for the third, 22 mm long Ti:Sa crystal after being pumped by a 730 mJ YAG laser pulse with a 9 mm diameter top hat profile. The 800 nm laser pulse after the second crystal was measured to have 33.1 mJ energy, with a transverse Gaussian profile with FWHM

of 6 mm. This pulse was used as the input to simulate the density of excited states and further amplification in the 22 mm crystal. The (normalized) excited state density after four passes is shown in Figure 2.12.b.

The comparison between the simulated and measured energy of the 800 nm laser pulse after each pass through the crystals is given in Table 2.3 and Figure 2.13. Each measurement is an average of 300 laser pulses at a repetition rate of 10 Hz. There is significant difference between simulations and measurements, especially in the 10-mm crystal. The most important reason is, that in reality the laser alignment is not perfect because the 800 nm laser pulse propagates at an angle with respect to the axis of the crystal. The overlap between the 800 nm laser pulse and the distribution of excited states in the crystal is therefore not optimal. Furthermore, during the 5 passes through the crystal, the size of the 800 nm changes due to the diffraction of the beam. This was not taken into account in the simulations. Both these effects are less important in the 22-mm crystal, because the beam is larger (less diffraction), the beam comes in at a smaller angle due to the geometrical design of this part, and the pump volume is larger. Although the simulations show that an extra of ~ 100 mJ is available for amplification, the measured 285 mJ is sufficient for LWA experiment.

Figure 2.13 also shows the energy after the spatial filter and compressor. The measured energy lost is approximately 10% in the spatial filter and 50% in the compressor. A deposit which reduces reflectivity was found on the grating. Cleaning the gratings would result in a lower energy loss of 40% (see Sec.2.2.4). The measured energy after spatial filtering is found to be 255 mJ and 129 mJ after compression resulting in a 2.9 TW laser pulse.

Table 2.3: Simulated and measured energy of the 800 nm laser pulse after each pass through the pumped Ti:Sa crystals , the spatial filter and the compressor.

	Pass	Simulated energy [mJ]	Measured energy [mJ]
Second Ti:Sa crystal	0	0.44	0.44 ± 0.06
	1	3.4	1.63 ± 0.13
	2	23.1	3.77 ± 0.22
	3	65.8	9.92 ± 0.65
	4	86.3	22.2 ± 1.2
	5	89.3	33.1 ± 1.9
Third Ti:Sa crystal	0	33.1	33.1 ± 1.9
	1	82.3	96.6 ±4.0
	2	182	181 ± 10
	3	306	263 ± 7
	4	398	285 ± 10
Spatial filter	1	358	255 ± 9
Compressor	1	181	129 ± 8

2.6 Conclusion

The constructed Titanium:Sapphire laser system satisfies the requirements for LWA with external injection of 6 MeV electrons behind the laser pulse in a typical plasma density of $\sim 10^{24}$ m^{-3}. The laser system generates (2.9 ± 0.3) TW laser pulses to drive a plasma wave at an adjustable repetition rate between 1 an 10 Hz. The energy of the laser pulse was found to be 129 mJ with a temporal FWHM length of 45±5 fs. The laser pulses can be focused to a waist with a Gaussian transverse intensity profile with a $1/e^2$ radius of 40 μm. This is in range with the matched spot size for guiding in plasma channels with a typical density of 10^{24} m^{-3}. The shot-to-shot stability of the centre of the laser focus was found to be ~ 4 μm and is within a fraction of the measured waist of 40 μm. This stability is sufficient to perform successful plasma guiding and LWA experiments.

Comparison between measurements and simulations of the amplification of the 800 nm laser pulse in the Titanium:Sapphire crystals show that approximately 25% of the laser energy is lost during the amplification process. These losses are mostly caused by the chosen geometry of the setup.

The final properties of the laser pulse at the entrance of the (planned) plasma channel are summarized in Table 2.4.

Table 2.4: Measured properties of the laser pulse at the entrance of the plasma channel.

Parameter	Symbol	Value
Maximum repetition rate	f	10 Hz
Central wavelength	λ_0	800 nm
Bandwidth spectra (FWHM)	$\Delta\lambda_{FWHM}$	35 nm
Pulse length (FWHM)	Δt_{FWHM}	44 fs
Maximum energy per pulse	E_{max}	129 mJ
Maximum power per pulse	P_{max}	2.9 TW
Radius ($1/e^2$ intensity)	r	40 μm
Pointing stability x-direction (RMS)	$\sigma_{\Delta x}$	5 μm
Pointing stability y-direction (RMS)	$\sigma_{\Delta y}$	3 μm
Peak intensity	I	1.0×10^{17} Wm^{-2}
Laser strength parameter[1]	a_0	0.22

---

[1]   The laser strength parameter a_0 is defined as the peak amplitude of the normalized vector potential of the laser field and is related to the peak intensity I and the central wavelength λ_0 of a linearly polarized Gaussian laser pulse by: $a_0 \approx 8.6 \times 10^{-10} \times \lambda_0[\mu m] \times I^{1/2}$ [W/cm^2] [20].

References

[1]   A. G. Khachatryan, F. A. van Goor, K.-J. Boller, A. J. W. Reitsma and D. A. Jaroszynski, *Extremely short relativistic-electron-bunch generation in the laser wakefield via novel bunch injection scheme*, Phys. Rev. ST Accel. Beams, Vol. 7, 121301 , (2004).

[2]   A. Irman, M. J. H. Luttikhof, A. G. Khachatryan, F. A. van Goor, J. W. J. Verschuur, H. M. J. Bastiaens, and K.-J. Boller, *Design and simulation of laser wakefield acceleration with external electron bunch injection in front of the laser pulse*, J. Appl. Phys., Vol. 102., 024513, (2007).

[3]   W. H. Urbanus, W. van Dijk, S. B. van der Geer, G. J. H. Brussaard, and M. J. van der Wiel, *Front-to-end simulations of the design of a laser wakefield accelerator with external injection*, J. Appl. Phys., Vol. 99, 114501, (2006).

[4]   W. van. Dijk, *Simulations and Experiments on External Injection for Laser Wakefield Acceleration*, PhD thesis, Einhoven University of Technology, ISBN: 978-90-386-2316-0, (2010).

[5]   M. J. H. Luttikhof, A. G. Khachatryan, F. A. van Goor, and K.-J. Boller, *The effect of the vacuum-plasma transition and an injection angle on electron-bunch injection into a laser wakefield*, Phys. Plasmas, Vol. 14, 083101, (2007).

[6]   M. J. H. Luttikhof, *Theoretical investigation of external injection schemes for laser wakefield acceleration*, PhD thesis University of Twente, ISBN: 978-90-365-3071-2, (2010).

[7]   W. van Dijk, S. B. van der Geer, M. J. van der Wiel, and G. J. H. Brussaard, *Parameter study of acceleration of externally injected electrons in the linear laser wakefield regime*, Phys. of Plasmas, Vol. 15, 093102, (2008).

[8]   D. Strickland and G. Mourou, *Compression of amplified chirped pulses*, optics communications, Vol. 56, Issue 3, pp. 219-221, (1985).

[9]   P. S. Banks, M. D. Perry, V. Yanovsky, S. N. Fochs, B. C. Stuart and J. Zweiback, *Novel All-Reflectrive Stretcher for Chirped-Pulse Amplification of Ultrashort Pulses*, IEEE journal of quantum electronics, Vol. 36, Issue 3, p. 268, (2000).

[10]   M.J. de Milliano, *Implementation of a new stretcher design in a terawatt laser system,* Eindhoven University of thecnology, Bachelor thesis, FTV 2006-03, (2006).

[11]   Femtolasers GmBH, User *Manual: "Omega Pro Amplifier"*, Femtolasers Productions, S.N.: 1008 03/99, (1998).

[12]   J. Barros, *Tera-Watt laser Amplifier: Design and Partial Implementation,* Eindhoven University of Technology, master thesis, FTV-TIB 2002-01, (2002).

[13]   J. Diels and W. Rudolph, *Ultrashort laser pulse phenomena,* Academic Press Inc., ISBN: 0-12-215492-4, (1996).

[14] Hecht. *Optics. second. edittion*, Addison-Wesley Publishing Company, ISBN: 0-201-11611-1, (1987).

[15] Positive Light, *User Manual: Frequency Resolved Optical Gating,* (1998).

[16] K. A. Daamen, *Reverse engineering the INGCRYS Laser Systems Ltd. Third Harmonic Generation*. Eindhoven University of Technology, Bachelor thesis, (2007).

[17] P. F. Moulton, *Spectroscopic and laser characteristics of Ti:Al2O3*, J. Opt. Soc. Am. B, Vol. 3, pp. 125-133, (1986).

[18] K. F. Wall and A. Sanchez, *Titanium Sapphire Lasers*, Lincoln Laboratory Journal , Vol. 3, p. 447, (1990).

[19] T. de Kruif, *Analysis of an ultra-short pulsed laser used for Laser Wakefield Acceleration,* Eindhoven University of Technology, CQT-2011-02, (2011).

[20] E. Esarey, P. Sprangle, J. Krall, A. Ting, *Overview of Plasma-Based Accelerator Concepts,* IEEE Trans. on Plasma Science, Vol. 24, Issue 2, (1996)

Chapter 3

Plasma Guiding.

3.1 Introduction

Focusing a laser pulse with a power of a couple of TW with a Gaussian transverse intensity profile - as described in the previous chapter - in a plasma with a density of ~ $10^{24}\,\mathrm{m^{-3}}$, creates a plasma wave on which externally injected electrons (with energy of a few MeV) can be accelerated to hundreds of MeV in a few centimeters [1–4]. To accelerate electrons in a plasma up to the point of dephasing over distances exceeding the Rayleigh range, the laser pulse has to propagate in a collimated mode through the plasma. Such an optically guided laser pulse has a constant intensity over the complete length of the plasma. A possible technique to guide a laser pulse with a Gaussian transverse intensity profile through the plasma is by preforming the plasma in such a way that the electron density profile is parabolic in radial direction, with minimum density on-axis [5]. Density profiles like this can be created in a slow capillary discharge plasma and were first investigated by Hooker, Spence and Butler [6-8]. A setup has been developed to create such a slow capillary discharge hydrogen plasma and to test the guiding properties of the laser pulse in the plasma channel.

In this chapter a short theoretical overview of the plasma properties for guiding laser pulses in a slow capillary discharge plasma is presented in section 3.2. An overview the setup, including the capillary holder and the high-voltage pulse source used in the experiments to create a plasma channel with an appropriate plasma profile is described in sec 3.3. Guiding experiments were first done with a 13 ns Helium-Neon laser pulse (sec 3.4) and later with 0.13 TW laser pulses (sect 3.5). A time window for guiding of more than 0.5 µs and over 90%

transmission of the laser pulse energy was found. Unexpectedly, these good guiding properties are found to exist during a spurious secondary discharge, 1.5 μs after the initial discharge. These results are described in section 3.5.2. The dependence of some of the guiding properties on the pressure in the capillary is investigated in section 3.5.3.

3.2 Plasma guiding

A high intensity laser pulse focused on a homogeneous plasma will diverge after focus. This results in a local decrease of the laser intensity. The electric fields in the plasma (created by the laser pulse) which are used for electron acceleration will therefore also decrease. As a consequence, only a small part of the plasma wave is suitable for acceleration. The length of the plasma wave in a homogenous plasma that can be effectively used for acceleration is typically on the order of the Rayleigh length, given by:

$$Z_R = \frac{\pi w_0^2}{\lambda},$$
(3.1)

with λ the wavelength of the laser and w_0 the $1/e^2$ radius of the laser beam (intensity) at focus. For a 800 nm laser focused on a typical $1/e^2$ radius of 40 μm at the entrance of the plasma the Rayleigh length is $\sim$ 6 mm. When accelerating electrons on a plasma wave driven by a laser pulse in a plasma with a density of $n_e = 0.7 \times 10^{24}$ m^{-3} and assuming the laser intensity to be constant during propagation, the dephasing length is $\sim$ 10 cm and thus approximately 15 times the Rayleigh length (see chapter 6). The dephasing length is the distance over which the electrons outrun the accelerating part of the plasma wave and enter its decelerating part (see Sec. 1.3). The electrons exiting the plasma obtain maximal energy if the plasma is terminated at the point of dephasing. Therefore a collimated TW laser pulse, propagating through a plasma of length equal to the dephasing length is a prerequisite to accelerate electrons to the maximum achievable energy.

A possible way to achieve guiding is by relativistic self-focusing [9,10] which requires focusing a laser pulse with a power of tens of TW on a spot with $1/e^2$ radius of typically $\sim$ 10 μm in a gas jet of a few mm length [11-13]. The drawback of this approach is that the laser power necessary for self-guiding is inversely proportional to the plasma density and the guiding length is limited to a couple of mm in practice. To accelerate to an electron energy of a couple of hundred MeV, a plasma density of around 1×10^{24} m^{-3} and guiding over a couple of cm is required. Therefore, a guiding structure without relativistic self-focusing is needed. One way to guide an intense laser pulse over long distances in a low density plasma is by using capillary tubes as a waveguide where the laser pulse is guided by the capillary inner wall. This allows the guiding of laser pulses with a smooth transverse Gaussian intensity profile in a gas-filled capillary in monomode propagation [14, 15]. Successful guiding experiments with capillaries up to 8 cm and laser pulses of 3×10^{17} W/cm^2 have been reported [16]. Another method to

guide laser pulses over cm-scale distances in a low density plasma is by preforming the plasma density profile. The divergence of a laser pulse with a Gaussian transverse intensity profile can be compensated by a plasma with a parabolic transverse electron density profile. This results in a collimated propagation of the laser pulse through the plasma [5]. In the ideal case, when the laser pulse is guided without scalloping, the laser pulse is said to be matched to the plasma channel. The transverse parabolic electron density profile needed, is given by:

$$n_e(r) = n_e(0) + \Delta n_e \left(r/r_m \right)^2 , \qquad (3.2)$$

with $n_e(r)$ the electron density at radius r and $\Delta n_e = n_e(r_m) - n_e(0)$ the increase in plasma density at a radius r_m. If there is no ionization of the plasma by the laser pulse and if relativistic and ponderomotive effects can be neglected, the matched spot size of the laser pulse is given by [6, 17]:

$$W_M = \left(\frac{r_m^2}{\pi r_e \Delta n_e} \right)^{\frac{1}{4}} , \qquad (3.3)$$

with r_e the classical electron radius, 2.818×10^{-15} m. The matched spot size is defined as the $1/e^2$ radius of the laser pulse at focus. A plasma with a transverse parabolic electron density profile suitable for guiding can be created in a slow capillary discharge plasma. Successful guiding experiments have been reported with high intensity laser pulses in centimeter scale plasma channels [8, 18]. Electrons have been accelerated from 0 to 1 GeV in a 3.3 cm long preformed plasma channel at an electron density of 4.3×10^{18} cm^{-3} in combination with a 40 TW laser pulse by Leemans et al. [19]. A similar capillary discharge plasma waveguide is used in the experiments in this thesis as it is known for its good guiding properties and is well-documented in literature.

3.3 Slow capillary discharge waveguide

A setup has been built to create a plasma channel with a parabolic electron density profile to perform laser guiding experiments. A schematic overview of this device is given in figure 3.1. The capillaries used to surround the plasma channel are made of alumina (polycrystalline aluminum oxide) with purity between 97.5% and 99.5% made by Agate Products Ltd. [20]. Alumina is chosen because it is an electrical insulator with a relatively high thermal conductivity (30 Wm^{-1}K^{-1}) and has a high melting point (2072 ºC). The external radius of the capillaries is 1.5mm. The capillaries are 10 cm long and can easily be cut at the desired length for experimenting. Capillaries with an inner radius of 100, 150 and 200 µm are available. The capillary is supported by a PEEK (Polyether Ether Ketone) structure which can be adjusted to the length of the capillary. PEEK is a electrical insulator with a relatively high melting point (for a synthetic material) of 343 ºC. Furthermore it has a high stiffness, bending and tensile strength, can easily be machined and has low outgassing properties in vacuum [21]. Hollow
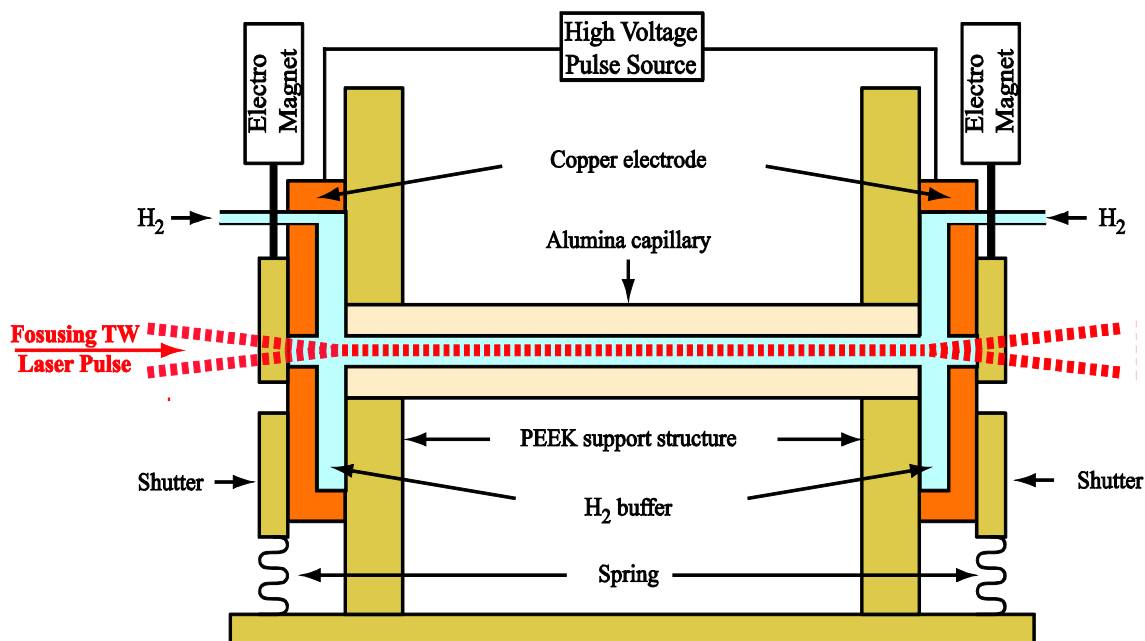
Figure 3.1: Schematic overview of the device to create slow capillary discharge plasma with transverse parabolic electron density profile.

copper electrodes are placed at both ends of the capillary and the hollow space is used as a hydrogen buffer through which the capillary is filled. A hole in the middle of the electrodes allows the TW laser pulse to be focused at the entrance of the capillary. Both holes are closed off by shutters.

The shutter system is necessary to keep the background pressure as low as possible because the plasma channel and the RF-photogun are in the same vacuum environment. The RF-photogun only operates decently at high vacuum. The shutter system reduces the background pressure in the plasma vessel approximately by two orders of magnitude compared to operation without shutters. Furthermore, two pump restrictions are in place, one between the vessel containing the plasma setup and the vessel containing the off-axis parabolic mirror and one between the RF-photogun and the parabola vessel (See also figure 1.4). Because the compression ratio of the turbo pumps used is lower for hydrogen by 3 orders of magnitude than for air, two turbo pumps had to be placed in series to achieve the desired background pressure. This is done for the turbo pumps connected to the parabola vessel and the RF-photogun. These measures together make the background pressure in the RF-photogun rise from $\sim 1 \times 10^{-7}$ mbar without hydrogen in the capillary to $\sim 3 \times 10^{-7}$ mbar with a hydrogen pressure of 30 mbar in the capillary and shutter operating at 5 Hz. This hydrogen background pressure was found to be sufficiently low for operation of the RF-photogun.

The shutters are normally closed by springs and can be opened with the use of electromagnets. The shutters are only opened when a TW-laser pulse has to pass (be guided). Because the complete device is placed in vacuum, the electromagnets are thermally connected
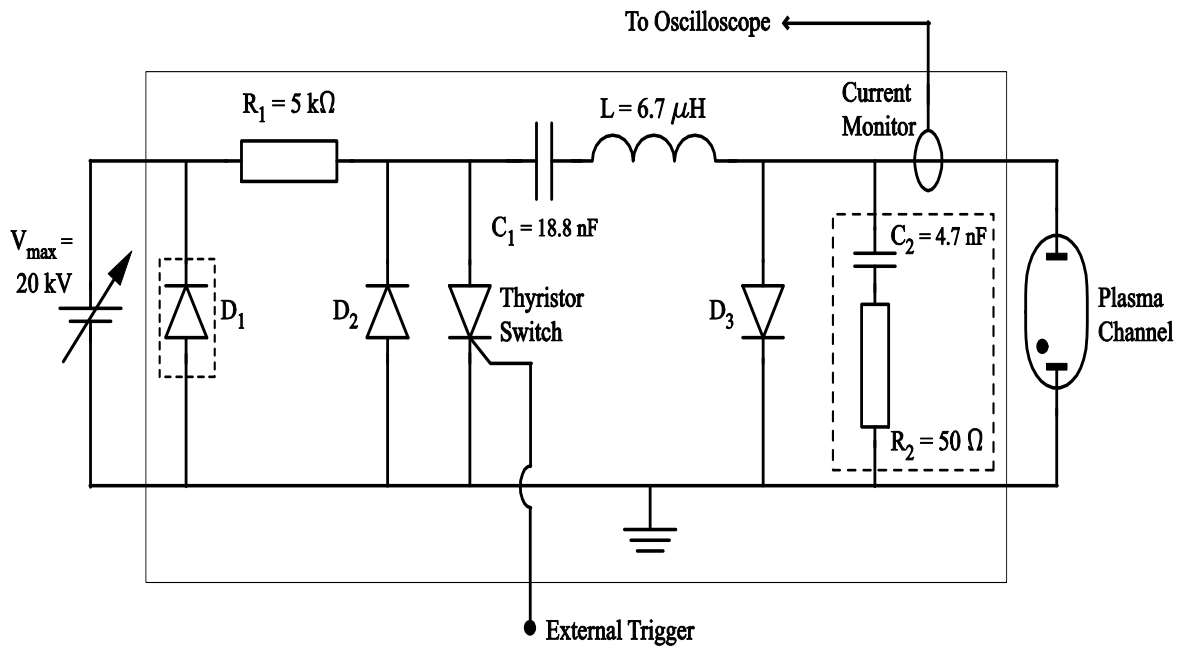
Figure 3.2: Electric scheme of the high voltage pulse source.

to the surrounding vacuum vessel to prevent overheating and make an operating frequency of 10 Hz achievable. During one cycle, the shutters are typically opened for ~ 5 ms. With the shutters closed, the buffer (~1 cm^3 each) in the electrodes and the capillary are filled with hydrogen. By shortly opening the shutters, most of the hydrogen escaping to the vacuum will come from the buffers and not from the capillary. A quasi stable hydrogen pressure in the capillary during operation is therefore attained. The electrodes are connected to a high-voltage pulse source (max 20 kV). A high-voltage pulse over the electrodes results in an electrical breakdown through the hydrogen filled capillary. The ensuing current pulse of 200-400 A creates a fully ionized plasma in the capillary. Approximately 0.5 μs after breakdown the transverse electron density profile becomes parabolic, capable of guiding a laser pulse with transverse Gaussian intensity profile.

The electric scheme of the high voltage pulse source to create the plasma is shown in figure 3.2. With the thyristor switch opened, a variable high voltage source charges a capacitor bank C_1. A thyristor switch (Behlke type HTS-320-800-SCR, V_{max}=32 kV, I_{max} = 8 kA) is used because of its low turn-on jitter of 1 ns. The maximum voltage of the DC source is 20 kV. The capacitor bank C_1 consists of 4 parallel capacitors of 4.7 nF each. A resistor R_1 of 5 kΩ limits the current through capacitor bank C_1 during charging. With a charged capacitor C_1 and closing the thyristor switch by an external trigger, breakdown occurs through the hydrogen filled capillary and a plasma is created by the high current through the capillary. The current through the plasma is measured by a current monitor (type Pearson current monitor, model 101) connected to an oscilloscope. The current through a capillary with an inner radius of 150 μm, a length of 25 mm and filled with hydrogen at a pressure of 23 mbar can be seen in figure 3.3.
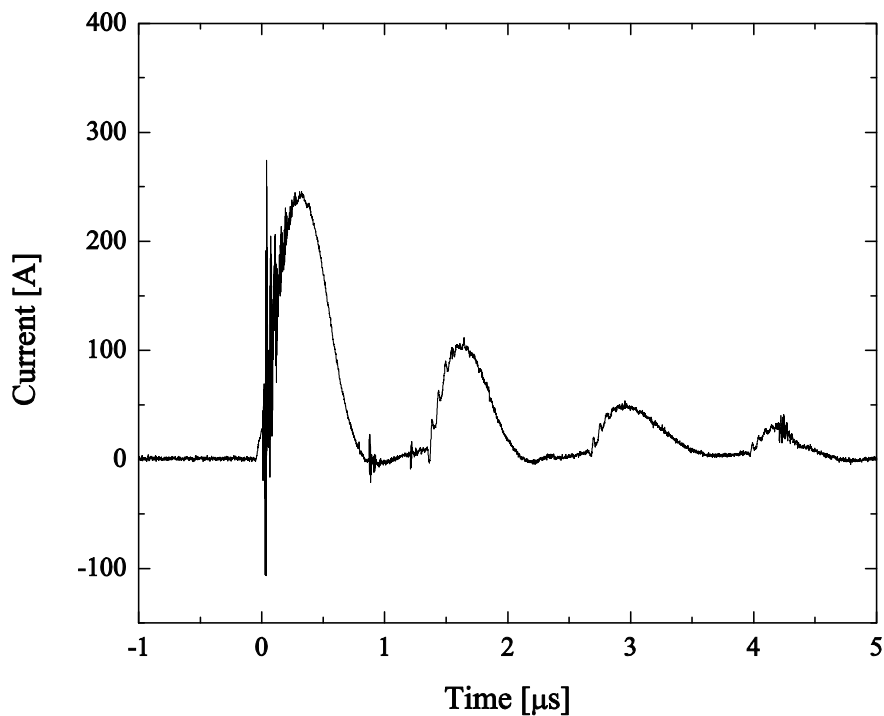
Figure 3.3: Current pulse caused by the high voltage pulse source through a capillary with an inner radius of 150 μm, a length of 25 mm and filled with hydrogen at a pressure of 23 mbar. The external high voltage source was adjusted to 19 kV.

Here, the external high voltage source was adjusted to 19 kV. To limit the rise time of the current through the plasma, a solenoid L with an inductance of 6.7 μH is placed in series with the capacitor bank C_1. This results in a RL circuit oscillating at a theoretical frequency of ~ 500 kHz ($f = 1/2\pi[LC_1]^{1/2}$) which is in fair agreement with the measurement in figure 3.3. A diode D_2 is place parallel to the thyristor switch to prevent the oscillation current flowing through the high voltage supply. The diode D_3 prevents the current through the plasma from becoming negative (see Fig 3.3). The filter combination R_2 and C_2 reduces reflection in the cable between high voltage pulse source and plasma channel whereas diode D_1 is to protect the voltage supply from an accidental negative voltage. The filter combination and diode D_1 are not crucial for functionality of the pulse source. Energy dissipation, which mainly takes place in the plasma and R_2, results in a damped oscillation. As not all energy is dissipated during one cycle, a couple of current pulses through the plasma can be observed in Fig. 3.3. The capacitor C_1 gets charged up to 99% in approximately 0.5 ms (5 times $\tau = R_1C_1$), while the discharge is less than 10 μs. This makes an operating frequency of the high voltage pulse source of up to 1 kHz possible.

3.4 Determination of the guiding settings

The capillary holder and high voltage pulse source (Sec 3.3) used during the guiding experiments is an improved version of the original version developed and tested at the FOM Institute for Plasma Physics 'Rijnhuizen' (The Netherlands) [22]. The guiding properties of this new plasma channel have to be tested at plasma densities of $\sim 10^{24}\,\mathrm{m}^{-3}$ for laser pulses with a $1/e^2$ radius of typically $30 - 50\,\mu m$. This is the typical parameter range for LWA with external injected electrons [1-4]. The determination of the global guiding settings and the first guiding experiments of the plasma channel have been done with 13 ns helium-neon laser pulses. For this a helium-neon laser system is used because the focal spot is easier to change and because the system is much easier to operate compared to a more complicated TW-laser system. TW laser guiding experiments can be found in section 3.5.

3.4.1 Helium-Neon laser setup

In the absence of an ultrafast camera system with a nanosecond-scale shutter time, the laser pulses needed for successful guiding experiment in a plasma channel have to be sufficiently short compared to the time window for guiding which is typically on the order of 100 ns [18, 23, 24]. In figure 3.4 the laser system is described that is used to perform laser guiding experiment in a plasma channel with 13 ns helium-neon laser pulses. The laser light coming from a helium-neon laser (632.8 nm with a power of 2 W) is s-polarized by a linear polarizer. The polarization direction of a second linear polarizer is rotated 90º compared to the first linear polarizer and only transmits p-polarized light. A Pockels cell (spare part of the TW laser system) is placed in between the two polarizers. The high voltage supply for the Pockels cell is tuned to rotate the polarization direction of the helium-neon laser light over 90º in the Pockels cell for a period of 13 ns at an adjustable repetition frequency between 1 and 1000 Hz. This results in 13 ns p-polarized helium-neon laser pulses after the second polarizer. The lens combination $f_1 - f_2$ expands the laser beam by a factor 15 to a collimated laser beam with a $1/e^2$ radius of 7 mm. A lens, f_3, with a focal length of 1 m focuses the laser beam at the entrance of the capillary. The size of the focus spot at the entrance of the plasma channel can be changed relatively easily by changing the ratio f_2/f_1 of the lens combination $f_1 - f_2$. The capillary holder (Fig 3.1) is placed on a motorized 5-axis stage that can position the capillary with a precision of better than 30 nm (New Focus model 8081) and align the capillary to the laser beam. The laser and capillary are well aligned when the axis of the laser and capillary coincide and the laser focus is at the entrance of the capillary. The 5-axis stage and capillary holder are placed on a motorized vertical stage to move the complete capillary holder out of the laser path, in order to image the laser beam at the position of the entrance of the capillary. This vertical linear stage (Newport type UTS100PPV6) has a reversal accuracy of 5 μm. The capillary holder, 5-axis stage and vertical linear stage are placed in a vacuum vessel. The laser profile at the entrance or
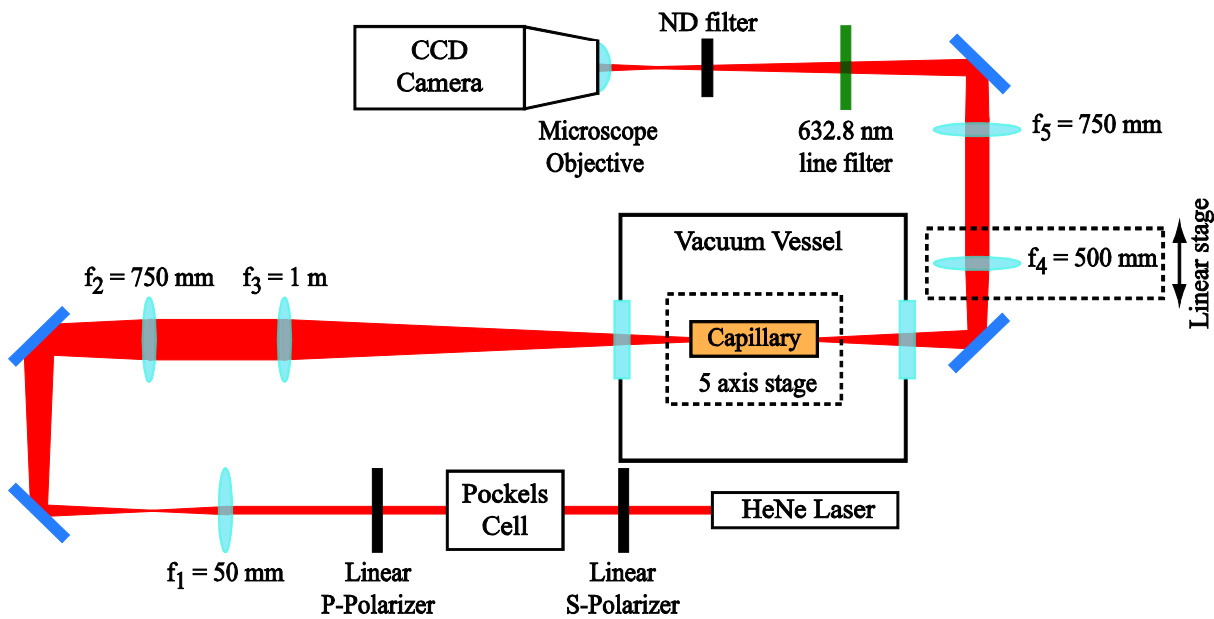
Figure 3.4: Test setup to measure guiding properties of the slow capillary discharge waveguide by using 13 ns helium-neon laser pulses.

exit of the capillary can be imaged on a camera. For this, the lens f_4 (see figure 3.4) collimates the laser beam coming out of the vacuum. A lens f_5 focuses the beam a few centimeters in front of the CCD camera and a microscope objective mounted on the camera makes an image on the CCD Chip (Point Grey type Flea 2). The entrance or exit of the capillary can be imaged on the CCD camera by changing the position of lens f_4 which is placed on a linear stage. The imaging system is calibrated for both positions of the lens f_4, looking at the entrance or exit of the plasma channel. The optical resolution of the system is ~10 μm. As the energy of one helium-neon laser pulse of 13 ns is only ~ 30 nJ, a line filter of (632.8 ± 1) nm is placed in front of the camera to distinguish the laser light from the plasma light. When necessary, a neutral density (ND) filter is inserted in the laser path in order not to overexpose the camera. This makes the imaging of one single helium-neon laser pulse possible even with the plasma ignited. Measurements of the laser beam profiles can be found in section 3.4.4.

3.4.2 Capillary pressure and plasma density

The system to control the hydrogen pressure in the capillary is shown in figure 3.5. The pressure of a hydrogen supply at an absolute pressure of 0.5 bar is reduced by a control valve (MKS type 245). A baratron (MKS type 625BX12MDC1B) connected to a pressure/flow controller (MKS type 244A) measures the hydrogen pressure after the control valve. The controller regulates the control valve so that the pressure measured by the baratron equals the desired pressure in the capillary. Outside the vacuum, the hydrogen flows through a stainless
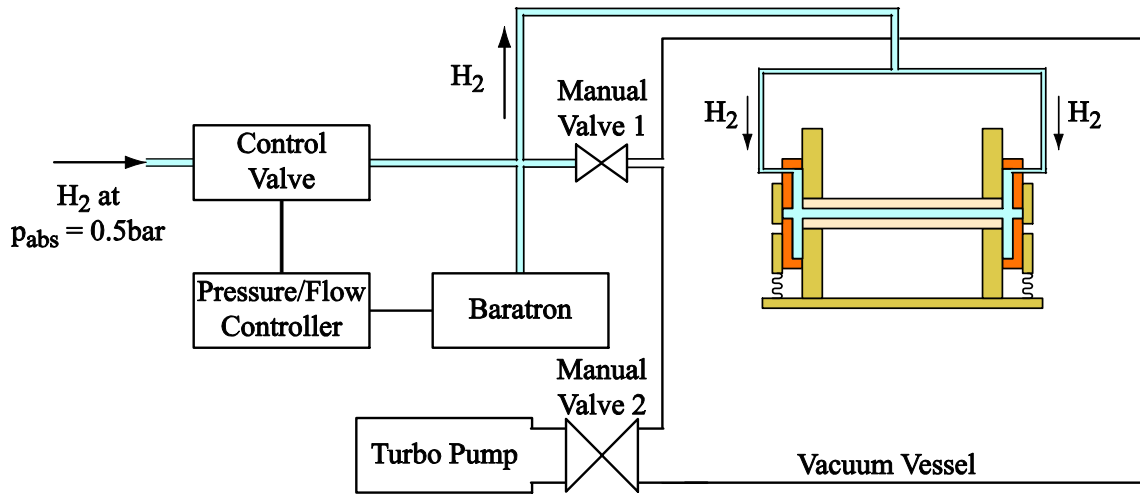
Figure 3.5: Control system of the hydrogen pressure in the capillary.

steel tube with an inner diameter of 4 mm. Inside the vessel, the stainless steel tube is split into two nylon tubes with inner diameters of 2 mm. Each nylon tube is connected to one of the hollow electrodes (see Fig 3.1 and 3.5). To guarantee pure hydrogen in the capillary, the hydrogen filled tubes, hollow electrodes and capillary can be evacuated by opening and closing manual valve 1 before enabling the pressure system.

As the shutters are not completely sealing the cathodes, a small amount of hydrogen escapes from the electrodes. This leak generates a hydrogen flow in the stainless steel and nylon tubes and results in a pressure drop between the baratron and the electrodes. The length of the stainless steel and each of the nylon tubes is approximately 1 m. An estimation of the pressure drop can be made using the Poiseuille equation for a compressible fluid. The relation between the pressure p_i at the entrance and the pressure p_o at the exit of a straight tube with a length L and radius R for a laminar flow with volumetric flow rate Φ, is given by:

$$\Phi = \frac{\pi R^4}{16\eta L}\left(\frac{p_i^2 - p_o^2}{p_0}\right) \tag{3.4}$$

with η the dynamic viscosity of the fluid. For a small pressure drop $\Delta p = p_i - p_o$, this simplifies to:

$$\Delta p = \frac{8\eta L\Phi}{\pi R^4} \tag{3.5}$$

For a stable hydrogen pressure of 10 mbar (1000 Pa) at the position of the baratron, with the shutters closed and a closed manual valve 2 between turbo pump and vacuum vessel, the measured pressure of the vacuum vessel rises at rate of $dp/dt = 0.32$ Pa/s. The volumetric flow rate in the supply tubes is given by:

$$\Phi = \frac{V}{p_t}\frac{dp}{dt} \tag{3.6}$$

with $V = 0.025$ m^{-3} the volume of the vacuum vessel and p_t the pressure in the supply tubes. Assuming a small pressure drop between the baratron and the electrodes, this pressure is approximately 1000 Pa. This results in a volumetric hydrogen flow rate of $\sim 8 \times 10^{-6}$ m^3/s for the stainless steel tube and $\sim 4 \times 10^{-6}$ m^3/s for each nylon tube. The dynamic viscosity of hydrogen is $\eta = 9 \times 10^{-6}$ Pa·s at a pressure of 1000 Pa and a temperature of 300 K [25]. With the use of Eq. (3.5), this results in an estimated pressure drop of ~ 10 Pa over the stainless steel tube and an additional pressure drop of ~ 90 Pa over a nylon tube. This results in an estimate hydrogen pressure drop of $\sim 10\%$ between the measured baratron pressure and the real electrode pressure.

Because the Poseuille equation (Eq. (3.4)) assumes laminar flow, it is necessary to check the Reynolds number:

$$\mathrm{Re} = \frac{2\Phi\rho}{\pi\eta R} \tag{3.7}$$

with ρ the hydrogen density. A Reynolds number of ~ 0.3 is found for the hydrogen flow in the supply tubes confirming the assumption of laminar flow.

The hydrogen pressure in the capillary is assumed to be the same as the pressure in the electrodes. An estimation of the plasma density in the capillary is made by assuming a fully ionized plasma by the current pulse. The plasma density in the capillary n_e is then given by:

$$n_e = \frac{\mathrm{n}p_c}{k_B T} \tag{3.8}$$

where k_B is Boltzmann's constant, p_c the gas pressure in the capillary at a temperature T and n the number of electrons per molecule. When the shutters are opened, some of the gas will flow out through the electrodes. Because the gas volume inside the electrodes is relatively large, the effect on the density inside the capillary will be relatively small. Another effect that is neglected in this estimation is that the porous alumina wall absorbs hydrogen and part of this is desorbed when the wall is heated by the plasma [26]. With these side notes, for the hydrogen-filled capillary, ignited at room temperature at a baratron pressure p_b the plasma density is estimated to be:

$$n_e[10^{24}\,m^{-3}] \approx 0.048\,p_c[mbar] \approx 0.043\,p_b[mbar] \tag{3.9}$$

3.4.3 Clogged up capillaries

The plasma profile given by Eq. (3.2) depends on the plasma density and also on the radius of the capillary. A smaller radius gives a steeper parabolic plasma profile and therefore a smaller matched spot size. The matched spot size W_M (1/e^2 radius) of a laser pulse in a capillary with radius r_c initially filled with a molecular hydrogen density n_{H2}^i is given by [27]:

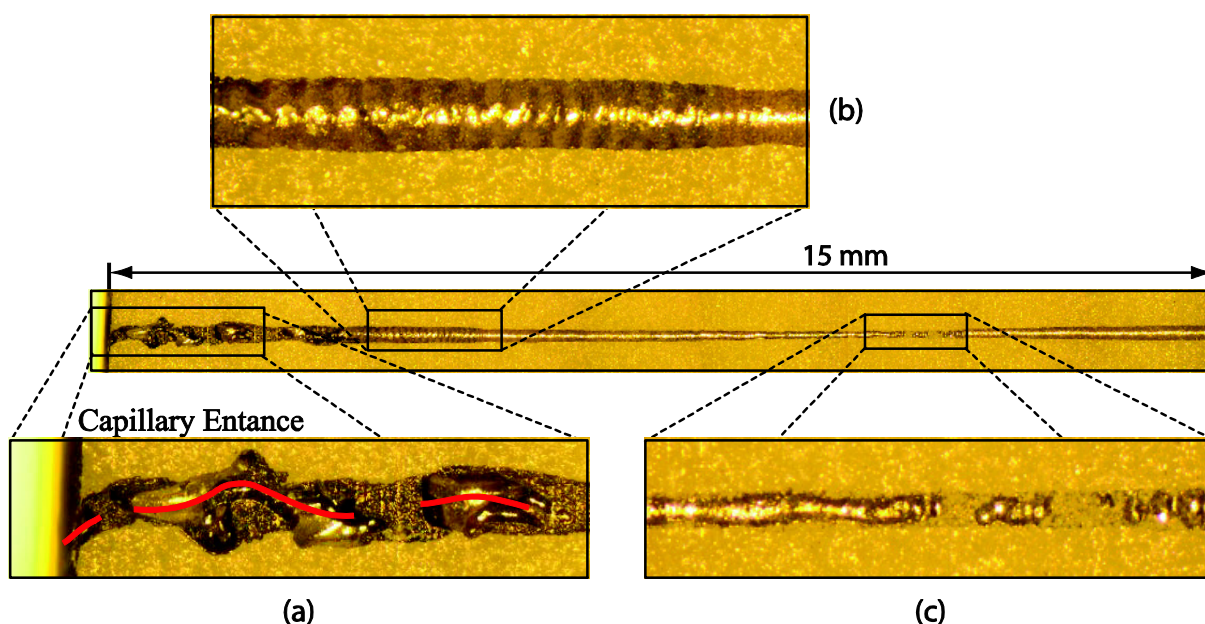$$W_M[m] = 7.3 \times 10^3 \left(n_{H2}^i[m^{-3}]\right)^{-0.25} \left(r_c[m]\right)^{0.5625} \tag{3.10}$$

Figure 3.6: (middle picture) A 15mm long cross section of a used capillary with a length of 30 mm and an inner radius of 100 μm after ~ 100 high voltage pulses (breakdowns) of 20 kV. (a) Magnification of the deformation of the exit of the capillary. The red line indicates the free path for the laser. (b) Magnification of a periodic structure and of (c) narrowing in the capillary.

For the planned LWA experiments with externally injected electrons, the laser has a typical matched spot size of 30 μm − 50 μm and the plasma density needs to be in the range 0.5×10^{24} m^{-3} − 2 ×10^{24} m^{-3} [1, 2]. According to Eq. (3.10), the radius of the capillary has to be at most 100 μm to operate in this parameter range. Capillaries with an inner radius as small as 100 μm are available. These capillaries are used during the helium-neon laser experiments.

The capillaries with an inner radius of 100 μm start to show severe deformation after ~ 100 current pulses through the capillaries generated by the high voltage pulse source. In figure 3.6 a cross section of such a deformed capillary is found. The capillary used had a length of 30 mm. A high voltage pulse of 19 kV with a peak current of ~ 250 A was used and the plasma density was ~ 1 × 10^{24} m^{-3}. During these high voltage/high current pulses, no laser was used. The middle picture shows the first 15 mm of the capillary with the entrance of the capillary on the left of the picture. On the right side of this picture the capillary is more or less unchanged with an inner radius of (still) 100 μm. A magnification of the entrance of the capillary is shown in a Fig 3.6.a. The red line indicates the free path for the laser. In this section the capillary is seriously deformed and there is no straight path for the laser beam to pass through. In Fig 3.6.b a periodic structure in the wall with a period of ~ 100 μm is noticed. The cause of this periodic structure is unknown. The inner radius of the capillary in sections a and b is bigger than the original radius of 100 μm. The alumina from section a and b seems to be deposited in section c (Fig 3.6.c) at a distance of ~ 1 cm from the entrance. At this place the capillary is almost completely clogged up. Similar results were found at the exit of the capillary.
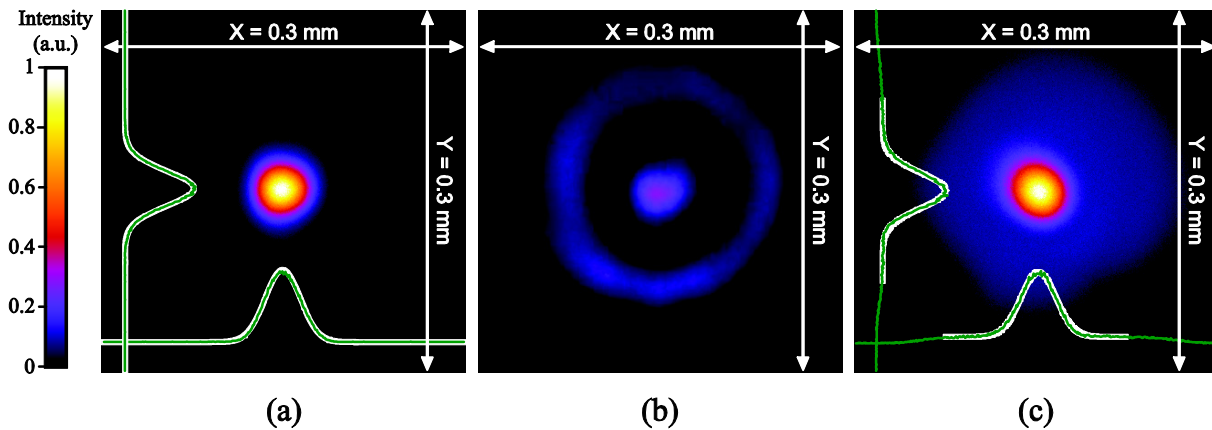
Figure 3.7: Guiding experiment with a helium-neon laser in a capillary with a length of 28 mm, a radius of 100 μm at a hydrogen baratron pressure of 15 mbar. Each picture presents one single helium-neon laser pulse with a length of 13 ns. (a) Laser focus at the entrance of the capillary. (b) Laser profile at the exit of the capillary without plasma and (c) with plasma (guided pulse). The intensity profile at the point of max intensity (green line) with a Gaussian fit (white line) gives a $1/e^2$ radius of 28 μm in (a) and (c).

Capillaries with an inner radius of 150 μm and 200 μm did not show any sign of such deformations even after thousands of breakdowns. The current density in the capillary and the plasma density near the wall possibly becomes too high for the capillaries with an inner radius of 100 μm. This results in an evaporation/ablation of the alumina wall and deposition at another place in the capillary. Successful guiding experiments have been done with these capillaries (see section 3.4.4). However, for the settings used in these experiments capillaries with an inner radius of 150 μm and higher are required to perform prolonged successful and reliable LWA experiments.

3.4.4 Helium-Neon laser beam profiles at guiding

A picture of a typical guiding experiment with a helium-neon laser can be seen in figure 3.7. Each image in figure 3.7 represents one single helium-neon laser pulse of 13 ns. The setup used to perform guiding experiments with a helium-neon laser and the imaging system is described in section 3.4.1. The capillary has an inner radius of 100 μm and a length of 28 mm. A stable baratron pressure of 15 mbar was measured. Using Eq. (3.9), this gives an estimated hydrogen plasma density of $\sim 0.65 \times 10^{24}$ m^{-3} in the capillary after the electrical breakdown by the high voltage pulse source at 15 kV (Sec 3.3). When lowering the vertical linear stage and thus moving the capillary holder out of the laser path, an image of the laser focus at the entrance of the capillary can be made and is shown in figure 3.7.a. The laser beam profile at the exit of the capillary can be seen in figure 3.7.b and 3.7.c. In (b) the capillary is filled with hydrogen (no plasma) and the cylindrically symmetric intensity of the diffraction rings indicates a good alignment between laser and capillary. When the plasma is ignited and a laser pulse

passes through the plasma with a profile as given by Eq. (3.3), the laser pulse is guided (c). The blue background in (c) is the leakage of plasma light through the 632.8 nm line filter. Looking closely at figure 3.7.c, one can observe that the exit of the capillary, which can be distinguished by the blue background, is not completely cylindrically symmetric. This shows the onset of the capillary getting clogged up as described in section 3.4.3. The green lines in (a) and (c) are line-outs of the intensity through the center of the spot. The white lines are Gaussian fits to these line-outs. The Gaussian fits in (c) are corrected for the background. The $1/e^2$ radius of the laser pulse at the entrance (Fig 3.7.a) and the guided pulse at the exit (Fig. 3.7.c) of the capillary are 28 μm in both x- and y-direction (corrected for the optical resolution of 10 μm of the imaging system).

3.5 Terawatt laser pulse guiding experiments

The guiding properties of the operational plasma channel for helium-neon pulses (as described in section 3.4) needs to be tested for ultra-short high-intensity terawatt level laser pulses. TW-scale laser pulses guided through the plasma channel will generate a plasma wave on which externally injected electron can be accelerated.

3.5.1 Terawatt laser pulse profiles at guiding

The helium-neon guiding experiments of section 3.4.4 have been repeated for TW level laser pulses. During these experiments full laser power (2.9 TW) was temporarily not available; the power was limited to 0.13 TW. For the 0.13 TW guiding experiments, the capillary holder, 5-axis and vertical stage - which are necessary for alignment of the capillary on the TW laser - are moved to the setup as described in section 2.3 and figure 2.6. In figure 3.8.a the laser profile (focus) of the 0.13 TW laser at the entrance of the plasma is shown. The $1/e^2$ radius of the laser at the focus is 41 μm. The alumina capillary used for guiding has a length of 25 mm at a baratron pressure of 23 mbar, resulting in an estimated plasma density of ~ 1×10^{24} m^{-3}. To construct a long-term reliable setup and prevent the capillary from clogging up (see sec 3.4.3), a capillary with an inner radius of 150 μm is used instead of the 100 μm prescribed by Eq. (3.10). The high voltage of the pulse source was set to 19 kV. Figure 3.8.b shows the laser light passing through the capillary without plasma and indicates the alignment of TW laser and capillary. In figure 3.8.c the laser profile of the guided 0.13 TW laser pulse is shown. No plasma light is seen as the energy of the laser pulse (6.5 mJ) is orders of magnitude higher than the energy of the plasma light on the camera. The green lines in (a) and (c) are line-outs of the intensity through the center of the spot. The white lines are Gaussian fits to these line-outs. The $1/e^2$ radius of the laser pulse at the exit of the capillary is 35 μm which is slightly smaller than 41 μm at the entrance. This indicates a focusing effect or scalloping of the laser pulse while propagating through the plasma. The sizes of the measured laser spots have been corrected for
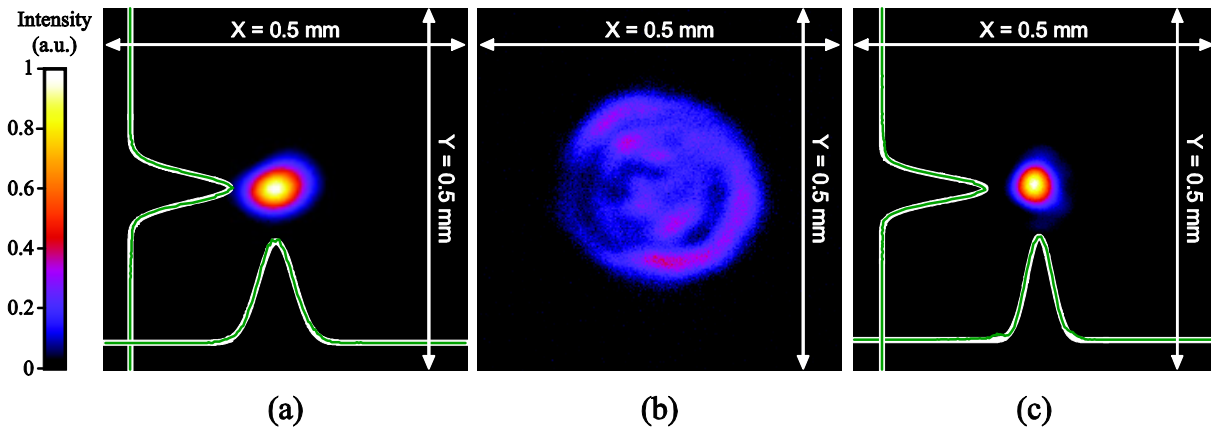
Figure 3.8: Guiding experiment with 0.13 TW laser pulses in a capillary with a length of 25 mm, a radius of 150 μm at a hydrogen pressure of 23 mbar. Each picture presents one single laser pulse. (a) Laser focus at the entrance of the capillary. (b) Laser profile at the exit of the capillary without plasma and (c) with plasma (guided pulse). The intensity profile at the point of max intensity (green line) with a Gaussian fit (white line) giving a $1/e^2$ radius of 41 μm in (a) and 35 μm in (c).

the optical resolution of 10 μm of the imaging system. The guiding of a TW level laser pulse in the plasma channel shows that this laser plasma guiding system operates in the parameter range necessary for LWA experiments with external injected electrons (a $1/e^2$ laser radius of 30 μm – 50 μm for a plasma a density of 0.5×10^{24} m^{-3} – 2×10^{24} m^{-3} [1, 2]).

3.5.2 Guiding versus time

The energy transmittance of the 0.13 TW laser pulses through the plasma has been measured for a capillary with an inner radius of 150 μm, a length of 25 mm at a hydrogen (baratron) pressure of 23 mbar ($n_e \sim 1 \times 10^{24}$ m^{-3}) and a high voltage of 19 kV. The transmitted energy of the laser is measured by replacing the spectrometer in figure 2.6 by a power meter (Coherent 3 Sigma Display with head type: J-10MB-LE). The current pulse versus time through the plasma generated by the high voltage pulse source (see Sec 3.3) can be seen in the lower part of figure 3.9. The transmittance of the laser pulses is measured at different points of time on the current pulse and can be seen in the upper part of figure 3.9. This is done by changing the delay between the laser pulse and the trigger pulse for the high voltage pulse source. Every single measurement in figure 3.9 is the average of the transmittance of ten consecutive laser pulses and the associated error bars indicate the standard deviation of the transmittance of these pulses. The transmittance through the hydrogen-filled capillary before the current pulse (no plasma) is ~ 30% and is indicated by the dotted line. At the first current pulse, the transmittance goes up to ~75%. This is at the maximum of the first current pulse. The laser pulses are guided through the plasma. This was confirmed by looking at the laser pulses' profile at the exit of the capillary. The duration of the time window for guiding on this first current pulse is between
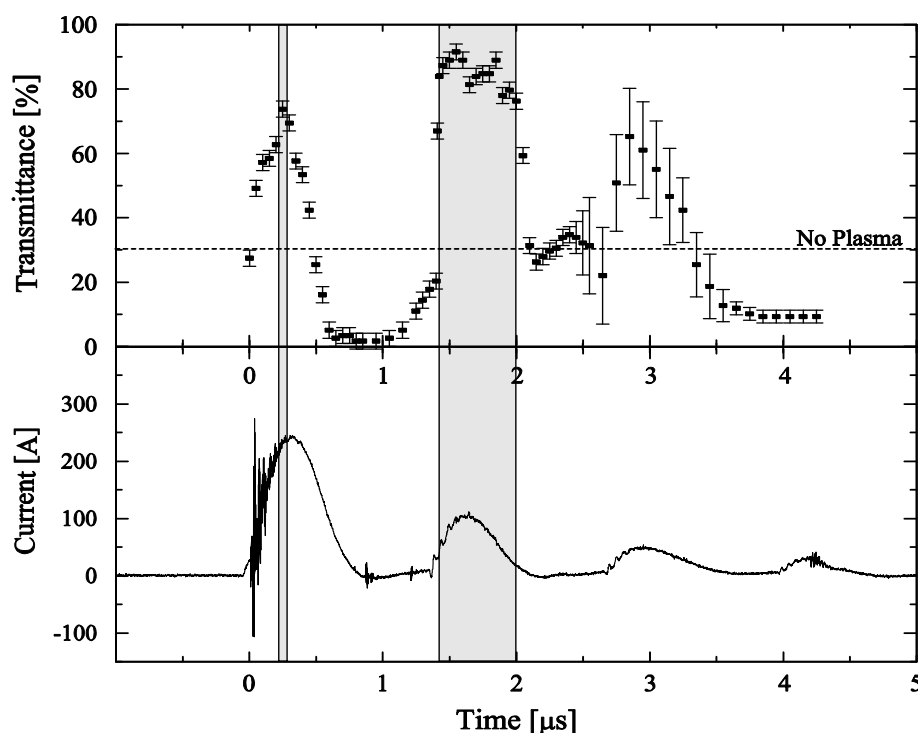
Figure 3.9: <u>Top:</u> Laser transmittance measurement at the exit of a capillary (black dots) versus time for 0.13 TW laser pulses in a capillary with a length of 25 mm, a diameter of 300 μm at a hydrogen pressure of 23 mbar. <u>Bottom:</u> Solid line represents the associated current pulse through the plasma. Dotted line indicates the laser transmittance without plasma. Time windows for guiding are indicated by the grey intervals.

50 ns and 100 ns. After the maximum of the first current pulse, the transmittance decreases and the guiding disappears. This time window for guiding is rather short and the transmittance is poor. The transmittance drops to 0% instead of the expected 30% without plasma, indicating that there is still some plasma present, albeit with a profile that is apparently not suitable for guiding. A secondary breakdown (current pulse) occurs approximately 1.3 μs after the first breakdown, due to the mismatch between the plasma and the high-voltage system, as described in section 3.3. At the second current pulse the transmittance goes up to ~90% and also here guiding is observed. The time window for guiding during this second pulse is much longer, ~ 600 ns. The laser spot of figure 3.8.c is measured on the second current pulse. After the second current pulse, transmittance drops again and also guiding disappears. The later pulses sometimes show guiding, but not consistently, making the next current pulses unsuitable for guiding. The grey intervals in figure 3.9 indicate the time windows for guiding.

All guiding properties during the second current pulse are better compared to the first current pulse. The transmittance is ~ 15% higher and the intensity profile of the guided laser spot at the exit of the capillary better approaches a Gaussian profile. During the first current pulse, the guided laser spot shows more asymmetry. But most important is the time window for

guiding, which is approximately 10 times longer. If the first current pulse is used for guiding, a low turn-on jitter of the thyristor switch (see Sec.3.3 and Fig. 3.2) and breakdown jitter of the plasma is essential because of the small time window for guiding which is typically under 100 ns. A similar time window for guiding has also been reported by others, cf. [18, 23, 24]. For this reason a thyristor switch was chosen which has a typical turn-on jitter of 1 ns. The breakdown jitter is typically tens of nanoseconds which results in an unreliable guiding process with a change of guiding of ∼ 50% on the first current pulse. The breakdown jitter can be made smaller by applying a higher high voltage, which was done in the measurements of figure 3.9, or by igniting the plasma with a laser pulse [23, 28]. A too high HV pulse is adverse for the capillary lifetime (see Sec.3.4.3) while an ignition laser complicates the setup. Both problems can be bypassed by using the second current pulse to guide the laser pulse. In a guiding experiment on the second current pulse, consisting of a sequence of 100 laser pulses at a repetition rate of 2 Hz, all laser pulses were successfully guided through the plasma.

A possible explanation for the better guiding properties on the second current pulse is a better parabolic electron density profile during this pulse. Before the high voltage breakdown, the capillary is filled with molecular hydrogen. The breakdown voltage of a surface discharge is lower than the breakdown through the hydrogen on axis of the capillary. This results in breakdown close to the capillary wall. The current pulse then heats and further ionizes the plasma. Cooling and recombination at the capillary wall stabilizes the plasma. Due to the radial symmetry of the system, a stable plasma will form at the center of the capillary. The current will develop to an on-axis current in this radial symmetric stabilized plasma. Therefore the temperature of the plasma will be higher on-axis, the density will be lower and the density profile will be to first approximation and near the axis parabolic. However this situation takes time to develop. Apparently, only near the maximum of the first current pulse, a plasma profile suitable for guiding is formed, resulting in a short time window for guiding. During some of the experiments on the first current pulse it was noticed that guided laser pulses at the exit of the capillary were near the capillary wall instead of in the center of the capillary. This also indicates that the plasma initially forms near the wall instead of on the axis. Between the first and the second current pulse the current drops to zero but there is still plasma in the capillary. This can be seen by the transmittance which also drops to zero. If the plasma was extinguished and molecular hydrogen was reformed, the transmittance should have been ∼ 30% as was measured without plasma (dotted line). It is suggested that between the current pulses, the plasma stabilizes and becomes more homogeneous and cylindrically symmetric. When the second current pulse starts, plasma is still present in the capillary and a more symmetric plasma forms straight away. This gives a faster formation of the appropriate plasma channel which guides over a much longer time, compared to the guiding on the first current pulse. A suitable guiding profile is formed when the second current pulse is more than ~50 A (see also fig 3.9).

We propose to study the influence of the first and second current pulse on the guiding properties separately by using a pulse source as schematically indicated by Fig. 3.10. Two separate high voltage pulse sources are required. Each pulse source should generate only one
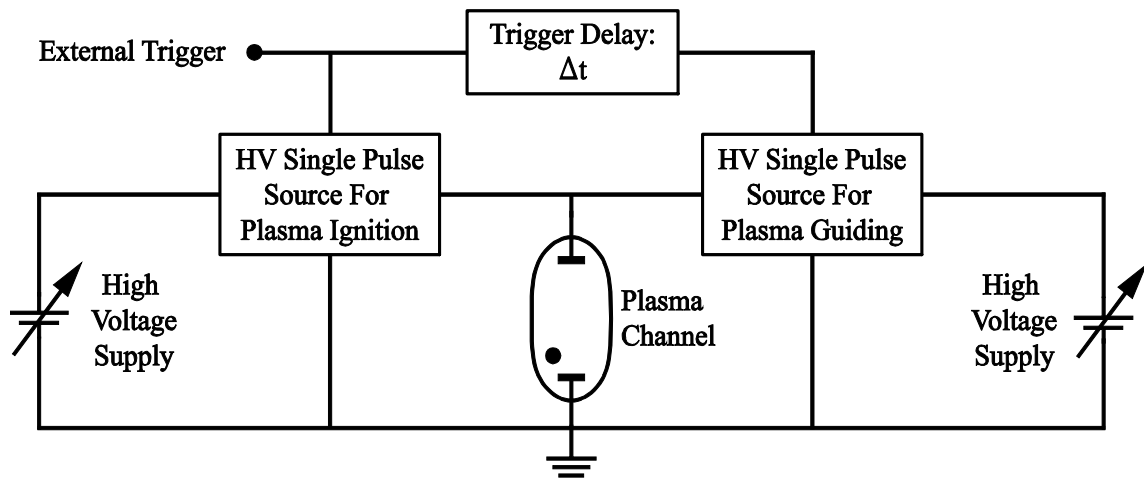
Figure 3.10: Proposal for a HV pulse source to thoroughly examine the guiding properties on the second

single current pulse instead of the multiple current pulses through the plasma as given in figure 3.3. Such a pulse source can be made by placing a resistor in series with diode D_3 in figure 3.2. A well-chosen resistor will dissipate the energy during the second half of the first cycle of the oscillation. During this second half of the first cycle, the capillary is still filled with a plasma which results in a low electrical impedance over the capillary. Placing a resistor in series with diode D_3 would therefore result in a negative current through the plasma. Therefore a diode has to be placed in series with the plasma channel which will prevent a negative current through the plasma channel. Two of such high voltage pulse sources are connected to the plasma channel with each pulse source having its own separate high voltage supply. The first pulse source is used to ignite the plasma and the second pulse source to create an appropriate plasma profile for guiding. A delay between the two pulse sources is determined by a trigger delay *Δt*. As the capacitor bank C_1 (see fig 3.3) consists of 4 capacitors placed in parallel, it is easy to remove or add one or more capacitors to create a shorter or longer current pulse when necessary. The ignitor pulse probably does not need to carry a large current, whereas the second pulse will not require a high voltage. Such dual systems are often applied in plasma systems, such as the common fluorescent lamp. By changing the setting of the high voltage supplies, the trigger delay and the capacitors, the optimal setting may be found for guiding on the second pulse. It is possible that this will result in an even longer, more stable time window for guiding at a lower current. A lower current pulse may also solve the problem of the deformation of the capillaries with a radius of 100 μm which is probably caused by the high current density in the capillary (see Sec 3.4.3). A better control over the igniting and guiding pulse could result in more stable and longer plasma channels that are necessary to accelerate the electrons to a higher energy.
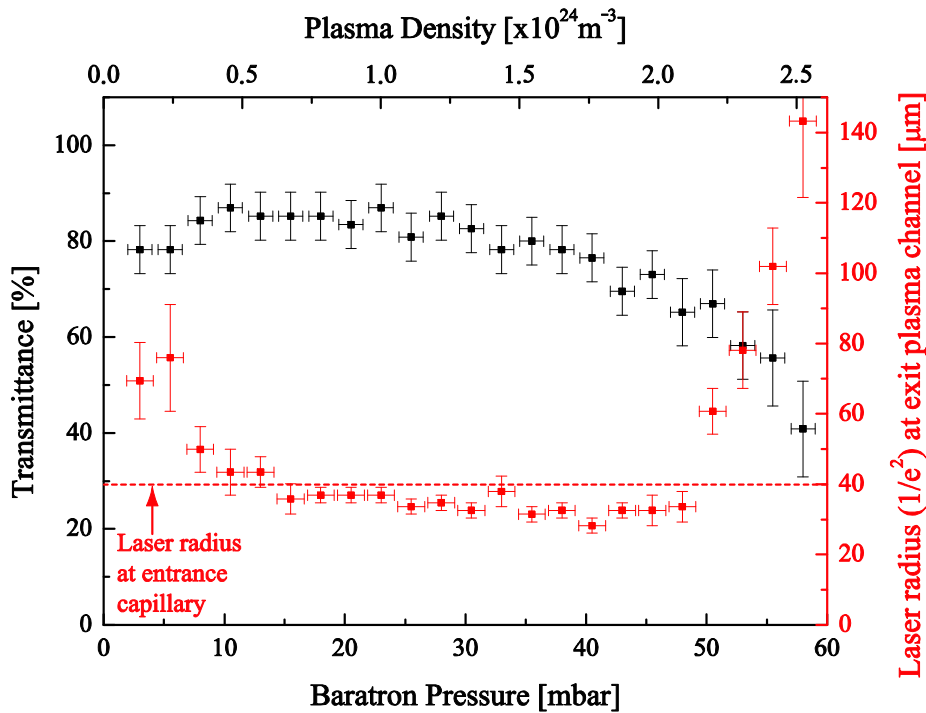
Figure 3.11: Laser transmittance measurement at the exit of a capillary (black dots) versus baratron pressure/plasma density for 0.13 TW laser pulses in a capillary with a length of 25 mm, a diameter of 300 μm at optimal guiding (second current pulse). Red dots represent the associated $1/e^2$ laser radius at the exit of the capillary. Red dotted line indicates the $1/e^2$ laser radius at the entrance of the capillary.

3.5.3 Guiding versus pressure

The effect of the hydrogen pressure (plasma density) on the transmittance and the laser intensity profile at the exit of the capillary has been examined for a capillary with an inner radius of 150 μm, a length of 25 mm and at a high voltage of 20 kV. Guiding experiments were done on the second high voltage pulse because of its bigger time window for guiding and higher transmittance. Laser pulses with a power of 0.13 TW were used during these measurements and the results are shown in figure 3.11. The relation between the measured baratron pressure and the estimated plasma density in the capillary is given by Eq. (3.9). The black dots represent the transmittance of the guided laser pulses through the plasma channel and the red dots the $1/e^2$ radius at the exit of the capillary. A measurement in figure 3.11 is the average of ten consecutive single measurements at the same pressure and the associated error bars indicate the standard deviation of these consecutive measurements. The dotted red line indicates the $1/e^2$ laser radius at the entrance of the capillary.

Successful guiding experiments were done at a baratron pressure between 7 mbar and 50 mbar (0.3×10^{24} m^{-3} − 2.2×10^{24} m^{-3}). This can be seen in figure 3.11 because in this pressure range the size of the laser radius at the entrance and exit are comparable.

Transmittance shows a maximum of ~ 90 % between 10 mbar and 30 mbar (0.4×10^{24} m^{-3} – 1.25×10^{24} m^{-3}) which is therefore the optimal pressure range for LWA experiments. The planned LWA experiments with externally injected electrons require a density around $\sim 1 \times 10^{24}$ m^{-3} [1, 2], which is well within this range. At pressure above 30 mbar the transmittance starts to drop from $\sim 90\%$ at 30 mbar to ~ 75 % at 50 mbar. Above 50 mbar the laser radius at the exit of the capillary increases significantly at a small increase in pressure, indicating that this pressure range becomes unsuitable for guiding experiments with these settings of the laser.

3.6 Conclusion

The guiding properties of an improved version of the plasma channel and high voltage pulse source originally developed at the FOM Institute for Plasma Physics 'Rijnhuizen' has been tested. The plasma channel used in this thesis and the 'Rijnhuizen' plasma channel are both based on the so-called Hooker channel.

During the experiments it was found that the secondary current pulse from the high voltage pulse source also generates a plasma capable of guiding the laser pulses. All the measured guiding properties are found to be better on this second current pulse than on the initial pulse: A better laser spot is found at the exit of the capillary, the transmittance is higher (up to 90%) and the time window for guiding is ~ 600 ns, which is ~ 10 times longer than on the first current pulse. Using the second current pulse to guide a laser pulse through the plasma results in a better, more reliable and more reproducible guided laser pulse. A new high voltage pulse source is proposed to examine the use of the second current pulse for guiding in more detail.

A user-friendly helium-neon laser setup was built for the first guiding experiments to determine the parameter settings required for guiding. These experiments were done with helium-neon laser pulses with a length of 13 nanoseconds. Helium-neon laser pulses with a $1/e^2$ radius of 28 μm were guided over a distance of 28 mm in plasma with a density of $\sim 1 \times 10^{24}$ m^{-3}. These experiments were repeated for terawatt scale laser pulses (0.13 TW) with a $1/e^2$ radius of 41 μm and show similar results as for the helium-neon laser. With the TW laser system, a small focusing or scalloping effect is observed during guiding.

Although the guiding properties of an alumina capillary with an inner radius of 100 μm are better compared to the capillaries with a 150 μm radius, the latter were used in most experiments, because capillaries with an inner radius of 100 μm started clogging up after ~ 100 electrical breakdowns. The clogging up of these capillaries is possibly caused by a too high current density.

The pressure range for successful guiding of terawatt level laser pulses with a $1/e^2$ radius of 41 μm in the hydrogen plasma was found to be between 7 mbar and 50 mbar. This corresponds to a hydrogen plasma with a density between 0.3×10^{24} m^{-3} – 2.2×10^{24} m^{-3}, which is in range with the plasma density of $\sim 1 \times 10^{24}$ m^{-3} required for the planned LWA experiment with externally injected electrons.

References

[1]   W. H. Urbanus, W. van Dijk, S. B. van der Geer, G. J. H. Brussaard and M. J. van der Wiel, *Front-to-end simulations of the design of a laser wakefield accelerator with external injection*, J. Appl. Phys., Vol. 99, 114501, (2006).

[2]   W. van. Dijk, *Simulations and Experiments on External Injection for Laser Wakefield Acceleration*, PhD thesis, Einhoven University of Technology, ISBN: 978-90-386-2316-0, (2010).

[3]   A. G. Khachatryan, F. A. van Goor, K.-J. Boller, A. J. W. Reitsma and D. A. Jaroszynski, *Extremely short relativistic-electron-bunch generation in the laser wakefield via novel bunch injection scheme*, Rev. ST Accel. Beams, Vol. 7, 121301, (2004).

[4]   M. J. H. Luttikhof, *Theoretical investigation of external injection schemes for laser wakefield acceleration*, PhD thesis University of Twente, ISBN: 978-90-365-3071-2, (2010).

[5]   E. Esarey and P. Sprangle, *Interaction of ultrahigh laser fields with beams and plasmas*, Phys. Fluids B, Vol. 4, p. 2241, (1992).

[6]   S. M. Hooker and D. J. Spence, *Investigation of a hydrogen plasma waveguide*, Phys. Rev. E, Vol. 63, 015401, (2000).

[7]   D. J. Spence, A. Butler and S. M. Hooker, *First demonstration of guiding of high-intensity laser pulses in a hydrogen-filled capillary discharge waveguide*, J. Phys. B: At. Mol. Phys., Vol. 34, pp. 4103-4112, (2001).

[8]   A. Butler, D. J. Spence and S. M. Hooker, *Guiding of High-Intensity Laser Pulses with a Hydrogen-Filled Capillary Dicharge Waveguide*, Phys. Rev. Lett., Vol. 89, 185003, (2002).

[9]   C.E. Max and J. Arons, *Self-Modulation and Self-Focussing of Electromagnetic Waves in Plasmas*, Phys. Rev. Lett., Vol. 33, Issue 4, p. 209, (1974).

[10]   P. Sprangle, Cha-Mei Tang and E. Esarey, *Relativistic Self-Focusing of Short-Pulse Radiation Beams in Plasmas*, IEEE Transactions on Plasma Science, Vols. 15, Issue 2, p. 145, (1987).

[11]   S. P. D. Mangles, C. D. Murphy, Z. Najmudin, A. G. R. Thomas, J. L. Collier, A. E. Dangor, E. J. Divall, P. S. Foster, J. G. Gallacher, C. J. Hooker, D. A. Jaroszynski, A. J. Langley, W. B. Mori, P. A. Norreys, F. S. Tsung, R. Viskup, B. R. Walton, and K. Krushelnick, *Monoenergetic beams of relativistic electrons from intense laser-plasma interactions*, Nature, Vol. 431, p. 535, (2004).

[12]   C. G. R. Geddes, Cs. Toth, J. van Tilborg, E. Esarey, C. B. Schroeder, D. Bruhwiler, C. Nieter, J. Cary, and W. P. Leemans, *High-quality electron beams from a laser wakefield accelerator using plasma-channel guiding*, Nature, Vol. 431, p. 538, (2004).

[13]   J. Faure, Y. Glinec, A. Pukhov, S. Kiselev, S. Gordienko, E. Lefebvre, J.-P. Rousseau, F. Burgy, and V. Malka, *A laser-plasma accelerator producing monoenergertic electron beams*, Nature, Vol. 431, p. 541, (2004).

[14]   F. Dorchies, J. R. Marquès, B. Cros, G. Matthieussent, C. Courtois, T. Vélikoroussov, P. Audebert, *Monomode Guiding of 10^{16} W/cm^2 Laser Pulses over 100 Rayleigh Lengths*, Phys. Rev. Lett., Vol. 82, Issue 23, p. 4655, (1999).

[15]   B. Cros, C. Courtois, G. Matthieussent, A. Di Bernardo, D. Batani, N. Andreev and S. Kuznetsov, *Eigenmodes for capillary tubes with dielectric walls and ultraintense laser pulse guiding*, Phys. Rev. E, Vol. 65, 026405, (2002).

[16]   F. Wojda, K. Cassou, G. Genoud, M. Burza, Y. Glinec, O. Lundh, A. Persson, G. Vieux, E. Brunetti, R. P. Shanks, D. Jaroszynski, N. E. Andreev, C.-G. Wahlström, and B. Cros, *Laser-driven plasma waves in capillary tubes*, Phys. Rev. E, Vol. 80, 066403, (2009).

[17]   E. Esarey, P. Sprangle, J. Krall and A. Ting, *Self-Focusing and Guiding of Short Laser Pulses in Ionizing Gases and Plasmas*, IEEE Journal of Quantum Electronics, Vol. 33, Issue 11, p. 1879, (1997).

[18]   C. McGuffey, M. Levin, T. Matsuoka, V. Chvykov, G. Kalintchenko, P. Rousseau, V. Yanovsky, A. Zigler, A. Maksimchuk, and K. Krushelnick, *Guiding of 35 TW laser pulses in ablative capillary discharge waveguides*, Phys. Plasmas, Vol. 16. 113105, (2009).

[19]   W. P. Leemans, B. Nagler, A. J. Gonsalves, Cs. Tóth, K. Nakamura, C. G. R. Geddes, E. Esarey, C. B. Schroeder, and S. M. Hooker, *GeV electron beams from a centimetre-scale accelerator,* Nature physics, Vol. 2, p. 696, (2006).

[20]   http://www.agateproducts.co.uk/.

[21]   www.kubra.nl.

[22]   P. S. Antsiferov, M. R. Akdim, and H. T. van Dam, *Direct measurement of the matched spot size in a slow capillary discharge optical* , Rev. Sci. Instrum., Vol. 78, 123107, (2007).

[23]   B. Greenberg, M. Levin, A. Pukhov and A. Zigler, *Low jitter capillary discharge channels*, Applied Physics Letters, Vol. 83, Issue 14, (2003).

[24]   M. Levin, A. Pukhov, A. Zigler, K. Sugiyama, K. Nakajima, R. F. Hubbard, A. Ting, D. F. Gordon, P. Sprangle, and D. Kaganovich, *Long plasma channels in segmented capillary discharges*, Physics of Plasmas, Vol. 13, 083108, (2006).

[25]   L. I. Stiel and G. Thodos, *Viscosity Of Hydrogen in the Gaseous and Liquid States for Temperatures up to 5000 K* , I&EC Fundamentals, Vol. 2, Issue 3, p. 233, (1963).

[26]   B. H. P. Broks, K. Garloff, and J. J. A. M. van der Mullen, *Nonlocal-thermal-equilibrium model of a pulsed capillary discharge waveguide*, Phys. Rev. E, Vol.71, 016401, (2005).

[27] B. H. P. Broks, W. van Dijk and J. J. A. M. van der Mullen, *Parameter study of a pulsed capillary discharge waveguide* , J. Phys. D: Appl. Phys., Vol. 39, pp. 2377–2383, (2006).

[28] M. Liu, A. Deng, J. Liu, R. Li, J. Xu, C. Xia, C. Wang, B. Shen, Z. Xu, and K. Nakajima, *Low density and long plasma channels generated by laser transversely ignited ablative capillary*, Rev. Sci. Instrum., Vol. 81, 036107, (2010).

Chapter 4

The RF-photogun.

4.1 Introduction

To enable an independent study of the effects of the plasma conditions, laser parameters and injected electrons in the plasma accelerator, these three different components need to be separately controllable. This condition is already fulfilled for the TW laser (Chap. 2) and the plasma (Chap. 3). It is believed that the accelerated electron bunch in a LWA can be more reliable by controlling the injected electrons in the LWA [1]. Therefore an external electron source that injects electron in the LWA is desirable. Since an RF-photogun is the brightest pulsed electron source presently available [2], this is the best candidate for an external injector. An added advantage of using an external source for the injection of electrons is that acceleration becomes possible not only in the nonlinear wakefield regimes [3-5], but also in the linear regime [3, 6, 7]. The linear regime requires much less laser power (sub-10 TW) and therefore LWA in this regime can possibly be operated at a higher repetition rate.

This chapter describes the RF-photogun that was built for the purpose of injecting electrons in a LWA. It concerns the cavity design (Sec. 4.2), basic cavity theory (Sec 4.3.1), electric field distribution in the cavity (Sec. 4.3.2) and RF characterization (Sec. 4.3.3 and Sec 4.3.4). Electron bunch measurements can be found in chapter 5.

4.2 Design of the RF-photogun

The RF-photogun injector is a 2.6 cell cavity working in the S-band range at a frequency of 2.998 GHz. A cross section is shown in Fig. 4.1. The accelerator consists of 3 coupled pillboxes which are clamped together. The cells are made from high purity oxygen free copper (type C10100) by single-point diamond turning with 1 μm accuracy, following the design (using SUPERFISH) that was made with the same precision. By clamping the cells, deformation after construction by heating - which is necessary when brazing - is eliminated. Combining the clamping construction and micrometer precision manufacturing of the individual cells makes tuning plungers redundant. The length of the first cell is chosen to achieve maximum acceleration. The irises between the cells have an elliptically shaped cross section. As a consequence the maximum electric field strength is not on the irises, but on the cathode [8]. When breakdown occurs, it will be mostly on the cathode, which can be removed relatively easily for cleaning or polishing, because of the clamping system.

Instead of the more commonly used sideways in-coupling of the RF power in the cavity, a coaxial input-coupler was designed and built. The design was originally proposed by DESY (Deutsches Elektronen Synchrotron) for use at 1.3 GHz. It was redesigned for 3 GHz and successfully used in previous versions of this electron gun at Eindhoven University of Technology [9, 10]. The coaxial input coupler makes the construction completely cylindrically symmetric. The cavity can now be placed inside a solenoid, whereas in most other designs, the solenoid has to be placed just behind the exit of the cavity because of the sideway ports that feed the RF-power in the cavity. Placing the cavity inside the solenoid is beneficial to the bunch quality (bunch length and emittance), as will be explained in more detail later in this section. Also, the coaxial coupler makes the field inside the cavity more symmetrical, which is also advantageous for the quality of the electron bunches. The coaxial input coupler transfers the RF power coming from a rectangular waveguide in the TE_{10} mode to the TM_{010} mode in the cavity. The RF power source is a klystron, producing a peak power of 10 MW (Thomson TH2157A). Inside the cavity, a standing wave is generated with a longitudinal electric field which accelerates the electrons. The cavity is mounted inside a stainless steel can, thereby separating the electric and vacuum functions of the construction. The stainless steel holder only serves to maintain the vacuum, preventing unwanted strain on the copper cavity structure. The normal operating pressure is $\sim 1 \times 10^{-7}$ mbar.

Electrons are produced at the copper cathode plate by photoemission of an incoming 50 fs, 266 nm laser pulse and are accelerated by the cavity's electric field. The magnetic solenoid lens around the cavity serves multiple functions aimed to keep the emittance of the bunch low and the length of the bunch short. It keeps the accelerating electron bunch in the cavity collimated and the radius small. Because the electric field as a function of radius inside the cavity is only constant close to the axis, the bunch radius has to remain relatively small to prevent electrons from sampling the higher order field components which would cause an increase in emittance and energy spread. In addition, path length differences between electrons on the axis and those
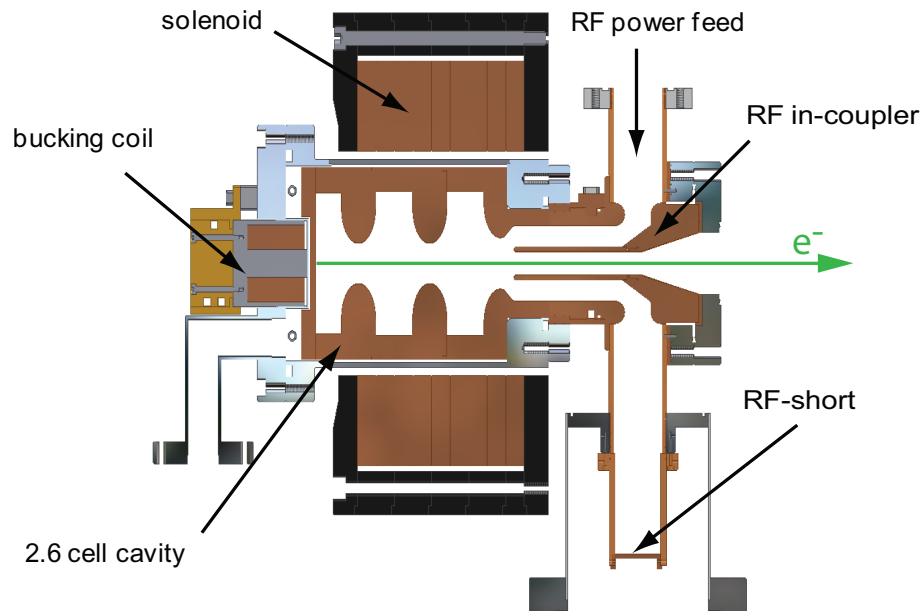
Figure 4.1: Cross section of the RF-photogun, coaxial input coupler of the RF-power, magnetic solenoid lens and bucking coil. The green arrow represents the direction of electron accerelation and propagation.

further away are minimized. This keeps the bunch length at the exit of the accelerator short. Finally, the solenoid lens compensates for the exit kick from the divergence of the electric field at the end of the accelerator, which acts as a negative lens for the electrons exiting the cavity. At the place of electron creation on the cathode, the magnetic field due to the solenoid has to be nulled. Otherwise, the electrons would obtain an extra net azimuthal momentum which leads to an increase of the emittance. A smaller solenoid (bucking coil) is placed outside the vacuum at the back of the cathode plate to null the magnetic field at the surface of the cathode.

The temperature of the cavity is controlled by a water circuit which is connected to the both cathode plate and the exit cell of the cavity. Temperatures of the first and exit cell of the cavity are measured by thermocouples. A PI controller adjusts the water temperature to assure a cavity operating temperature of 30.00 °C with a stability of 0.05 °C [10]. Precise temperature control is essential in this design of the accelerator to keep the cavity resonant with the RF oscillator.

A detailed analysis of the absorption spectrum and the field balance inside the cavity is given by Van Dijk [11]. Three different modes can be excited, the 0-,$\pi/2$- and π-mode. The peaks in the absorption spectrum are well separated, in accordance with the SUPERFISH simulations that were used for the design of the cavity. For optimal acceleration the cavity needs to be operated in the π-mode.

4.3 Properties of the RF- photogun

A basic theoretical description of the working principle RF accelerator is presented in Sec. 4.3.1. This abridged version of the theory is based on the work presented in refs [9, 12]. A more thorough theoretical description can be found in refs [9, 11-13].

4.3.1 Pillbox cavity theory

A pillbox is typically a hollow copper cylinder which is closed at the ends. According to the Maxwell equations the only two types of standing wave possible in the pillbox are the TE and the TM mode of which only the latter can be used to accelerate charged particles along the axis of the cylinder (z- axis). The EM field in a pillbox in the TM_{010} mode can be seen in Fig. 4.2.a. In this mode the electric field is parallel to the z-axis and the magnetic field only has a tangential component. The shape of the E-field in the z direction versus the radius of the pillbox is presented in Fig 4.2.b. and is maximum on the z-axis. Fig. 4.2.c shows that the accelerating electric field is constant along the z-axis. Therefore those pillboxes are most suitable to accelerate charged particles on the axis of the cylindrical structure. In these figures R is defined as the radius of the pillbox and d is the length of the pillbox.

The resonant angular frequency of a pillbox operating in the TM_{010} mode is given by:

$$\omega_0 = \frac{p_{01}}{R\sqrt{\mu\varepsilon}},$$
(4.1)

with μ and ε the permeability and permittivity of the material inside the cavity. $p_{01} = 2.405$ is the first root of the zero[th] order Bessel function J_0. The cavities used in the experiments here are not filled with a substance and operate at vacuum so Eq. (4.1) becomes:

$$R = \frac{cp_{01}}{\omega_0}.$$
(4.2)

For a single closed pillbox cavity operating at a frequency of $f = 3$ GHz, the radius R of the pillbox is 38.3mm. The electric field strength as function of time and radius is given by:

$$E_z(r,t) = E_0 J_0\left(\frac{rp_{01}}{R}\right)\cos(\omega_0 t).$$
(4.3)

Here E_0 is the maximum accelerating electric field on the z-axis and independent of z. Only half of the period can be used for accelerating charged particles in the z-direction as the electric field changes sign after π rad (Eq. (4.3)). Therefore, a particle propagating at the speed of light c has to pass the complete pillbox in half a period time. This corresponds to a pillbox length of:

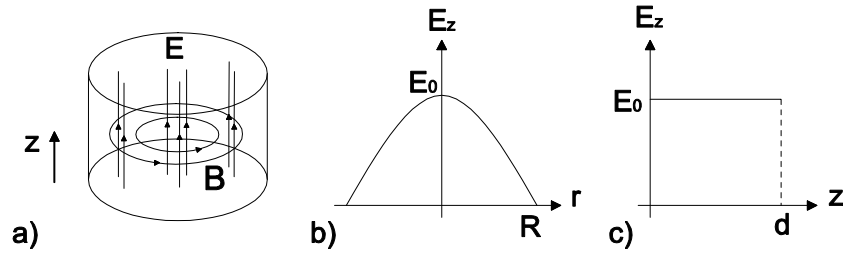$$d = \frac{\pi c}{\omega_0}.$$
(4.4)

Figure 4.2: EM fields in a pillbox in the TM010 mode (a), electric field in the z direction versus radius (b) and electric field on the z-axis in the z direction (c) [9].
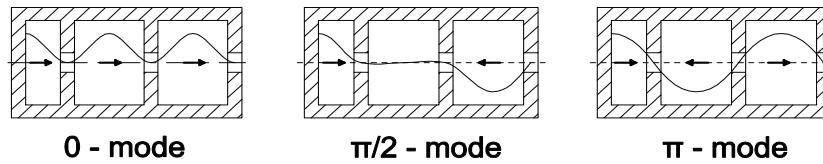

Figure 4.3: Different modes for a 2.6 cell accelerator with the associated on –axis electric field with maximum electric field on the cathode [9].

At an operating frequency of 3 GHz, the optimal pillbox length is therefore 50 mm. A charged particle travelling at a velocity *c,* passing a pillbox in half a period on the optimal phase of the electric field will gain a maximum kinetic energy ΔE_{kin} of :

$$\Delta E_{kin} = \frac{2cE_0}{\omega_0}.$$

$$(4.5)$$

For a pillbox with maximum electric field of 100 MeV/m, this corresponds to a maximum energy gain of 3.18 MeV.

To accelerate charged particles to energies over 3.18 MeV, pillboxes are coupled together and a hole is made on-axis to make a passage for the particle to move from one cell to the next. The RF-wave that provides energy to the cavity also passes through the holes. The resonant frequency of an accelerator consisting of N coupled pillboxes will break up in N different modes with a phase difference between consecutive pillboxes, ranging for 0 to π in N steps. In the 0-mode all cells (pillboxes) are in phase. This is the lowest resonant frequency for the structure. In the π-mode each consecutive cells is in the opposite phase and the resonant frequency is the highest for this structure. The used RF-photogun consists of 3 coupled pillboxes. The first one is a 0.6 cell pillbox to optimize the energy of accelerated electrons at the exit of the photogun and assure a high accelerating field at the cathode where the electrons are emitted. For a 2.6 cell cavity there are three different modes: 0-, π/2- and π-mode (Fig.4.3). The 0-mode cannot be used to accelerate charged particles. Particles that are accelerated in the first cell will reach the second cell after some time. These electrons experience a decelerating

field in the second cell as the field in the second cell has changed direction in the time that the electrons pass through the first cell. Under the right conditions and cell length, the $\pi/2$-mode can be used for acceleration, but in the π-mode the electrons can be accelerated in the maximum field for each cell and is therefore the optimal mode for acceleration, since maximum fields are needed to keep the electron bunches as short as possible.

To generate the electric fields described above, RF power is coupled into the cavity structure. The change of stored energy in the cavity is given by:

$$\frac{dU(t)}{dt} = P(t) - P_{loss}(t) = P(t) - \frac{\omega_0}{Q_{unl}} U(t), \tag{4.6}$$

with U the stored energy, P the absorbed RF-power and P_{loss} the power lost in the cavity, mainly by the finite conductivity of the cavity walls in which currents flow. Q_{unl} is defined as the unloaded quality factor of the cavity and is a measure of how long energy can be stored in a cavity. The klystron that is used to generate the RF power has a Q-factor Q_{kl}. When the klystron and cavity are connected together, the Q-factor of the complete system is given by Q (without subscript) which is commonly called the loaded Q-factor. The relation between these Q's is given by:

$$\frac{1}{Q} = \frac{1}{Q_{kl}} + \frac{1}{Q_{unl}}. \tag{4.7}$$

The system is designed so that the klystron matches the cavity, i.e. both have an impedance of 50 Ω at the resonant frequency. In this case klystron and cavity both absorb 50 % of the power and maximum power is transferred to the cavity. When klystron and cavity are matched Q_{kl} equals Q_{unl} so that $Q_{unl} = 2 \times Q$.

The energy stored in the cavity is directly related to the electric field by:

$$U = CE_0^2. \tag{4.8}$$

C is a constant that depends on the exact structure of the used cavity. SUPERFISH simulation shows that a maximum on-axis electric field of 96.8 MV/m corresponds to a stored energy of 6.68 J in the cavity. Design of the cavity (Fig. 4.1) and SUPERFISH simulations can be found in van Dijk [11]. The constant C was determined for the used 2.6 cell cavity and results in:

$$E_0[\text{MV/m}] = 37.5\sqrt{U \text{ [J]}}. \tag{4.9}$$

The fraction of absorbed RF-power of an ideal single cavity as function of the frequency can be approximated by a single Lorentzian peak function and is given by [9, 11, 14]:

$$A = A_{max} \frac{BW^2}{4(f - f_0)^2 + BW^2}, \tag{4.10}$$

with A_{max} the maximum percentage of absorbed power of the cavity with a resonant frequency f_0 and a bandwidth BW (FWHM) of the Lorentzian peak function. Therefore, for a real cavity

with parasitic absorption and with N different modes, the fraction of absorbed RF-power can be approximated by the summation of N Lorentzian peak functions and has to be corrected for the parasitic absorption and is given by:

$$A = A_p + \left(1 - A_p\right) \sum_{i=1}^{N} A_i \frac{BW_i^2}{4\left(f - f_{0,i}\right)^2 + BW_i^2}. \tag{4.11}$$

Here A_p is the percentage of overall parasitic absorption in the system and A_i is the percentage of absorbed power by the cavity at the ith resonance peak with resonance frequency $f_{0,i}$. BW_i is the bandwidth (FWHM) of the ith resonance peak and is related to its associated loaded Q-factor Q_i by:

$$BW_i = \frac{f_{0,i}}{Q_i}. \tag{4.12}$$

4.3.2 Electric field distribution in the cavity

The maximum electric field in a cavity is limited by vacuum breakdown and is typically less than ~100 MV/m. As the RF-photogun operates in the π-mode, all three cells can be used for acceleration. To assure maximum acceleration of the charged particle in the accelerating structure, an equal (maximum) electric field in the three cells is required. This can be determined by measuring the electric field distribution in the cavity along the axis.

The field distribution is measured using the 'bead-ball method' [15]. A 4-mm diameter nylon bead was connected to a 150-μm diameter nylon wire and lowered along the axis in the cavity. According to perturbation theory, the small bead ball in the cavity generates a frequency shift which can be measured with a network analyzer. The relation between the frequency shift $\Delta\omega$ and the electric field E at the position of the bead ball inside the cavity is given by: $\Delta\omega/\omega \propto E^2$. The frequency shift depends on the position of the bead ball on the axis of the cavity. The local on-axis electric field in the π-mode has been measure and is shown in Fig. 4.4.

The measured on-axis field is in reasonable agreement with the design simulation that is represented by the solid line. However, there is a clear deviation between measurements and simulation in the first cell, close to the cathode. During the measurements, the cathode plate was replaced by a copper plate with a small hole (200 μm) in the centre to create a passage for the nylon wire. A possible explanation for this deviation is that the screws that put the copper plate and the first cell together were not tightened enough. This locally reduces the conductivity between the copper parts of the cavity and also reduces the on-axis electric field. A more thorough study of the electric field balance can be found in Ref. [11].
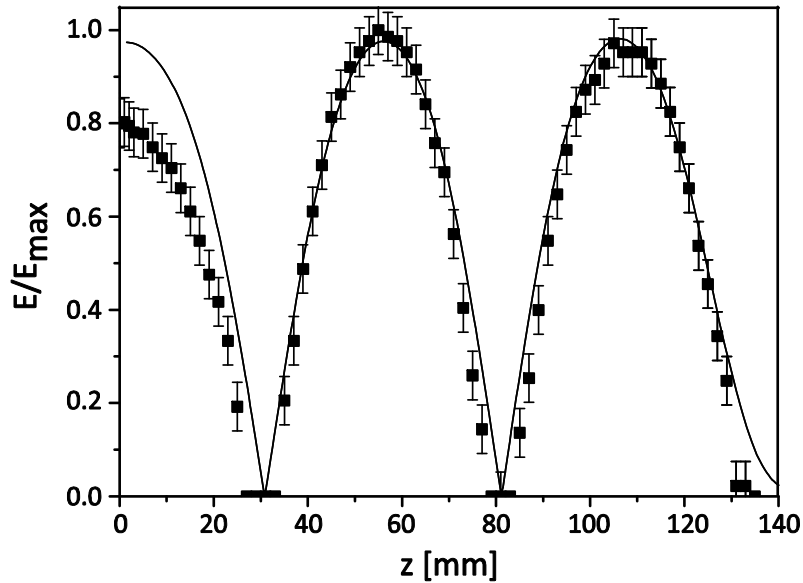
Figure 4.4: On-axis electric field distribution in the π-mode of the RF-photogun. Dots are measurements and the solid line represents the design SUPERFISH simulation [11].

4.3.3 Absorption spectrum

The RF power generated in the klystron is sent through an RF waveguide towards the cavity. An RF window is placed between the RF waveguide and the cavity to separate the vacuum in the cavity from the SF_6 gas at a pressure of 1bar in the RF-waveguide. The RF window is transparent for the RF power coming from the klystron. The SF_6 in the waveguide is necessary to prevent breakdown.

Low power tests have been performed on the cavity using a network analyzer type HP 8753C. To approach the real operational conditions as mentioned above as close as possible, the waveguide just above the RF-window was removed and the network analyzer was connected just above the window. By doing this, the cavity can be tested under vacuum conditions. The network analyzer sends low power RF waves to the cavity and measures the reflected and absorbed part in the cavity. The measurement of the absorption spectrum can be found in Fig. 4.5. The dots represent the measurements from the network analyzer and the solid line represents the fitted curve of Eq. (4.11).

This measurement was done with the antenna of the input coupler 3 mm shorter than the original design. This was done to optimize the stored energy in the cavity and thus maximize the on-axis electric field. A more complete description of the optimization can also be found in reference [11].

With the fit parameters from Eq. (4.11) and the use of Eq. (4.12) we can find the resonance frequency, absorption and the loaded Q-factor for the different modes. These are given in table 4.1.
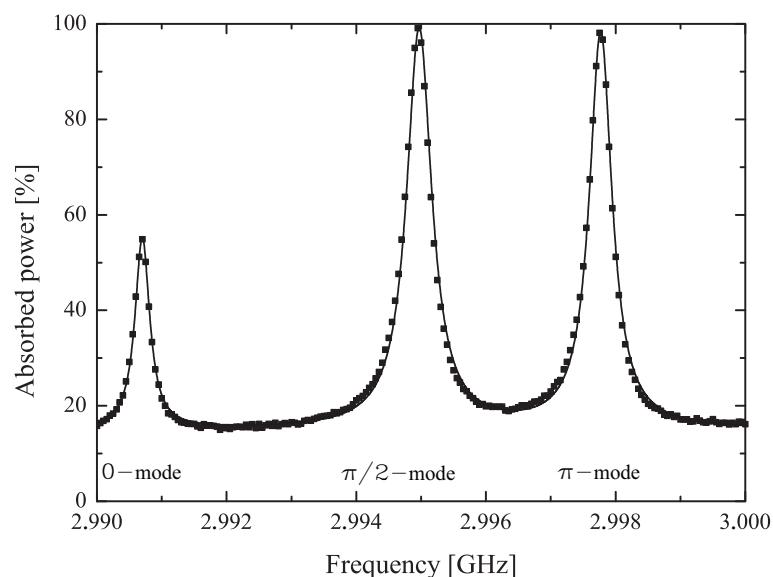
Figure 4.5.: Measured (dots) and fitted (solid line) spectrum of the absorbed power in the cavity for the 0-, $\pi/2$- and π-mode.

The three resonance peaks in Fig. 4.5 are clearly separated which is a prerequisite if we want to operate in a single mode. The measured resonance frequency in the π-mode is 2997,8 MHz using the network analyzer. During high power operation, the frequency is monitored using a frequency counter. This frequency is found to be 2998.5 MHz. The SUPERFISH design value is 2998.5 MHz. Simulations and measurements have all been done at 30ºC.

The loaded Q-factor is found to be 7108, which is above the design value of 6562. Possible explanations for this high value are an error in the estimation of the antenna length or a slight mismatch between cavity and network analyzer. The impedance of the network analyzer is 50 Ω. To have an optimal power transfer from network analyzer to cavity, the impedance of the cavity also needs to be 50 Ω. This can be tuned by changing the position of the endplate (RF-short, see also Fig. 4.1) of the RF-waveguide and is possibly not in the optimal position. Further tweaking of the antenna length and RF-short could be performed to match the measured values even more closely to the design values. However, in the present configuration, these values are well within the desired range for operation.

Table 4.1: Absorption, resonant frequency and loaded quality factor of the RF-photogun for the 0-, $\pi/2$- and π-mode

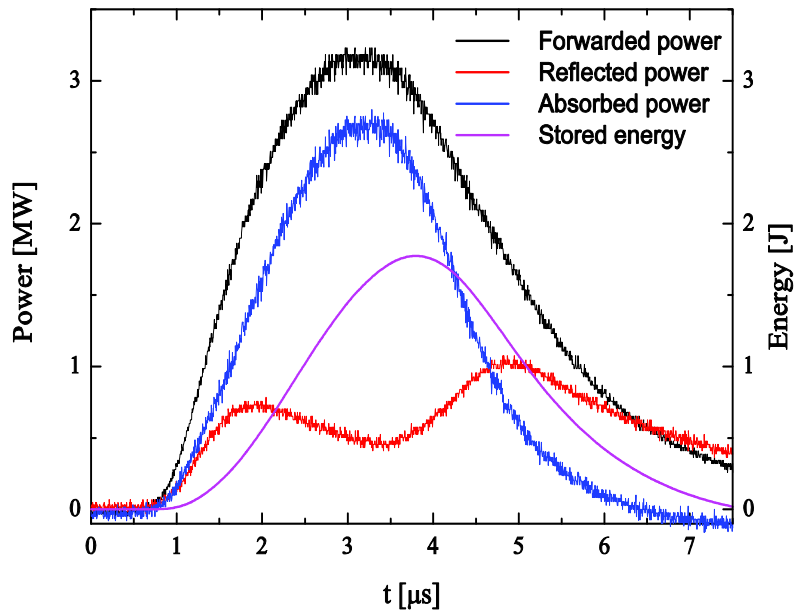|	0-mode	$\pi/2$-mode	π-mode
A	0.47	0.985	0.975
f_0 **[MHz]**	2990.7	2995.0	2997.8
Q	10869	6379	7108

Figure 4.6.: Measurement of the forward (black), reflected (red) and absorbed power (blue) in the cavity versus time. The stored energy in the cavity is calculated from these measurements and shown as the purple solid line.

The parasitic absorption A_{p} is around 15 % (Eq. (4.11)), as can be seen from the position of the baseline in figure 4.5. This absorption is almost completely caused by the RF-window which was measured separately and showed absorption of around 12 %.

4.3.4 Absorbed power and stored energy

High power measurements have been done with two RF diodes connected with the RF waveguide. The first RF diode records the forwarded power from the klystron into the cavity and the second one the power reflected from cavity. The RF power produced by the klystron is in the 10 MW range and is delivered in a pulsed mode. A typical picture of the forwarded and reflected power as function of time can be seen in Fig. 4.6. This measurement was taken with klystron and cavity settings that produce electron bunches with a kinetic energy of 3.7 MeV. The energy of the accelerated electrons was measured with a magnetic spectrometer as described in section 5.5.1.

The black line in figure 4.6 is the forward power and the red line is the reflected power. The difference between forward and reflected power is the absorbed power in the cavity and is represented by the blue line. The length of the forward pulses is 3.5 μs (FWHM), while the absorbed power has a pulse width of 2.5 μs. The reason for the difference in pulse duration between forward and absorbed power is due to the fact that the use of a klystron amplifier gives rise to changes in the RF frequency during the pulse. When the power increases, the frequency

is slightly lower and when the power decreases the frequency is slightly higher than the resonance frequency of the cavity [9]. Only if the frequency is within the bandwidth of the cavity, power is absorbed efficiently.

For the settings of figure 4.6, the maximum forward power is 3.2 MW and the maximum absorbed power is found to be 2.7 MW. With the use of Eq. (4.6) and the measured parameters defined in table 4.1, we can calculate the stored energy in the cavity. This is represented by the purple line in Fig. 4.6. The length (FWHM) of the pulse is ~ 3 μs with a maximum stored energy of 1.77 J in the cavity. The peak in stored energy comes 0.6 μs after the maximum forward power. The maximum electric field in the cavity calculated with Eq. (4.9) is 49.9 MV/m. Implementing this maximum on-axis electric field in a GPT [16] (general particle tracer) simulation, results in a simulated kinetic energy of (3.45 ± 0.1) MeV at the exit of the RF photogun. This is in reasonable agreement with the measured 3.7 MeV. The difference can be attributed to systematic uncertainties in the equipment used to measure the forward and reflected power. To measure the RF-power, a 90 dB attenuator is required between RF-diodes and oscilloscope. This generates the biggest uncertainty in the RF-power measurement and can explain the lower simulated value of 3.45 MeV. The energy measurement of 3.71 MeV with the use of a spectrometer is a direct measurement of the energy of the electrons (see section 5.2 and 5.5.1) and therefore more accurate. The estimate of the electric field above is merely to check the consistency of the different methods.

4.4 Conclusions and discussion

The measurements on the performance of the cavity show reasonable agreement with the design. The three different modes in which the cavity can operate are well separated. At the resonance frequency 2.998 GHz, only the π-mode (the mode needed for effective acceleration) is excited. Measurement of the field balance in the cavity, in this mode, shows slightly lower field strength in the first half-cell, near the cathode. This discrepancy with the design can be caused by the measurement itself (where a different cathode plate was used), or by the position of the antenna. With a lower field in the first cell, the electrons will be accelerated to a slightly lower energy, but still well within the requirements for further experiments. The absorbed power shows the expected behavior. Up to this moment, the cavity was conditioned to 2.7 MW, ~ 25% of the expected maximum power. More conditioning may be needed to increase the power absorbed in the cavity without causing breakdowns. A possible cause for the long conditioning time needed, is that at some point during operation of the cavity, the RF-window cracked. The window separates the vacuum part from the high-pressure SF_6-filled RF-waveguides. This released SF_6 gas and debris into the cavity, while operating at high power. A discoloring of parts of the input coupler and the irises inside the cavity was observed. The cathode plate was re-machined, but the other parts were left untreated. It may be necessary to re-machine these parts as well.

With 2.7 MW absorbed power, the maximum field strength inside the cavity is 50 MV/m, approximately half the maximum field strength in the design. With these fields electron bunches can be accelerated to approximately 3.5 MeV. These bunches will be measured and analyzed in the next chapter and the suitability for LWA will be determined.

References

[1]   J. Faure, C. Rechatin, A. Norlin, A. Lifschitz, Y. Glinec and V. Malka, *Controlled injection and acceleration of electrons in plasma wakefield by colliding laser pulses*, Nature, Vol. 444, p. 737, (2006).

[2]   R. Akre, D. Dowell, P. Emma, J. Frisch, S. Gilevich, G. Hays, Ph. Hering, R. Iverson, C. Limborg-Deprey, H. Loos, A. Miahnahri, J. Schmerge, J. Turner, J. Welch, W. White, and J. Wu, *Commisioning the Linac Coherent Light Source*, Phys. Rev. ST Accel. Beams, Vol. 11, 030703, (2008).

[3]   M. J. van der Wiel, O. J. Luiten, G. J. H. Brussaard, S. B. van der Geer, W. H. Urbanus, W. van Dijk and Th. van Oudheusden, *Laser wakefield acceleration: the injection issue. Overview and latest results,* Phil. Trans. R. Soc. A, Vol. 364, p. 679, (2006).

[4]   A. G. Khachatryan, F. A. van Goor, K.-J. Boller, A. J. W. Reitsma and D. A. Jaroszynski, *Extremely short relativistic-electron-bunch generation in the laser wakefield via novel bunch injection scheme*, Phys. Rev. ST Accel. Beams, Vol. 7, 121301 , (2004).

[5]   A. Irman, M. J. H. Luttikhof, A. G. Khachatryan, F. A. van Goor, J. W. J. Verschuur, H. M. J. Bastiaens, and K.-J. Boller, *Design and simulation of laser wakefield acceleration with external electron bunch injection in front of the laser pulse*, J. Appl. Phys., Vol. 102., 024513, (2007).

[6]   W. H. Urbanus, W. van Dijk, S. B. van der Geer, G. J. H. Brussaard, and M. J. van der Wiel, *Front-to-end simulations of the design of a laser wakefield accelerator with external injection*, J. Appl. Phys., Vol. 99, 114501, (2006).

[7]   W. van Dijk, S. B. van der Geer, M. J. van der Wiel, and G. J. H. Brussaard, *Parameter study of acceleration of externally injected electrons in the linear laser wakefield regime*, Phys. Plasmas, Vol. 15, 093102, (2008).

[8]   M. J. de Loos, S. B. van der Geer, Y. M. Saveliev, V. M. Pavlov, A. J. W. Reitsma, S. M. Wiggins, J. Rodier, T. Garvey, and D. A. Jaroszynski, *Radial bunch compression: Path-length compensation in an rf photoinjector with a curved cathode*, Phys. Rev. ST Accel. Beams , Vol. 9, 084201, (2006).

[9]   F. Kiewiet, *Generation of ultra-short, high brightness relativistic electron bunches*, PhD thesis, Eindhoven University of Technology, ISBN: 90-386-1815-8, (2003).

[10]   W. P. E. M Op 't Root, M. J. de Loos, S. B. van der Geer, A. H. Kemper, E. H. Rietman, M. J. van der Wile and O. J. Luiten, *Second generation TU/e RF-photogun*, submitted op Phys. Rev. ST Accel. Beams, (2010).

[11]   W. van. Dijk, *Simulations and Experiments on External Injection for Laser Wakefield Acceleration*, PhD thesis, Einhoven University of Technology, ISBN: 978-90-386-2316-0, (2010).

[12] D. van der Drift, Electron energy determination of an RF-photogun for laser wakefield acceleration, Eindhoven University of Technology, Bachelor Thesis, CQT 2009-08, (2009.)

[13] S. Humphries Jr., *Charged Particle beams*, John Wiley and Sons, ISBN 0-471-60014-8, (1990).

[14] T. van Oudheusden, *Electron source for sub-relativistic single-shot femtosecond diffraction*, PhD thesis, Einhoven University of Technology, (2010).

[15] L. C. Maier and J. C. Slater, *Determination of Field Strength in a Linear Accelerator Cavity*, J. Appl. Phys., Vol. 23, p. 78, (1952).

[16] Pulsar Physics. www.pulsar.nl/gpt.

Chapter 5

Results from the Beam Line.[1]

5.1 Introduction

This chapter mainly concerns the measurements of electron bunch properties produced by the RF-photogun (Sec 5.5). The properties of the RF-photogun are described in the previous chapter. Besides the 'standard' properties of the electron bunches from the RF-photogun i.e. energy, energy spread, bunch length at focus and transverse emittance, we focused in this chapter on the properties that are specifically important for LWA, namely smallest possible focus spot, focus stability and timing jitter between TW laser pulse and electron bunch at the entrance of the plasma channel. Out of these, bunch length and timing jitter are inferred from GPT simulations, the others are measured directly and the results are presented in this chapter. All measurements were done at 3.71 MeV, which was close to the maximum energy at which the RF-photogun could be operated reliably. For higher energy, further conditioning of the photogun is required. 3.71 MeV is the perfect energy for injection in the nonlinear regime of LWA. The measurements performed will show that the RF-photogun satisfies the conditions for external electron injection for LWA.

Furthermore, in this chapter the influence of the laser pulse - that emits the electrons from the cathode - on the accelerated charge is examined (Sec 5.4). This is done for different wavelengths i.e. 266 nm, 400 nm and 800 nm.

---

[1] Based on: X. F. D. Stragier, O. J. Luiten, S. B. van der Geer, M. J. van der Wiel and G. J. H. Brussaard, "Experimental validation of a radio frequency photogun as external electron injector for a laser wakefield accelerator.", Journal of Applied Physics, 110, 024910 (2011).

An overview the beam line used to measure the bunch properties is found in Sec 5.2. A description and measurements of the magnetic fields used to assure an appropriate electron bunch transport through the beam line are presented in section 5.3.

5.2 Test beam line setup

A beam line has been set up to measure different properties of the electron bunches produced by the RF-photogun, specifically energy, energy-spread, emittance, charge and, particularly of interest to the injection in LWA, smallest focus spot and shot-to-shot stability of the focus spot. A schematic overview of the different components of the beam line can be seen in Fig. 5.1.

The optical part of the setup is a Titanium:Sapphire femtosecond laser system that consists of a Femtosource oscillator and an Omega Pro multi-pass amplifier (Femtolaser Productions GmbH) that produces laser pulses of 30 fs with an energy of 0.8 mJ and a central wavelength of 800 nm. By third harmonic generation (THG-Ω1000 by B.M. Industries) the pulse from the Ti:Sa laser is transformed to a UV- pulse with a central wavelength of 266 nm, a maximum energy of 40 μJ, and a length of ~50 fs. This UV-pulse is reflected by a mirror in a flipper mount (FM) and a mirror (M1) to the center of the cathode of the RF-photogun. The reflection of the UV-pulse from the cathode is directed via mirror M2 and M3 through a lens L1 which makes an image of the cathode on a CCD-camera (all cameras used are Point Grey Flea 2). An interference pattern is seen on the CCD-camera, caused by the coherent UV pulses that reflect off the spiral grooves (with a depth of ~100 nm, caused by the machining) on the cathode plate. This pattern makes the alignment of the laser on the centre of the cathode straightforward (see Fig. 5.2a). To see the real (radial) shape of the UV-pulse on the cathode, the mirror in the flipper mount is moved out of the laser path and the UV-pulse is directed to the 'virtual cathode' CCD (see Fig. 5.1 and 5.2.b). To get the same image on the virtual cathode CCD as on the cathode, the distance from the flipper mount to the virtual cathode CCD is set equal to the distance from the flipper mount to the real cathode. The measured FWHM of the intensity of the UV-pulse on the (virtual) cathode is 1.7 mm.

A possible way to deliver electron bunches with sub-picosecond duration at the entrance of a plasma channel is by first creating and accelerating uniformly filled 3D ellipsoidal electron bunches in the RF photogun [1]. Because the space-charge fields in an ellipsoidal bunch depend linearly on the position inside the bunch, the bunch deforms during acceleration and transportation, but remains an ellipsoid. After acceleration, this ellipsoid bunch can be focused by a solenoid lens that exerts a force on the electrons that also depends linear on the distance from the axis. The bunch can be compressed in the longitudinal direction by an RF-compressor in which the longitudinal force is linear in time. The final bunch length is nearly equal to the bunch length at creation. For this a laser pulse with a spherical profile on the cathode is required in combination with an RF- compressor.
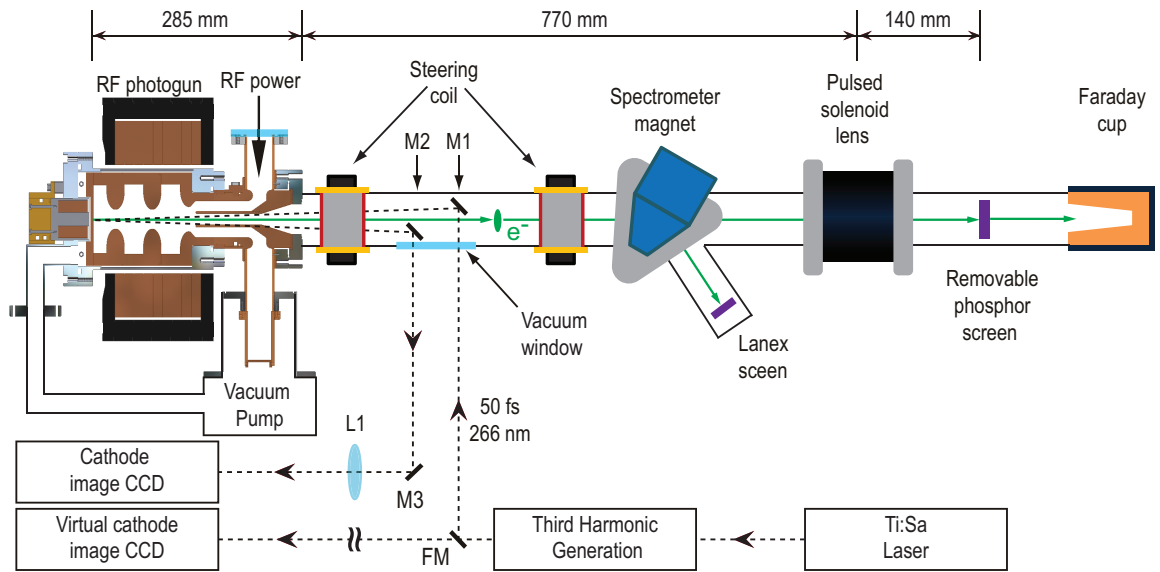
Figure 5.1: Schematic overview of the beam line used to characterize the properties of the electron bunches.
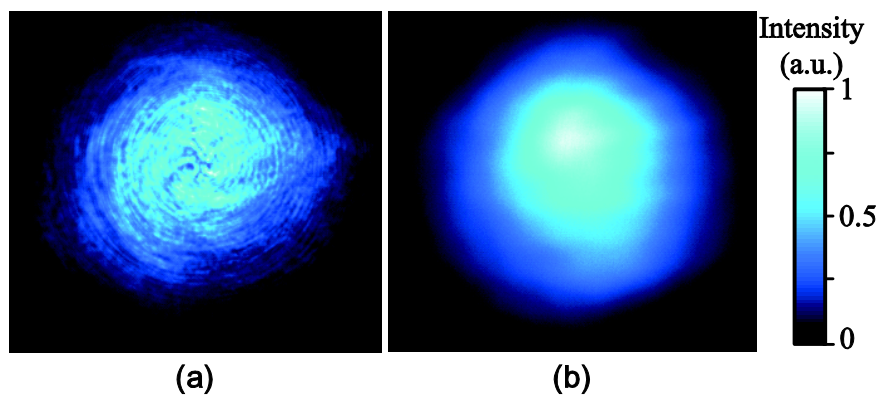

Figure 5.2: Image of the UV-spot on the centre of the cathode. The spiral diffraction pattern caused by the machining of the cathode indicates that the UV-pulse is aligned on the centre of the cathode (a). The profile of the UV-pulse on the cathode as can be seen on the 'virtual cathode' CCD (b). The images shown are 3×3 mm^2

In this setup we opted for a more simple method, using Gaussian laser pulses on the cathode to emit electrons. In this case the RF-compressor is not required, but the electron bunches in the RF-photogun must be accelerated as quickly as possible to relativistic speed, to limit bunch expansion due to space-charge. The acceleration due to space-charge in longitudinal and in radial direction is proportional to $1/\gamma^3$, with the Lorentz factor $\gamma = 1/[1-(v/c)^2]^{1/2}$, where v is the velocity of the electrons and c the speed of light [2]. For this reason it is highly desirable that the electrons from the cathode surface are photo-emitted in a high accelerating field. The electron
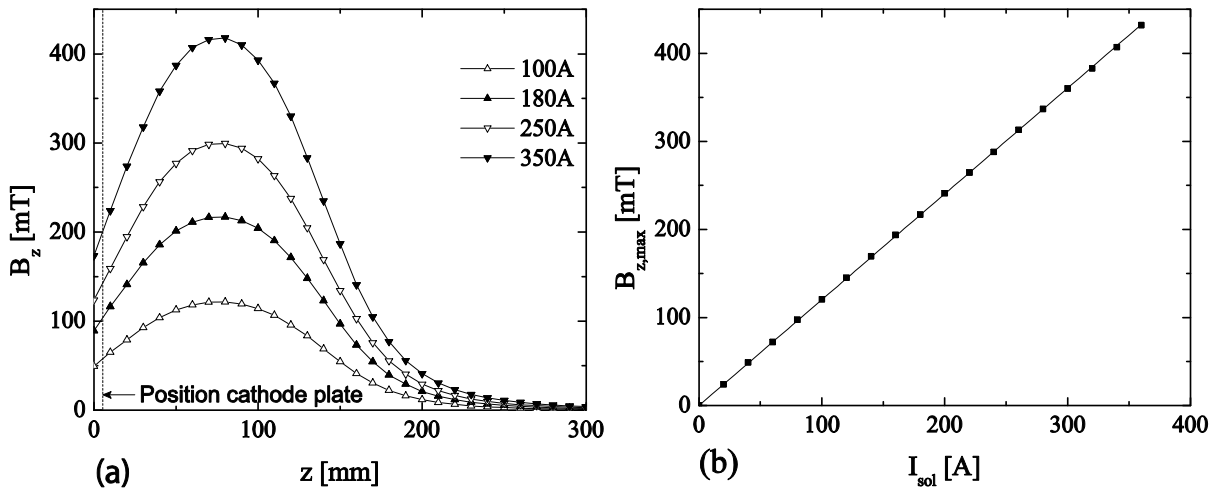
Figure 5.3: (a) On-axis magnetic field in z-direction of the solenoid around the RF-photogun versus z for a solenoid current of 100 A, 180 A, 250 A and 350 A. (no bucking coil mounted) (b) Measured (dots) maximum on-axis magnetic field in the z direction of the solenoid versus solenoid current. Black line is a linear fit on the measurent.

bunch can then be focused downstream to both a small spot, radially, and at the same time keeping it short in the longitudinal direction to ensure a high peak current, which results in higher accelerated charge after LWA. The phase of the RF wave at which the UV-pulse hits the cathode and electrons are created is determined experimentally by maximizing the energy of the accelerated electron bunches at a given power setting of the klystron. In the present experiments this was found to be 72° before the crest of the RF wave to assure a maximum kinetic energy of 3.71 MeV at the exit of the RF-photogun (the klystron was operated at 3.2 MW). A current-controlled spectrometer in combination with a LANEX screen, lenses and CCD camera is used to measure the energy and energy-spread of the electron bunches.

Timing jitter and stability of the output power of the klystron determine the shot-to-shot variations in energy of the electron bunches. The 3 GHz oscillator driving the klystron for the RF system is synchronized to the 75-MHz laser oscillator that produces the UV pulses. The timing jitter between the two oscillators is less than 20 fs [3]. The influence on the energy of the electrons is less than 0.01% at the injection phase used in these experiments (72° before crest). Using estimated power variations of the klystron of 0.1%, the energy jitter is expected to be 0.05% which is a small contribution to the overall energy spread of the electron bunches generated by the photogun (Sec. 5.5.1 and 5.5.6).

A magnetic solenoid lens is placed in the beam line at a distance of 1055 mm from the cathode plate and focuses the electron bunch on a phosphor screen 140 mm further downstream. The distance between the cathode and the magnetic solenoid lens is necessary to be able to accommodate the TW-laser beam which is needed for future LWA experiments. The phosphor screen is placed at the position of the entrance of the plasma channel in LWA experiments (see Fig 1.4). The phosphor screen can be moved out of the beam line in order to measure the charge

of the bunch in a Faraday cup. The magnetic lens is a pulsed solenoid, with a peak current of 272 A, resulting in a maximum on-axis magnetic field of 0.68 T. By using a pulsed solenoid, no additional cooling of the solenoid is required and a relatively compact design is possible. The centre of the solenoid can be placed as close as 140 mm from the phosphor screen, limited also by other geometric constraints, such as flanges and the wall of the vacuum chamber. The solenoid can operate at a repetition rate of 2 Hz at maximum current. In the present experiments, where maximum magnetic field was not required, a repetition rate of 5 Hz was achievable without overheating the solenoid or current supplies.

Finally, the path of the electron bunches can be slightly corrected by 2 steering coils to ensure a good alignment between the electron bunches and the spectrometer or between the electron bunches and the pulsed solenoid.

5.3 Magnetic compensation fields

5.3.1 Photogun magnetic fields

The RF-photogun is positioned inside a magnetic solenoid lens. A bucking coil is installed outside the vacuum at the other side of the cathode to generate a zero magnetic field on the cathode. The position of the solenoid and bucking coil can be seen in Fig. 4.1 and 5.1. The purpose of the solenoid and bucking coil is described in section 4.2.

5.3.1.1 RF-photogun solenoid

The magnetic solenoid lens has an inner diameter of 130 mm, an outer diameter of 230 mm and a length of 120mm. It consists of 144 turns of copper wire. The high continuous current could overheat the solenoid. To prevent this, cooling water flows through the hollow copper wire. The complete solenoid can be pitched, yawed and displaced in x-, y-, and z- direction, to make an alignment with the RF-photogun and electron bunches possible.

The measurement of the on-axis magnetic field in the z-direction B_z versus z is shown in figure 5.3.a. These measurements were done for solenoid currents of 100 A, 180 A, 250 A and 350 A. The simulated values of B_z are in good agreement with the measurements which are only 2 % higher than the simulated values. The position of the cathode is represented in Fig 5.3a by the dotted line. All measurement of the magnetic fields described in this chapter are done with a Hirst gaussmeter type GM04.

The measurement of maximum B_z along the z-axis versus solenoid current is given in Fig. 5.3.b. Maximum B_z along the z-axis is positioned at 71 mm from the cathode. The solid line represents a linear fit on the measurements. From these measurements it can be seen that the solenoid does not go into saturation even at currents up to 360 A.

5.3.1.2 Bucking coil

The solenoid around the RF-photogun generates a non-zero magnetic field on the cathode surface. Electrons that are photoemitted by the laser pulse on the cathode instantaneously start rotating around the magnetic field lines. This has a negative influence on the emittance of the electron bunch which needs to be as low as possible.

The normalized emittance in x-direction in configuration space is defined as [4]:

$$\varepsilon_{x,n} = \gamma\beta\sigma_x\sigma_{x'}, \tag{5.1}$$

With $\gamma = (1-v^2/c^2)^{-1/2}$ the Lorentz factor and $\beta = v/c$. σ_x is the RMS radius of the electron bunch in the x-direction. x' is defined as the angle between the projection of the velocity vector of an electron on the x-z plane and the z-axis (z is the average propagation direction of the electron bunch). $\sigma_{x'}$ is the RMS spread of x'. For relativistic paraxial electron bunches traveling in the z-direction $x' \approx v_x/v$ with v_x the velocity component in the x- direction and v the velocity of the electron bunch.

The (normalized) emittance is a direct measure of how small the electron bunch can be focused. For LWA with external injection the electron bunches need to be focused on a spot size comparable to the laser radius that drives the plasma wave which is typically on the order of 40 μm. For this, electron bunches with an emittance lower than ~2 μm are required (see section 5.5.3 and 5.5.6). It is therefore of great importance to keep the normalized emittance as low as possible. The normalized emittance growth due to photoemission of electrons in a non-zero magnetic field on the cathode is given by [5]:

$$\Delta\varepsilon_{x,n} \approx \frac{1}{8}\frac{q|B_{z,cat}|}{2m_ec}\sigma_x^2, \tag{5.2}$$

with electron charge q, m_e the electron mass at rest and $B_{z,cat}$ the magnetic field in z-direction on the cathode. For a solenoid current of 180 A, the B_z field on the cathode generated by the solenoid is $\approx$ 100 mT. This gives an additional normalized emittance growth of $\approx$ 2 μm for a bunch with a radius of 1 mm with a uniform electron distribution.

A bucking coil is used to compensate the magnetic field on the cathode. The bucking coil is a solenoid made of 1 mm diameter copper wire and 480 turns. The spacing between the copper wires is filled with epoxy rencast, CW 5156-1, to enhance heat conduction. The solenoid is wound around a core made out of steel (type 37-2). The diameter of the core is 16 mm and the length of the solenoid is 40 mm. The solenoid is surrounded by a steel jacket of 3 mm thickness. The bucking coil is water cooled on one side of the coil and placed outside the vacuum (Fig. 4.1).

The measured on-axis magnetic field in the z-direction of the bucking coil can be seen in Fig. 5.4.a for currents of 2 A, 4 A and 6 A. The magnetic field drops fast to zero and therefore, the bucking coil has to be placed as close as possible to the cathode (Fig. 4.1). The cathode position is marked as the dotted line in Fig. 5.4.a. The on-axis magnetic field in the z-direction
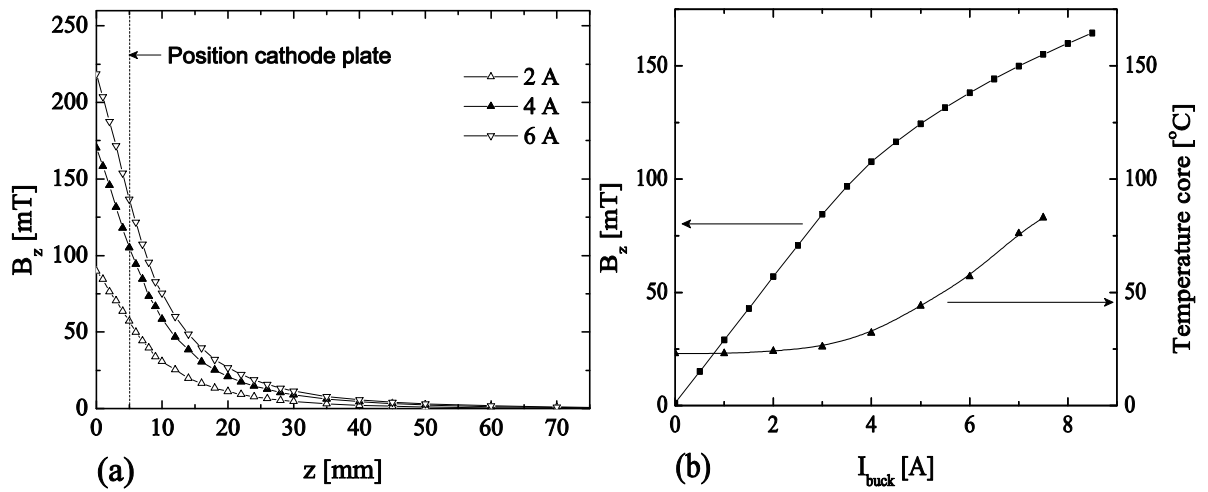
Figure 5.4: (a) On-axis magnetic field of the bucking coil in the z-direction versus distance for 2 A, 4 A and 6 A. (b) On-axis magnetic field in the z-direction on the cathode generated by the bucking coil and temperature of the core as function of the bucking coil current.
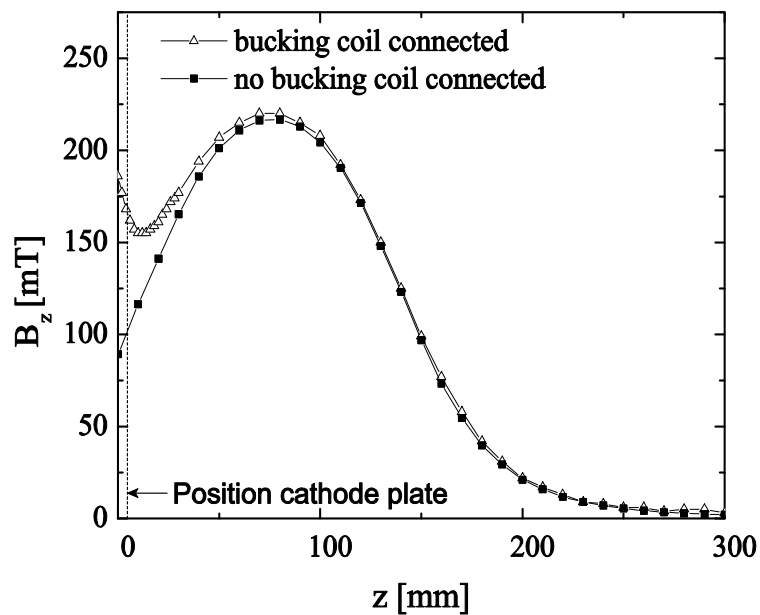

Figure 5.5: Effect of the bucking coil core on the on-axis magnetic field in the z-direction of the solenoid for a solenoid current of 180 A (no bucking coil current). Without bucking coil: black dots, with mounted bucking coil: triangles.

on the cathode versus bucking coil current can be seen in Fig. 5.4.b. There is a linear relation between magnetic field and current for currents up to 4 A. For currents over 4 A the magnetic field becomes lower than one would expect. This variation cannot be explained by saturation of the steel core, as the steel starts saturating for magnetic field around 1 T. The bucking coil is
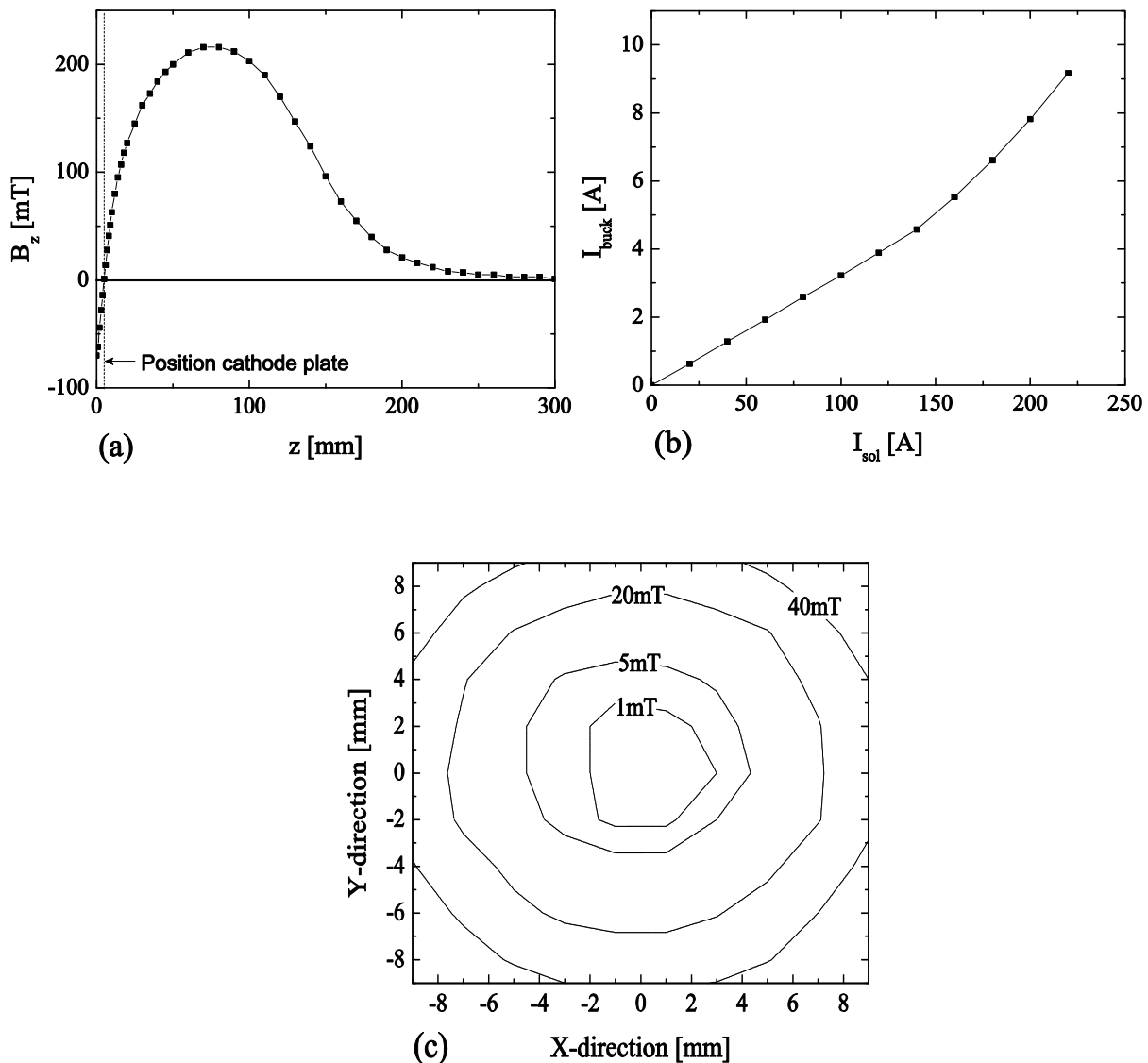
Figure 5.6: Measurements with $B_z = 0$ at the centre of the cathode. (a) $B_z(r=0,z)$ (b) Bucking coil current versus solenoid current and (c) B_z on the cathode as function of position in the xy-plane for a solenoid current of 180 A and a bucking coil current of 6.6 A.

cooled at one side and not at the place closest to the cathode. Therefore the temperature of this side rises at higher current because of resistive heating. This can be seen in Fig. 5.4.b. The nonlinearity can be explained by the fact that at higher temperature the permeability of the steel core drops and thus also the magnetic field.

Mounting the bucking coil to the back of the RF-photogun has an influence on the magnetic field generated by the solenoid around the RF-photogun, even when there is no bucking coil current. The high permeability of the steel core of the bucking coil locally increases the magnetic field generated by the solenoid. This effect on the on-axis magnetic field in the z-direction for a solenoid current of 180 A can be seen in Fig 5.5. The magnetic field at the

cathode rises from ~100 mT to ~170 mT when mounting the bucking coil, without current through the bucking coil. This field enhancement will be smaller when a current is applied through the bucking coil, but will not be negligible. Therefore, the magnetic field needs to be measured for every solenoid current while varying the bucking coil current to find the combination at which the magnetic field at the position of the cathode is zero.

5.3.1.3 Solenoid-bucking coil combination

During operation of the RF-photogun, the current through the solenoid needs to be adjusted in such a way that the solenoid has the appropriate current for optimal electron bunch transport through the beam line. The magnetic field at the centre on the cathode is measured and the bucking coil current is adjusted so that the magnetic field is zero for a certain solenoid current. The on-axis magnetic field in the z-direction as function of the z-position is given in Fig. 5.6.a. A solenoid current of 180 A has to be compensated with a bucking coil current of 6.6 A to achieve a zero magnetic field on the cathode. The place of the cathode is given by the dotted line. Inside the cathode, the magnetic field becomes negative. The high magnetic field gradient close to the cathode requires precise bucking coil setting. The relation between bucking coil and solenoid current to achieve a zero magnetic field at the centre of the cathode for the operating range of the solenoid is shown in Fig. 5.6.b. The temperature effect on the bucking coil as described in section 5.3.1.2 is also visible here.

The measured magnetic field in the z-direction on the cathode as function of x- and y-position can be seen in Fig. 5.6.c. A typical laser spot on the cathode has a full width at half maximum of ~2 mm. Assuming the laser to be aligned on the centre of the cathode (Fig. 5.2.a), the electrons are created in a magnetic field lower than 1 mT. This adds 0.02 μm to the normalized emittance (Eq. (5.2)).

5.3.2 Pulsed focussing solenoid

The electron bunches coming from the RF-photogun need to be focused at the entrance of the plasma channel on a spot as small as possible. This is commonly done by the use of a quadrupole triplet. Here we used a solenoid because it can be placed closer to the plasma channel [6].

The solenoid is operated using a pulsed current, so that no additional cooling is required and the solenoid can be kept small. The solenoid was built in-house and has an inner diameter of 50 mm, an outer diameter of 160 mm and a length of 110 mm. These relatively small dimensions make it possible to make the distance between the centre of the solenoid and the plasma channel as small as 140 mm. To eliminate induced currents in the beam pipe which could reduce and even null the magnetic field inside the beam line, the stainless steel beam pipe within the solenoid is replaced by a glass tube. The maximum repetition frequency at which the
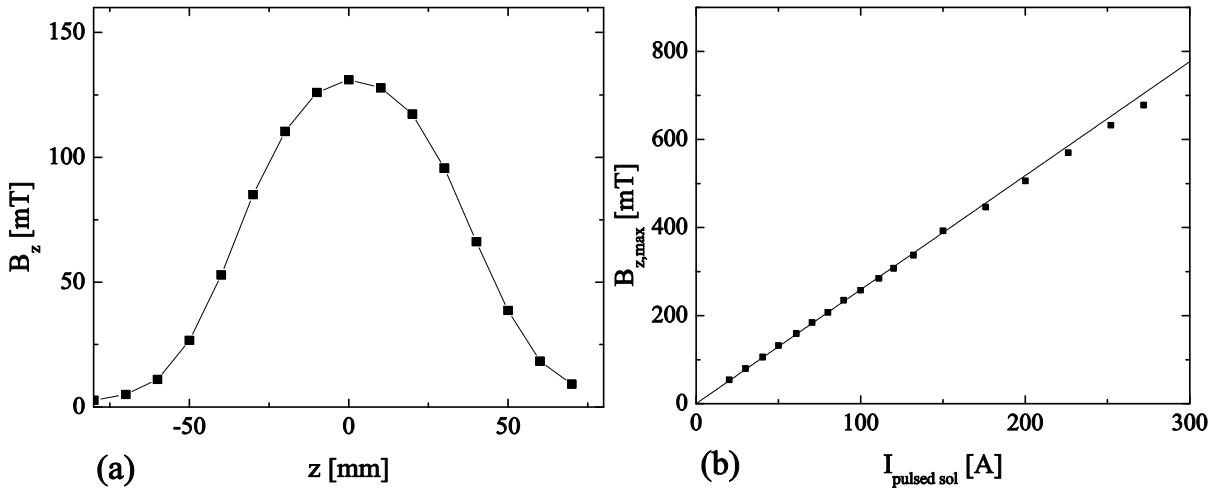
Figure 5.7: Magnetic field measurenents of the pulsed focusing solenoid (a) On-axis magnetic field in the z-direction versus z-position (z = 0 is the centre of the solenoid). (b) Maximum on-axis magnetic field in the z-direction (at z = 0) versus current.

solenoid can be operated is determined by the current supplies and is 2 Hz at maximum current (272 A, producing a field of 0.68 T). During the measurements that are presented in section 5.5, the maximum current required was 159 A with an associated magnetic field of 0.405T and an operating frequency of 5 Hz is possible.

The focal distance of a magnetic solenoid lens is given by [7]:

$$f_{sol} = \frac{4}{\int [qB_z(z)/\gamma m_e v_z]^2 dz},$$ (5.3)

with $B_z(z)$ the on-axis magnetic field in the z-direction as function of z. $v_z \approx \beta c$ is the velocity component of the electrons in the z-direction. In figure 5.7.a measurements are shown of the magnetic field in the z-direction, B_z, versus z-position for a solenoid current of 50 A, giving a maximum magnetic field of 0.13 T. The centre of the solenoid is positioned at z = 0. In figure 5.7.b the maximum B_z field as a function of the solenoid current is presented. The dots represent the measurements and the solid line is a linear fit. There is a linear relation between current and magnetic field at low current. Saturation of the yoke starts around 200 A, but the solenoid can be easily operated with currents up to 300 A. Even at these high currents, the difference between the linear fit and the measurement is less than 5 %

The measured solenoid current versus time with the corresponding maximum B_z (at z = 0) is given in figure 5.8.a. As expected, the magnetic field and current versus time show similar behavior, but are not completely proportional due to magnetic saturation and hysteresis in the ferrite yoke around the solenoid. The graph can be divided in four different intervals. A simplified electric scheme of the (in-house built) current supply is given in Fig. 5.8.b. The electric scheme and appropriate current is given for the four different intervals. The basic
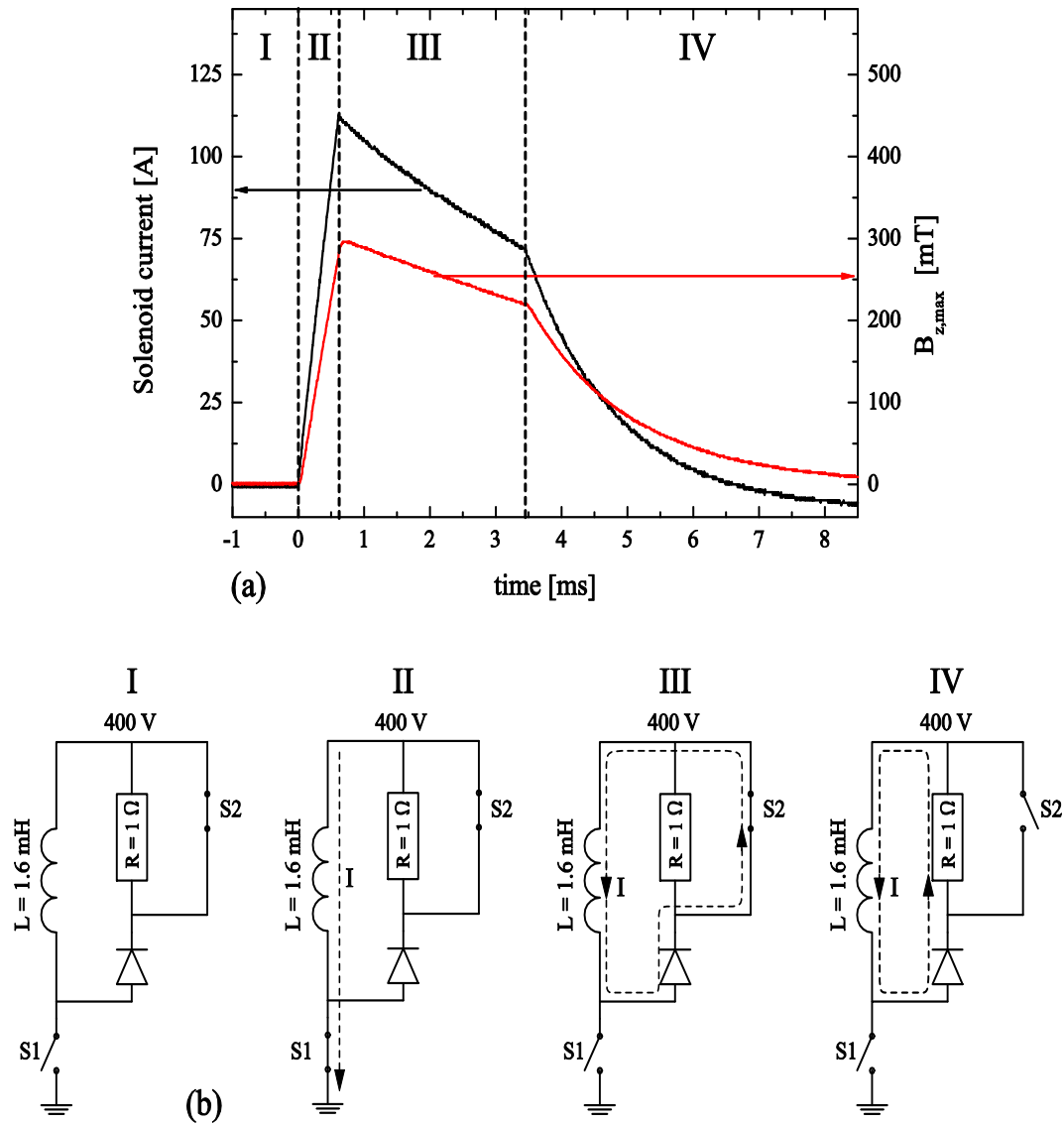
Figure 5.8: (a) Four different intervals of the solenoid current pulse and B_z (at z= 0) versus time. (b) Electric scheme and current for the four differetent intervals.

electric scheme consists of two switches S1 and S2, a diode, a $R = 1\ \Omega$ resistor and the magnetic solenoid lens indicated as L. The solenoid has and inductance L of 1.6 mH and an internal resistance R_{in} of 0.15 Ω. One side of the solenoid is kept at a DC voltage U of 400V.

The current pulse is explained as follows:

- **Interval I**: Switch S1 is open and switch S2 is closed. No current flows through the solenoid.
- **Interval II**: The system receives a trigger pulse and switch S1 closes, a current flows through the solenoid and the diode prevents a current flow over S2 and R. The current, I, rises linear and can be approximated by: $I = Ut/L$, where t is time.

- **Interval III**: Switch S1 is opened and the magnetic field in the solenoid keeps the current flowing and circles over switch S2 that bypasses *R*. The current exponentially drops with a time constant of 10 ms given by L/R_{in}.
- **Interval IV**: Switch S2 is opened and current flows through *R*. The current drops with a time constant of 1.6 ms given by *L/R*. Most of the energy is dissipated in resistor *R* and not in the solenoid. This is essential to prevent the solenoid from overheating.

The maximum current c.q. magnetic field between II and III is determined by the adjustable length of interval II. The solenoid was originally designed to be used in interval III because of the low gradient in this interval. In practice it turns out that operating in interval II is easier. This is done by generating a higher magnetic field between II and III than necessary to focus the electron bunch. By adjusting the delay between the trigger pulse (to start interval II) and laser pulse at the cathode of the RF-photogun, the electron bunch passes the magnetic solenoid lens at the desired focal length (in interval II). Using this method to focus the electron bunches is justified as the high relativistic electron bunches passes the magnetic field of the solenoid in less than 1 ns. During this transition time, the magnetic field can be considered constant.

5.4 Charge measurements

In this section, the measurements are described and analyzed of the amount of charge accelerated in the RF photogun. The electrons are created through photoemission by a laser pulse on the copper cathode and accelerated in the RF-photogun. The accelerated charge depends on the material properties of the cathode and the laser pulse. The most important property of the cathode in this respect is the work function of the material the cathode is made of. The work function of a material is defined as the minimal energy needed to extract an electron from that material. The work function W_{cu} for copper is 4.66 eV. The charge measurement experiments described in this section are done with a maximum on axis electric field of 55 MV/m. This corresponds to an electric field of 17 MV/m on the cathode as the laser pulse hits the cathode at a phase of 72º before the crest of the RF field. The electric field on the cathode lowers the work function due to the Schottky effect according to [7]:

$$\Phi_s = \sqrt{\frac{e^3 E}{4\pi\varepsilon_0}},$$ (5.4)

with *e* the elementary charge and *E* the electric field on the cathode. An electric field of 17 MV/m on the cathode results in a work function lowered by 0.16 eV. This gives a effective work function for our copper cathode of 4.5 eV.

The laser system used generates 800 nm pulses that can be transformed to 400 nm pulses by second harmonic generation and 266 nm pulses by third harmonic generation. The second/third harmonic generation system used transforms a 800 nm laser pulse with an energy
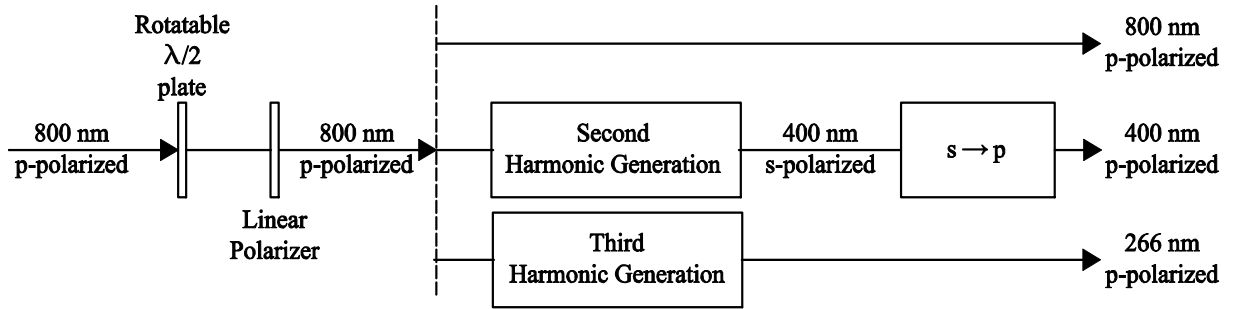
Figure 5.9: System to gradualy change the energy of the required laser pulse on the cathode, whitout changing the polarization and the laser pulse profile.

of 800 μJ to a laser pulse of 400 nm with a typical energy of 250 μJ or a 266 nm laser pulse with an energy of 50 μJ. The photon energy of a 266 nm, 400 nm and 800 nm photon are respectively 4.67 eV, 3.11 eV and 1.55 eV. The energy of the 266 nm-pulse photons is above the effective work function (due to Schottky effect) of copper and one photon can emit an electron from the cathode. To extract electrons from the cathode with a 400 nm pulse, a two-photon interaction is needed and for 800 nm a three-photon interaction is required. Although a two- or three-photon process is, in general, less efficient than a single-photon process, it would be beneficial for future experiments if electrons can be generated using 400 nm or even 800 nm laser pulses, as this would simplify the laser setup. Therefore the effect of 266 nm, 400 nm and 800 nm laser pulses on the electron bunches have been examined. Because the duration of the laser pulses is short, ~50 fs, the peak power is high (5 GW at 400 nm and 16 GW at 800 nm, respectively), so that also two- and three-photon interactions may produce sufficient charge.

The accelerated charge is collected in the faraday cup (Fig. 5.1) that is connected to a load with resistance R. The voltage is measured using an oscilloscope and integrated digitally to determine the charge, as given by:

$$Q = \frac{1}{R} \int U(t) dt, \tag{5.5}$$

where $U(t)$ is the voltage over the load R.

All measurements (266 nm, 400 nm and 800 nm) are done with p-polarized laser pulses on the cathode (at the near-zero angle of incidence used in these experiments, there is little difference between s-and p-polarization). To change the energy of the laser pulse on the cathode gradually and leave the polarization and profile of the laser unchanged, the laser polarization is rotated using a half-wave plate followed by a linear polarizer that transmits only the p-polarized part of the laser pulse (Fig. 5.9). For the experiments with 800 nm laser pulses, the pulses are sent directly to the cathode after the linear polarizer. If a 400 nm pulse is required, the fundamental 800 nm laser pulse after the linear polarizer is transformed using second harmonic generation in a barium borate (BBO) crystal. This process produces 400 nm at s-polarization [8]. By using a periscope consisting of 2 mirrors that are rotated 90° around the

___

central axis of the mirrors, the polarization is rotated to p-polarization. If 266 nm laser pulses are required the (s-polarized) 400 nm pulses are combined with 800 nm pulses (whose polarization has also been rotated to s-polarization) in a second BBO crystal to produce the third harmonic at 266 nm. These 266 nm pulses are produced at p-polarization.

5.4.1 Charge versus laser pulse energy at 266 nm

The accelerated charge is measured as a function of the laser pulse energy for three different sizes of the laser pulse on the cathode (Fig. 5.10). The $1/e^2$ radius of the laser spot on the cathode is 3.6 mm (blue), 1.5 mm (green) and 0.6 mm (red). During the measurements, the energy of the laser pulse is measured before entering the vacuum. In calibration measurements, an energy loss of the laser pulse of 28% in the fused silica vacuum window and mirror M1 (Fig. 5.1) was measured. This is taken into account to determine the laser pulse energy on the cathode during charge measurements.

In the measurement with the largest laser spot size of 3.6 mm (blue) the charge initially increases linearly with laser energy. The initial slope in figure 5.10 is first order as was expected, since the photon energy is larger than the work function and a one-photon interaction is expected. However, if the size of the laser spot on the cathode is decreased at a given energy, the collected charge increases considerably. The charge measurements with the small laser spot size of 0.6 mm (red) show a nearly quadratic dependence on the energy of the laser pulse. This is more consistent with a two-photon process. This effect can be understood if it is assumed that even at photon energies above the work function, two-, or more, photon processes are able to extract electrons from levels further below the work function. The accelerated charge by the RF-photogun is then a summation of charges Q_k, with Q_k the charge generated by a k-photon interaction on the cathode (k = 1,2,3,…). Assuming a Gaussian laser profile in transverse and longitudinal direction hitting the cathode, the total accelerated charge Q is given by:

$$Q = \sum_{k=1}^{+\infty} Q_k = e \sum_{k=1}^{+\infty} \alpha_k \left(\frac{E_{pulse}}{E_\lambda} \right)^k \frac{1}{t_0^{(k-1)} w^{2(k-1)}} \, , \tag{5.6}$$

with e the elementary charge, E_{pulse} the total energy of the laser pulse, E_λ the energy of one photon at the used wavelength, t_0 is the length (FWHM) of the laser pulse in and w denotes the radius ($1/e^2$ intensity) of the laser on the cathode. The parameter α_k is a constant which depends on factors such as the cathode material used, the contamination of the cathode, the wavelength and polarization of the laser pulse, the angle of incidence of the laser pulse on the cathode, etc.. Because the slope of the measurements in Figure 5.10 is always below 2, three-photon interactions are not observed and therefore for the energy range used and 266 nm pulses, Eq. (5.6) can be simplified to:

$$Q = e\alpha_1 \frac{E_{pulse}}{E_\lambda} + e\alpha_2 \left(\frac{E_{pulse}}{E_\lambda} \right)^2 \frac{1}{t_0 w^2} \tag{5.7}$$
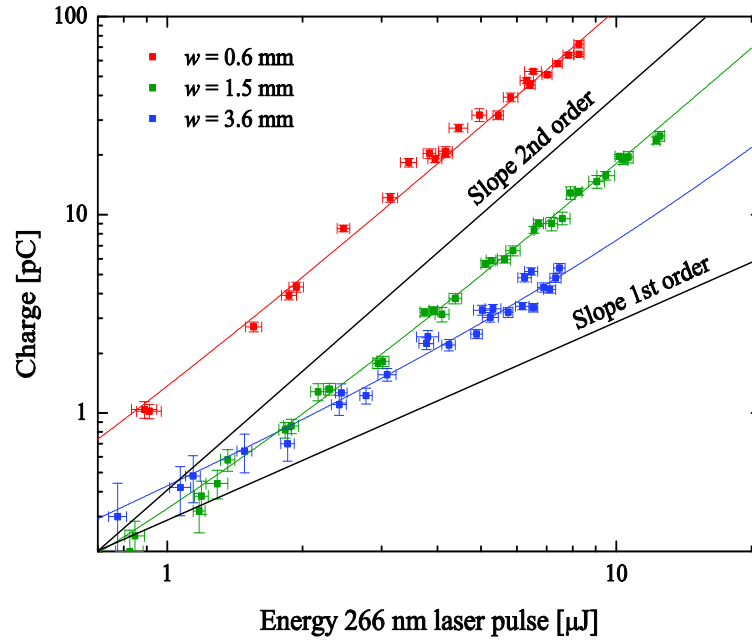
Figure 5.10: Accelerated charge versus laser pulse energy for 266 nm pulses for a laser with a radius ($1/e^2$ intensity) of 0.6 mm (red), 1.5 mm (green) and 3.6 mm (blue). Measurements (dots) and fit with Eq. (5.7). Lines with slopes corresponding to a linear dependence and quadratic dependence are shown for comparison.

This formula is fitted with $E_\lambda = 4.66$ eV on the data points in Fig. 5.10 for the three different measurements. α_1 in Eq. (5.6) and Eq. (5.7) is generally known as the quantum efficiency. Therefore α_2 can be seen as a second- order quantum efficiency. The quantum efficiency α_1 is defined as the probability that one photon extracts an electron from the cathode and is given by: $EQE = \alpha_1 = n_e/n_{ph}$, with n_e the number of photoemitted electrons (Q/e) when using n_{ph} photons (E_{pulse}/E_{laser}).

The fit parameter α_1 is determined by using the measurements of the laser spot with a 3.6 mm radius ($1/e^2$ intensity) as this measurement is dominated by one-photon interaction. This gives a quantum efficiency of $EQE = \alpha_1 = (2 \pm 0.2) \times 10^{-6}$. This is almost a factor 10 smaller than measured in other photoguns [9-11]. The value of the work function depends on the purity of the copper used and the roughness of the surface. Because the cathode is machined using single-point diamond turning, the microscopic roughness of the surface will be very low, of the order of tens of nm, smoother than mechanically polished surfaces, which typically have a smoothness of the order 50 nm. Such a smooth surface can show an increase of the effective work function by a few tenths eV [12], which could be a reason for the low measured value of α_1. This explanation has not been investigated independently for this cathode. Another explanation for the low quantum efficiency may be contamination of the cathode surface. The measurements in Fig. 5.10 have been done with a re-machined cathode surface which may be contaminated during this process. Insufficient cleaning may thus also explain the lower

measured quantum efficiency. The quantum efficiency measured in Ref [10] and [11] (which used the same type of copper and machining that was used in the present experiments) are based on a single measurement of charge versus laser energy. In these references, the radius and the energy of the laser pulse are not mentioned. Therefore, second order effects, if present, may have gone unnoticed. When using a single measurement and a small laser spot at high laser power, an overestimation of the quantum efficiency is made.

The value of α_2 can only be determined if the length of the laser pulse, t_0, is known. This will be done in the next paragraph. For the lines in Figure 5.10, α_2/t_0 (of Eq. (5.7)) was used as the fitting parameter. The value for this parameters is determined from the measurements with a spot of 0.6 mm radius, while keeping the value for α_1 fixed to the value $(2 \pm 0.2) \times 10^{-6}$ found above. All three solid lines in figure 5.10 are drawn using a single set of parameters α_1 and α_2/t_0.

According to (Eq. (5.7)), the photoemitted charge is dependent on the length of the laser pulse t_0. Stretching the laser pulse should result in lower accelerated charge. When an unchirped laser pulse with initial length $t_{0,i}$ propagates through a transparent medium, the laser pulse stretches to a length $t_{0,e}$ with:

$$\frac{t_{0,e}}{t_{0,i}} = \sqrt{1 + \frac{\left(\frac{d^2\varphi}{d\omega^2}\right)^2}{t_{0,i}^4}}.$$ (5.8)

Here $d^2\varphi/d\omega^2$ is the group velocity dispersion of the medium the laser pulse has propagated through [10, 13]. To investigate the effect of pulse stretching on the extracted charge, a measurement series was done with an extra fused silica window of 2 cm thickness in the laser path. A charge measurement as function of the energy for a laser radius ($1/e^2$ intensity) of 0.6 mm on the cathode can be seen in figure 5.11. The red measurements in figure 5.10 and 5.11 are identical. The blue data points are the measurements under the same conditions as the red, but with the extra 2 cm fused silica window in the laser path. The window was placed between the flipper mount and mirror 1, outside the vacuum (Fig. 5.1). Fused silica is used because it is transparent for 266 nm laser pulse. The laser pulse energy is measured after propagation through the fused silica to take reflections on the fused silica window surfaces into account. It can be seen in Figure 5.11, that the collected charge is lower with the extra window in place (blue) compared to the case without the extra fused silica (red). The ratio of the laser pulse lengths after and before the fused silica can now be determined from the fit parameters of Eq. (5.7) on the measurements in figure 5.11. The ratio $t_{0,e}/t_{0,i}$ is found to be 1.76. The length of the initial 266 nm laser pulse before the fused silica can be calculated using Eq. (5.8) and the group velocity dispersion in fused silica at 266 nm [10]:

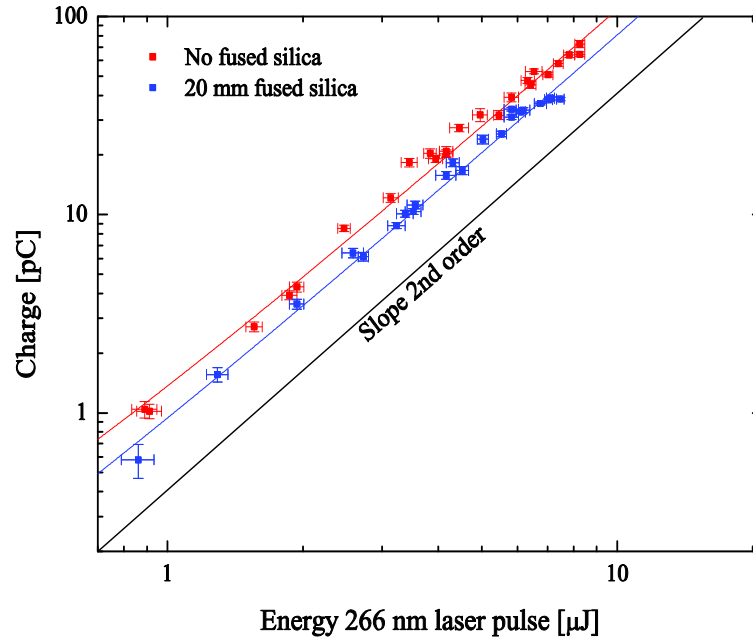$$\frac{1}{L}\frac{d^2\varphi}{d\omega^2} = 2.2 \times 10^3 \text{ fs}^2/\text{cm},$$ (5.9)

Figure 5.11: Accelerated charge versus laser pulse energy for 266 nm pulses with a laser radius ($1/e^2$ intensity) of 0.6 mm on the catode. With 2 cm fused silica in the laser path (blue) and without fused silica (red).

with L the propagation distance in cm of the UV-pulse in the fused silica (2 cm). The initial length (FWHM) of the 266 nm laser pulse is found to be ~ 55 ± 15 fs.

α_2 can be determined with the knowledge of t_o and the fit parameters of the fit of Eq. (5.7) on the red measurements in figure 5.10. The red measurements are used because they are dominated by a two-photon interaction. We find that $\alpha_{2,266nm} \approx 74 \times 10^{-18}$ fs mm^2 for 266 nm linearly (p-)polarized laser pulses on the cathode of the RF-photogun.

5.4.2 Charge versus laser pulse energy at 400 nm

The effect of the laser energy of a 400-nm pulse is examined for a laser radius ($1/e^2$ intensity) of 2.0 mm on the cathode and can be seen in figure 5.12. The measurements show a quadratic dependence of the charge on energy. The electron extraction is purely due to two-photon interactions, as expected. The laser pulse energy is apparently too low to notice any three-photon interactions. The measurement can now be approximated by just the second term in Eq. (5.7):

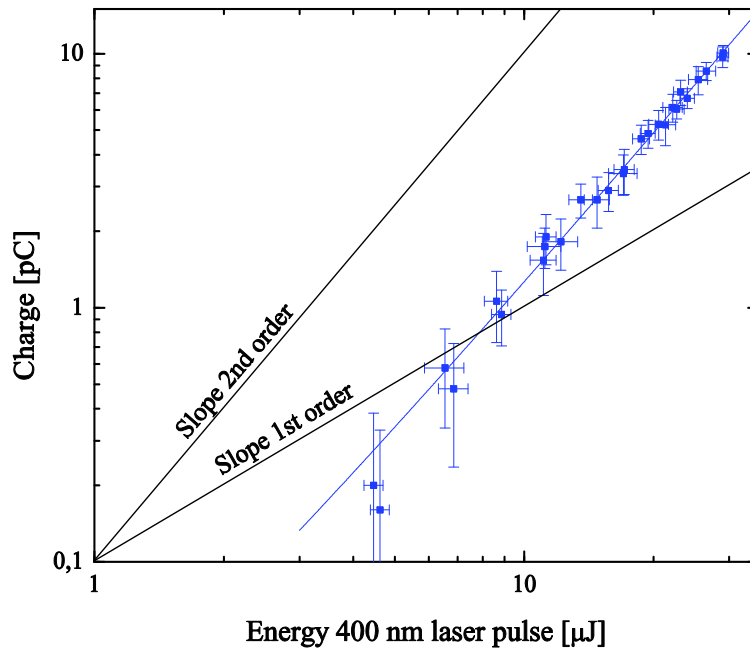$$Q = e\alpha_2 \left(\frac{E_{pulse}}{E_\lambda} \right)^2 \frac{1}{t_0 w^2} \tag{5.10}$$

Figure 5.12: Accelerated charge versus laser pulse energy for 400 nm pulses with a laser radius ($1/e^2$ intensity) of 2.0 mm on the catode. Lines with slopes corresponding to a linear dependence and quadratic dependence are shown for comparison.

The laser pulse length t_0 is not measured directly, but estimated to be ~55 fs as the fundamental 800 nm pulse is 50 fs and we found a similar duration for the pulse at the third harmonic (266 nm) of ~55 fs. Equation (5.10) is fitted with $E_\lambda = 3.11$ eV on the data points in Fig. 5.12. For 400 nm p-polarized laser pulses on the cathode of the RF-photogun we find that $\alpha_{2,400nm} \approx 4.2 \times 10^{-18}$ fs mm^2.

5.4.3 Charge versus laser pulse energy at 800 nm

The experiments of section 5.4.2 have been repeated for 800 nm laser pulses on the cathode. Three photons are needed to extract electrons from the cathode. The collected accelerated charges are under 0.2 pC at full laser power (0.8 mJ), with a comparable $1/e^2$ radius of 1.5 mm as in section 5.4.1. Charge has been detected, but the signal-to-noise was insufficient to state useful results. Higher laser power at 800nm is needed to perform reliable experiments.

5.5 Electron bunch measurements

All measurements presented in this section have been done on electron bunches with a kinetic energy $E_{kin} = 3.71$ MeV ($\gamma = 8.25$). Sections 5.5.1 – 5.5.5 describe measurements of different parameters of electron bunches, all with a charge of 10 pC. Section 5.5.6 deals with the effect of the charge on those measured parameters.
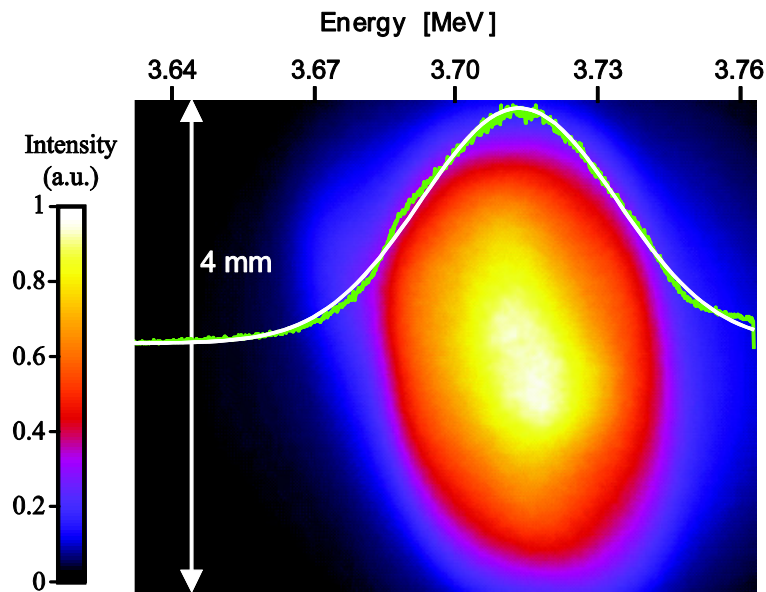
Figure 5.13: Typical picture of the profile on a LANEX screen behind the spectrometer for a single electron bunch of 10 pC. The green line is the energy profile through the point of highest intensity. The white line is a Gaussian fit on the energy profile.

Using a 266 nm or 400 nm laser pulse to extract the electrons from the cathode has no measurable effect on the electron bunch properties as measured and described in this section. Therefore all measurements presented here are done for 266 nm laser pulses.

5.5.1 Energy and energy spread

The kinetic energy of the electron bunches has been measured with a current controlled spectrometer in combination with a LANEX screen (as described in section 5.2). A typical spectrum of a single electron bunch with 10 pC of charge on the LANEX screen can be seen in Fig. 5.13. The green line in the figure is the profile of the measurement at highest intensity and the white line is a Gaussian fit. The (central) energy of the electron bunch is 3.71 MeV with a RMS spread of $\sigma_E = 0.02$ MeV or 0.5% and in agreement with simulations.

Simulations show that the main contribution to the energy spread is caused by the space charge of the electron bunch. The other effects, the energy spread caused by electrons that are accelerated off-axis in a lower accelerating field due to the radial dimensions of the UV-pulse on the cathode and the energy spread caused by the different accelerating field on which the electrons are injected due to the length of the UV-pulse, are negligible compared to the energy spread caused by the space charge of the electron bunch.

Besides the energy spread, there is also a shot-to-shot variation of the measured average electron energy. For 10 consecutive shots, the RMS spread of the average electron energy is measured to be 2 keV or 0.05 %. This is only a small contribution to the overall energy spread.

5.5.2 Timing jitter

The energy spread (as discussed in the previous section) of the electron bunch results in a spread in velocity and directly leads to bunch lengthening as the electrons propagate through the beam line. This is the main reason to keep the distance between the cathode and the entrance to the plasma channel as short as possible. The propagation time of a particle with a Lorentz factor γ over a distance l is given by:

$$t = \frac{l}{c\sqrt{1-1/\gamma^2}} \qquad (5.11)$$

while $t + \Delta t$ is the propagation time for a particle with Lorentz factor $\gamma + \Delta\gamma$ and

$$\Delta t = -\frac{l}{c}\frac{\Delta\gamma}{\sqrt{(\gamma^2-1)^3}} \qquad (5.12)$$

Using this Eq. (5.12) on an electron bunch with a Gaussian energy distribution around 3.71 MeV ($\gamma = 8.25$) and a RMS spread of 0.5 %, results in an extra (RMS) bunch length of $\sigma_{t,E} = 250$ fs per meter propagation distance. This extra bunch length is due to energy spread of the electron bunch and does not take path length difference of the electrons during propagation and the increasing space charge force during focusing into account. The overall (simulated) bunch length at the focus is described in section 5.5.5.

The UV-pulse on the cathode and the TW laser pulse to the plasma channel are both generated from the same pulse from the laser oscillator. The timing jitter between the electron bunches at the exit of the photogun and the TW laser pulses that will be used for LWA is mainly caused by phase jitter in the synchronization between the laser pulses and the 3 GHz RF phase. The synchronization system developed by Kiewiet et al. [3] locks the RF oscillator to the laser oscillator, with a timing precision of 20 fs. Combined with the phase jitter added by the klystron, this results in arrival time jitter at the exit of the cavity of ~100-120 fs.

The shot-to-shot variation of the measured average electron energy (measured to be 2 keV in Sec. 5.5.1) adds to the arrival time jitter between the TW laser pulse and the electron bunch at the entrance of the plasma channel. With the use of Eq. (5.12), this leads to a RMS timing jitter of $\sigma_{t,jit} = 22$ fs per meter propagation distance of the electron bunch. This is in agreement with the timing jitter measured from THz coherent transition radiation using a slightly different RF-photogun with the same synchronization system [11].

The total jitter in arrival time between the TW laser pulses and the electron bunches at the entrance of the plasma channel, 114 cm from cathode, is approximately 150 fs.
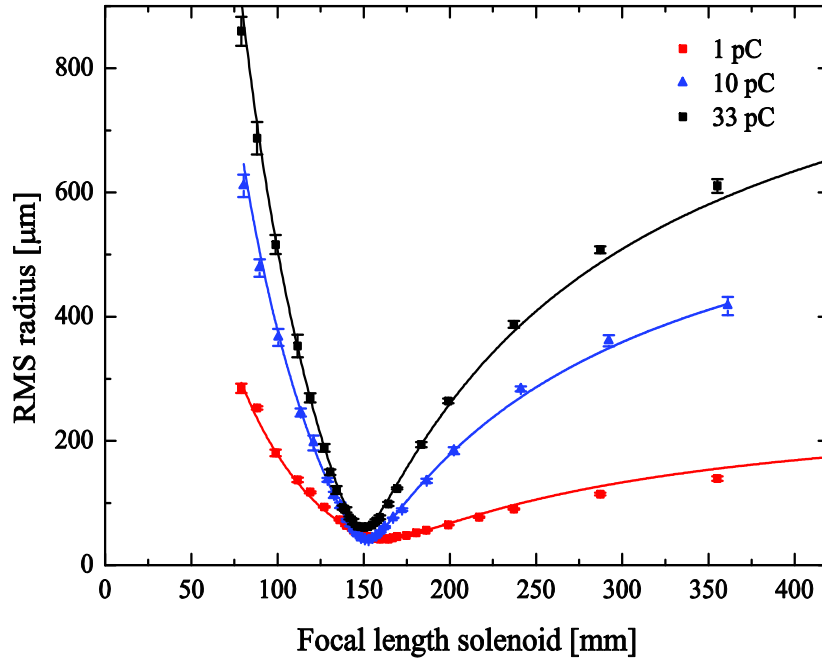
Figure 5.14: Focus scan of a 1, 10 and 33 pC bunches to determine normalized emittance. The dots with error bars are measurement and the solid lines are the fits using Eq. (5.14).

5.5.3 Normalized transverse emittance

The normalized transverse emittance of a low-charge bunch can be determined by performing a focus scan of the electron bunch. The scan is done by measuring the RMS radius of the electron spot on the phosphor screen while changing the focal length (Eq. (5.3)) of the pulsed solenoid lens (see section 5.3.2). The spatial resolution of the imaging system for this phosphor screen is 6 μm. For each setting of the focal strength, a Gaussian function:

$$I = I_0 \exp\left[-\frac{\left((x-x_0)^2 + (y-y_0)^2\right)}{2\sigma_r^2}\right], \tag{5.13}$$

is fitted to the intensity profile on the phosphor screen of a single electron bunch. Here, I_0 is the intensity at the center of the bunch at the position (x_0, y_0) and σ_r the RMS radius. The results of such measurements for 1, 10 and 33 pC bunches are represented by the dots in Fig. 5.14. A measured RMS radius in Fig. 5.14 is the average of 10 consecutive shots at the same focal length for the same charge. The error bars indicate the standard deviation between the 10 shots at each setting.

As the bunch is cylindrically symmetric, $\sigma_r = \sigma_x = \sigma_y$ and $\varepsilon_x = \varepsilon_y$, with σ_x, σ_y the RMS spread in x- and y-direction and $\varepsilon_x = \varepsilon_y$ the emittance in x- and y-direction. Using geometrical optics

97

(neglecting space charge and possible aberrations in the pulsed-solenoid lens), the following equation can be derived for the size of the focal spot as a function of the focal strength of a (thin) lens [11]:

$$\sigma_x = \sqrt{\left[l_1 l_2 - \left(l_1 + l_2\right) f_{sol}\right]^2 \frac{\varepsilon_x^2}{\sigma_{vt}^2 f_{sol}^2} + \left(f_{sol} - l_2\right)^2 \frac{\sigma_{vt}^2}{f_{sol}^2}} \tag{5.14}$$

with f_{sol} the focal length of the pulsed solenoid lens (Eq. (5.3)), ε_x the emittance in x-direction in configuration space, and $l_2 = 0.14$ m the distance between the centre of the pulsed solenoid lens and the phosphor screen. σ_{vt} can be interpreted as the RMS radius of a virtual electron bunch source at a distance l_1 before the pulsed solenoid lens. In order to determine the emittance, Eq. (5.14) was fitted to the measurements using ε_x, l_1 and σ_{vt} as fitting parameters. The result is shown as the solid curves in Fig. 5.14. The normalized emittance, $\varepsilon_{n,x}$, is found using $\varepsilon_x = \varepsilon_{n,x}/\gamma\beta$, with $\beta = v/c$. This results in a normalized emittance $\varepsilon_{n,x} = \varepsilon_{n,y} = 1.9$ μm for a 10 pC electron bunch. This is slightly higher, but in fair agreement (considering the earlier assumptions) with the value of 1.2 μm found from simulations using GPT (General Particle Tracer code [14, 15]). The normalized emittance $\varepsilon_{n,x} = \varepsilon_{n,y}$ for a 1 and 33 pC electron bunch are found to be 1 μm and 3.7 μm, respectively. For a 1 pC bunch, the measured emittance is equal to the simulated emittance. For a 33 pC bunch, the simulated emittance is 2.5 μm, which is significantly smaller than the measured value of 3.7 μm. This may indicate that the charge and thus the charge density at focus of the 33 pC bunch becomes too high to determine the emittance from a focus scan as described in this section, because of the effects of space charge. Measurements using the pepper pot emittance diagnostic can be used to further investigate these effects, as this method is independent of charge [4].

5.5.4 Focus spot and focus stability

For injection of the electron bunches into a plasma channel for LWA, one of the most important parameters is the minimum spot size that can be achieved at a certain bunch charge. In addition, the focus spot stability determines how much charge can be injected consistently.

By means of the solenoid around the RF-photogun, sub-50-pC electron bunches can be kept quasi parallel during propagation through the beam line and thus on the same order as the spot size of the UV-pulse on the cathode. The radius of the electron bunch is typically around 2 mm FWHM at the entrance of the pulsed-solenoid focusing lens. An electron bunch with a bigger radius entering the pulsed solenoid will result in a smaller focus spot at the plasma channel, but will also result in a longer electron bunch at focus because of path length differences introduced by focusing. A longer bunch length gives a lower peak current at focus. On the other hand, an electron bunch with a radius that is too small in the pulsed solenoid will result in focus spot that is large compared to the matched spot size of the laser pulse in the plasma channel, so that fewer
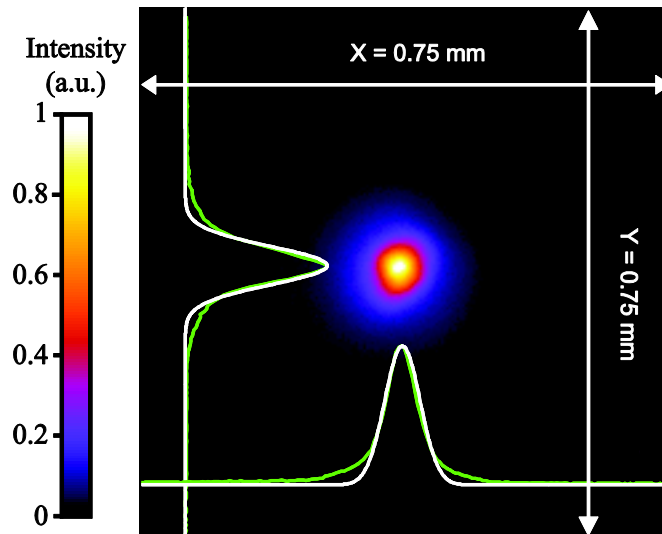
Figure 5.15: Focal spot of a 10 pC electron bunch on a phosphor screen 140 mm behind the pulsed solenoid. The intensity profile at the point of max intensity (green line) with a Gaussian fit (white line) gives an RMS radius of 40 μm.

electrons will be trapped in the wakefield (see chapter 6). A low peak current and a big focus spot are not beneficial for LWA experiments. A compromise between smallest spot and shortest bunch at focus is found (with GPT) when an electron bunch with a 2 mm FWHM radius enters the pulsed-solenoid focusing lens.

This lens focuses the electron bunch on a phosphor screen 140 mm further downstream (see Fig. 5.1), where the plasma channel will be placed for LWA. The current through the pulsed solenoid is adjusted to produce the smallest possible spot on the phosphor screen (the minimum of Fig. 5.14). A picture of the focal spot of a 10 pC electron bunch can be seen Fig. 5.15. The green lines are line- outs of the intensity through the center of the spot. The white lines are Gaussian fits to these line- outs. The RMS width at the focal point is 40 μm in both x- and y-direction. The plasma density of planned LWA experiments with external injection of electrons is typically around $10^{24}\,\mathrm{m}^{-3}$. The matched spot size for laser guiding in such a plasma is around 20-50 μm [6, 16-18], in the same range as the measured focal spot, so that it can be expected that a reasonable fraction of the electron bunch can be captured and accelerated in LWA (a detailed simulation using all measured parameters will be presented in chapter 6).

An important parameter is the shot-to-shot stability of the center of the focused electron bunches, because the position of the focus needs to remain stable within a fraction of the spot size to be able to consistently inject electrons into a plasma channel for LWA. A measurement of this parameter can be seen in Fig. 5.16. This figure shows the number of electron bunches counted as a function of the distance between the centre of each focus and the average position of the centers. This is done in x- and y-direction for 50 consecutive shots. This gives a shot-to-shot stability of the centre of the focused bunch with a RMS spread in x- and y-direction of respectively 5 μm and 4 μm. It is well below the measured RMS spot size of 40 μm.
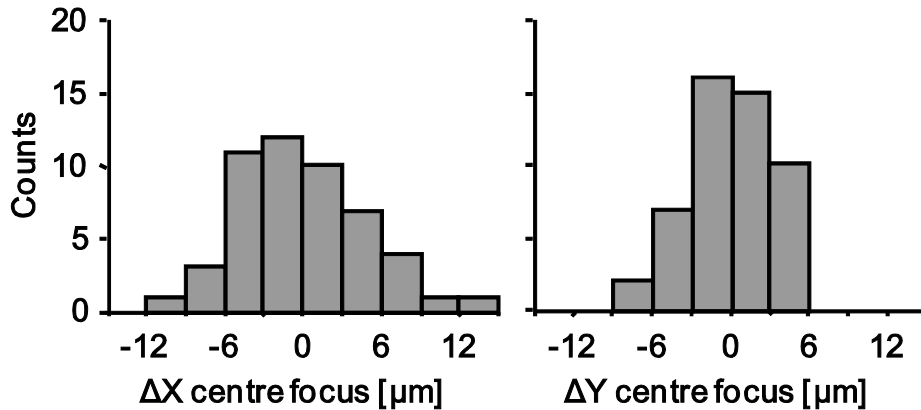
Figure 5.16: Shot-to-shot stability of the centre of the focused electron bunch for 50 consecutive shots in *x*- and *y*-direction.

These results concerning spot size and stability are comparable to those of the TW laser focus at the entrance of the plasma channel that were discussed in Sec 2.3. The combined variations of the laser pulses and the electron bunches at the entrance of the plasma channel are still much smaller than the laser spot and bunch size. This shows that there is always good overlap between the injected electron bunch, the laser pulse and the plasma channel.

5.5.5 Bunch length at focus

The bunch length at the focus is determined by the combination of many parameters, namely duration and radius of the UV-pulse on the cathode, RF-phase of the photogun on which the UV-pulse is injected, energy spread of the electron bunch, distance between cathode and pulsed solenoid lens, distance between phosphor screen and focusing solenoid lens, current in the focusing solenoid lens, current in the solenoid around the cavity, bucking coil current, diameter of the electron bunch in the focusing solenoid lens and charge of the bunch.

An accurate bunch length measurement of sub-picosecond relativistic electron bunches ($\beta \approx 1$) requires a separate, complicated setup, that could not be implemented in the present experiments. For bunch length, we therefore rely on particle tracking simulations using GPT. These simulations have been compared to (and found to be in good agreement with) measurements of the electric field strength of THz coherent transition radiation using electro-optical sampling in a similar setup [11]. The entire beam line, including the accelerator and solenoid lenses was simulated in GPT with the same settings (RF power, charge, laser spot size and magnetic fields) as those used in the experiments. This resulted in a RMS bunch length of 405 fs at focus for a 10 pC bunch. In section 5.5.2 the bunch lengthening was calculated due to the measured energy spread of the bunch (caused by space charge inside the bunch). This effect accounts for 250 fs of the simulated 405 fs. The extra 155 fs compared to the result described in sec. 5.5.2 is due to the increasing space charge while the bunch is being focused.

5.5.6 Effect of charge on focused electron bunch

All the measurements above were done on 10-pC electron bunches. To investigate the effect of the bunch charge on these parameters, we have changed the energy of the UV pulse. At the cathode, the initial bunch length is approximately equal to the length of the UV pulse (~ 50 fs). Changing the energy of the UV-pulse will results in a change of charge with the same initial bunch length and will therefore result in different space charge forces in the electron bunches. Space charge has an effect on almost all previously measured parameters of the electron bunch.

For higher charge, the energy spread will increase. As mentioned earlier, the (Coulomb) space charge force on the electrons in the front of a bunch will be in the forward direction, whereas the space charge force on the electrons in the rear of the bunch is in the backward direction. This leads directly to a higher energy spread at higher charge. The RF phase at which the electrons are created (72º before crest in the RF field for 3.71 MeV electron bunches) partly compensates the bunch-lengthening due to space charge, because the electrons at the front of the bunch are accelerated in a slightly lower RF field than those at the back. Another effect of space charge which relates to the energy spread is the radial expansion of the bunch. Electrons at larger distances from the axis experience a slightly different accelerating field. This effect is mostly compensated by increasing the magnetic field strength of the solenoid around the cavity when increasing the charge. The overall effect is that the energy spread of a bunch of 1 pC was measured to be 0.3 % which increases to 1.5 % for 35 pC bunches (see Table 5.1).

The transverse (normalized) emittance is also affected by space charge. Higher space charge will result in a higher (normalized) transverse emittance and consequently, in a larger spot size at the point of focus (see sec. 5.5.3). Measurements and GPT simulations of the smallest possible focus spot can be seen in Fig. 5.17. The measured RMS radius of the focus spot becomes significantly larger at higher charge and increases from ~30 μm at 1 pC to ~60 μm for a 35 pC electron bunch. Simulations of the smallest possible focus spot show the same increasing trend at higher charge. The simulations have been done using the experimental

Table 5.1: Properties of the electron bunches at focus for different charges. The measurements presented are the transverse RMS radius of the electron bunch, the energy spread and the transverse normalized emittance in *x*- and *y*-direction. RMS bunch lengths were simulated with GPT using other measured properties as input.

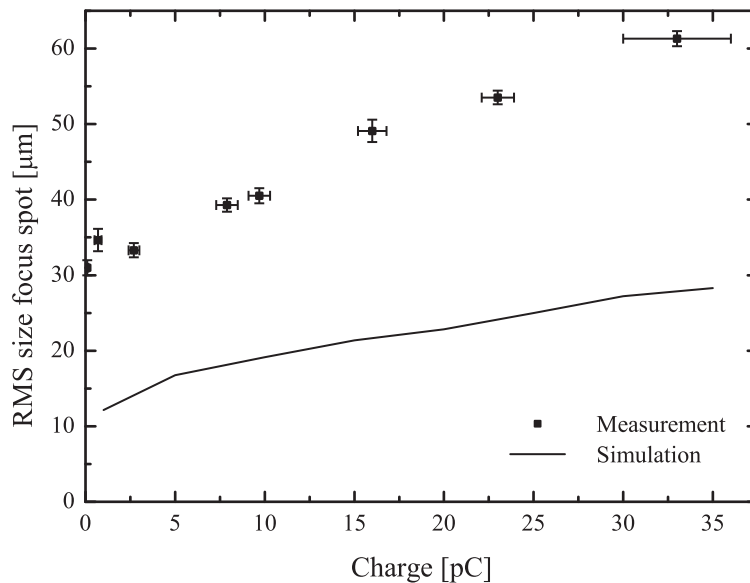| Charge [pC]	1	10	16	33
RMS radius focus spot [μm]	32	41	49	61
Simulated RMS bunch length focus [fs]	147	405	551	845
Energy spread [%]	0.3	0.5	0.8	1.5
Trans. Normal. emittance [μm]	1.0	1.9	2.3	3.7

Figure 5.17: Measurements (dots) and simulation (line) of the smallest RMS radius at focus of the electron bunch at 1.14 meter from the cathode as a function of the charge of the electron bunch.

settings for the current through the solenoids, bucking coil current, γ and UV spot size. The spot size in the experiments is roughly a factor of two larger than the spot size predicted by the simulations. The difference between measurements and simulations are possibly caused by an asymmetry of the field in the pulsed solenoid (which was not taken into account in the simulations). During the experiments we noticed that the solenoid had to be slightly tilted ($\sim 5°$) to keep the focused and unfocused bunch at the same position on the phosphor screen. This asymmetry may be due to the lead wires to the solenoid or due to the stray fields that possibly induced currents in the beam pipe in the vicinity of the pulsed solenoid (the beam pipe inside the solenoid is made of glass, but extends only 10 mm outside the solenoid, perhaps this needs to be increased).

Electrons in a bunch with a certain energy spread and thus a different velocity arrive at the point of focus at a different point in time. Bunches with higher charge will therefore be longer at the point of focus compared to low charge bunches. GPT simulations show that the RMS bunch length at focus in the described setup increases from 147 fs for a 1-pC bunch to 870 fs for a 35-pC bunch.

An overview of RMS radius and bunch length at focus, energy spread and emittance versus accelerated charge for a 3.71 MeV electron bunch can be seen in Table 5.1.

The focus spot of the bunches with a charge of 10 pC or less is almost completely cylindrically symmetric, as can be seen in figure 5.15. At higher charges, the spot often seems somewhat distorted, as shown in figure 5.18.b. This X-shape turns out to be caused by a slight asymmetry in the laser spot on the cathode. For the shot shown in Figure 5.18.b, the laser spot
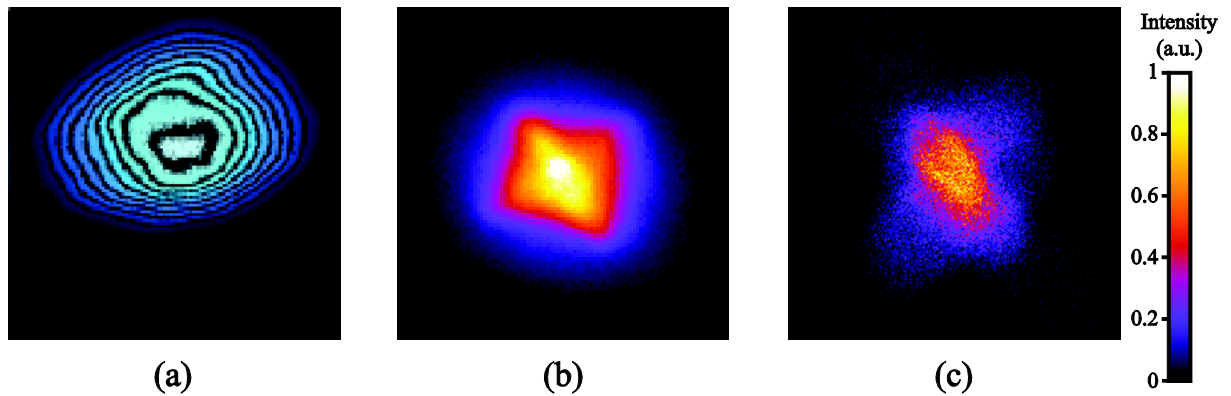
Figure 5.18: (a) Measured profile of 266 nm laser pulse at cathode to generate 20 pC electron bunch, the black lines are iso-intensity lines, (b) measured focus of the 20 pC electron bunch, (c) simulated focus spot of the 20 pC electron bunch.

was measured on the virtual cathode, Figure 5.18.a. This measurement of the laser spot was used as input for a GPT simulation. The simulation shows the same X-shape as the measurements, see Figure 5.18.c. Further simulations, using measured laser spots, showed that this asymmetry does not contribute significantly to the spot size at the focus. It does therefore not explain the difference between the measurements and simulations in Figure 5.17.

The shot-to-shot energy stability and the shot-to-shot stability of the position of the focal spot show no dependence on charge, as expected. The extra (RMS) timing jitter between the electron bunch and the TW laser pulse at the entrance of the plasma channel remains 22 fs (per meter propagation distance of the electron bunch), as discussed in section 5.5.2. The focus stability of the electron bunches is also charge independent and shows an RMS spread of 5 μm.

5.6 Conclusions

Measurements have been performed to characterize an RF-photogun, purpose-built as an electron injector for LWA. It was found that the RF-photogun satisfies the conditions to serve as a suitable electron injector for LWA with electron injection. This opens the way for LWA experiments in which the effects of injected electron bunches, plasma parameters and laser parameters on LWA can be studied separately.

The experiments with laser pulses with central wavelengths of 266 nm and 400 nm show that sufficient charge, tens of pC, can be made at either wavelength. The results at 266 nm show a first and second order effect in the dependence of charge on laser pulse energy. The measurements at 400 nm show only a second order effect (as expected). Because no effect on the focus spot size, emittance or energy spread of the electron bunches was observed, 400 nm pulses can be used to generate the electron bunches needed for LWA. These results allow

simplification of the laser system, because the generation of 400 nm pulses with this laser system (which produces pulses at a fundamental wavelength of 800 nm) is much easier than 266 nm.

In the experiments presented here, electron bunches of 10 pC were produced by the RF-photogun with a kinetic energy of 3.71 MeV and energy spread of 0.5%. These electron bunches were focused to a spot with an RMS radius of 40 μm. The shot-to-shot stability of the centre of the focused bunch had an RMS spread of 5 μm. This shot-to-shot stability is well below the measured RMS radius of 40 μm. This is an important parameter to perform successful LWA experiment with externally injected electrons because a consistently large overlap between plasma channel and injected electron bunch is necessary for the production of stable accelerated bunches. This condition is fulfilled as the matched spot size for guiding of most plasma channels considered for LWA experiments is on the order of 30 μm.

The synchronization between the UV-pulse at the cathode and the phase of the RF wave, combined with the variations in RF output power of the klystron leads to a shot-to-shot energy stability of 0.05% (2 keV). This results in an extra RMS timing jitter of 22 fs per meter drift length after the exit of the RF photogun between electron bunch at the focus and the TW laser pulse. The total jitter at the entrance of the plasma channel (1.14 m from the cathode), is estimated to be 150 fs.

For LWA in the non-linear regime with electrons injected in front of the laser pulse the energy needs to be in the range 3-4 MeV. Electrons with too low energy will not get accelerated by the wakefield and electrons with too high energy will not be overtaken by the laser pulse in the plasma. The RF-photogun described in this chapter here is perfectly capable of operating in this regime. For injection in this regime, a laser system that produces laser pulses with a power higher than 15 TW is required.

For injection of electron bunches behind the laser pulse and acceleration in the linear regime, a laser system of only ~3 TW is required, but the injected electrons need a kinetic energy higher than 6 MeV. To operate in this regime, the photogun needs further conditioning.

References

[1]   O. J. Luiten, S. B. van der Geer, M. J. de Loos, F. B. Kiewiet, and M. J. van der Wiel, *How to Realize Uniform Three-Dimensional Ellipsoidal Electron Bunches*, Phys. Rev. Let., Vol. 93, 094802, (2004).

[2]   T. P. Wangler, RF Linear Accelerators, second edition, Wiley-VCH, ISNB: 978-3-527-40680-7, p. 282, (2008).

[3]   F. B. Kiewiet, A. H. Kemper, O. J. Luiten, G. J. H. Brussaard, M. J. van der Wiel, *Femtosecond synchronization of a 3 GHz RF oscillator to a mode-locked Ti:sapphire laser.* Nucl. Instr. and Meth. in Phys Res. A, Vol. 484, p. 619. (2002).

[4]   S. Humphries Jr., *Charged Particle beams*, John Wiley and Sons, ISBN 0-471-60014-8, (1990).

[5]   E. R. Colby, Design, *Construction, and Testing of a Radiofrequency Electron Photoinjector for the Next Generation Linear Collider*, PhD thesis, University of California, Fermilab-Thesis-1997-03, (1997).

[6]   W. H. Urbanus, W. van Dijk, S. B. van der Geer, G. J. H. Brussaard and M. J. van der Wiel, *Front-to-end simulations of the design of a laser wakefield accelerator with external injection*, J. Appl. Phys., Vol. 99, 114501, (2006).

[7]   S. Humphries Jr., *Principles of Charged Particle Acceleration*, Wiley and Sons, ISBN: 0-471-87878-2, (1999).

[8]   K. A. Daamen, *Reverse engineering the INGCRYS Laser Systems Ltd. Third Harmonic Generation*. Eindhoven University of Technology, Bachelor thesis, (2007).

[9]   R. Akre, D. Dowell, P. Emma, J. Frisch, S. Gilevich, G. Hays, Ph. Hering, R. Iverson, C. Limborg-Deprey, H. Loos, A. Miahnahri, J. Schmerge, J. Turner, J. Welch, W. White, and J. Wu, *Commisioning the Linac Coherent Light Source*, Phys. Rev. ST Accel. Beams, Vol. 11, 030703, (2008).

[10] F. Kiewiet, *Generation of ultra-short, high brightness relativistic electron bunches*, PhD thesis, Eindhoven University of Technology, ISBN: 90-386-1815-8, (2003).

[11] W. P. E. M Op 't Root, M. J. de Loos, S. B. van der Geer, A. H. Kemper, E. H. Rietman, M. J. van der Wile and O. J. Luiten, *Second generation TU/e RF-photogun*, submitted op Phys. Rev. ST Accel. Beams, (2010).

[12] W. Li and D. Y. Li, *On the correlation between surface roughness and work function in copper*, The Journal of Chemical Physics, Vol. 122, 064708, (2005).

[13] J. Diels and W. Rudolph, *Ultrashort laser pulse phenomena,* Academic Press Inc., ISBN: 0-12-215492-4, (1996).

[14] www.pulsar.nl/gpt.

[15] Gisela Pöplau, Ursula van Rienen, Bas van der Geer, and Marieke de Loos, *Algorithms for the fast calculation of space-charge effects in accelerator design*, IEEE Transactions on Magnetics, Vol. 40 part 2, p. 714, (2004).

[16] A. G. Khachatryan, F. A. van Goor, K.-J. Boller, A. J. W. Reitsma and D. A. Jaroszynski, *Extremely short relativistic-electron-bunch generation in the laser wakefield via novel bunch injection scheme*, Phys. Rev. ST Accel. Beams, Vol. 7, 121301 , (2004).

[17] A. Irman, M. J. H. Luttikhof, A. G. Khachatryan, F. A. van Goor, J. W. J. Verschuur, H. M. J. Bastiaens, and K.-J. Boller, *Design and simulation of laser wakefield acceleration with external electron bunch injection in front of the laser pulse*, J. Appl. Phys., Vol. 102., 024513, (2007).

[18] W. van Dijk, S. B. van der Geer, M. J. van der Wiel, and G. J. H. Brussaard, *Parameter study of acceleration of externally injected electrons in the linear laser wakefield regime*,

Chapter 6

Simulations of electron injection in front of the laser pulse using the measured electron bunch parameters.[1]

6.1 Introduction

The electron bunches as measured and described in section 5.5 can be used as external electron source for LWA. Two different schemes exist for injection. One is with injection of the electron bunches in front of the laser pulse, the other with injection behind the laser pulse, as described in section 1.2. For relatively low laser power, the plasma wave can be described by simple harmonics. This is designated as the 'linear regime'. These waves are generated with a laser power corresponding to a normalized laser vector potential between ~ 0.25 and ~ 0.4, which is typically between 2 and 5 TW on a ~ 30 μm spot size ($1/e^2$ intensity), at a plasma density of ~ 1×10^{24} m^{-3}. When working in this regime, the electron bunch must be injected behind the laser pulse. The pre-accelerated electrons need to have an energy of more than ~ 5 MeV to be trapped and accelerated in these waves [1, 2], so the electron bunches with the present energy of 3.7 MeV do not have sufficient energy for acceleration in the linear regime.

---

[1] Based on: X.F.D. Stragier, S.B. van der Geer, M.J. van der Wiel, O.J. Luiten and G.J.H. Brussaard, "An RF photogun for external injection of electrons in a Laser Wakefield Accelerator", Proc. SPIE Vol. 8079, 80790W (2011)

The RF-photogun is designed to produce electron bunches with a maximum kinetic energy of 6.7 MeV (SUPERFISH and GPT) at a maximum on axis electric field of 97 MV/m. At present, the maximum field is limited to 50 MV/m due to breakdown. Further conditioning of the RF–photogun could result in a kinetic energy higher than 5 MeV but this was not yet reached in the experiments.

At higher laser power, the plasma waves become nonlinear. In this regime, electrons that are injected at lower energy can be trapped and accelerated. It is favorable to inject electrons in front of the laser pulse, so that the laser pulse overtakes the electrons inside the plasma and compresses, traps and accelerates the electrons in the first trough ('bucket') behind the laser pulse. To operate in this regime, laser power of >10 TW is required ($a_0 > \sim 0.7$) to trap and accelerate bunches injected at 3.7 MeV [3-5].

To determine what kind of electron bunches can be created in LWA, using the experimental results of chapter 5, this chapter describes simulations using the General Particle Tracer (GPT) code [6] with the electron bunches injected in front of the laser pulse. The injected electron bunch parameters used in the GPT simulations are the measured parameters as presented in section 5.5. In the present chapter, the effects on the accelerated electrons after plasma acceleration of the injected charge (Section 6.2.1), the laser power (Section 6.2.2) and the plasma density (Section 6.2.2) are examined.

6.2 Simulations

Simulations have been done for LWA with externally injected electrons in front of the laser pulse using the actual measured bunch parameters from table 5.1. All injected electron bunches have an energy of $E_{inj} = 3.7$ MeV. Because the length of the plasma channel is up to 15 cm, full particle-in-cell (PIC) simulations will take too long to perform and are therefore not practical. The laser wakefield potential used in the present simulations is based on the analytical description of Andreev [7] and is used as the field map in GPT. To keep the calculation time acceptable, the wakefield potential and laser pulse envelope are assumed to be time-independent in the frame of the laser pulse (quasi-stationary solution), similar to the approach of Van Dijk [1, 8-9]. We believe this assumption is realistic because the charge density of the electron bunch is low, compared to the plasma density. The charge density is $\sim 10^5$ times lower than the plasma density for the injected electron bunch and ~ 10 times lower for the bunch at the exit of the plasma channel. Reitsma shows that the effect of the bunch on the wakefield is still small in this regime [10]. Further we assume that the laser pulse that creates the plasma wave is Gaussian and is matched to the plasma channel with a parabolic radial electron density profile (see also chapter 3), so that the laser is guided through the plasma with a constant radius. The most critical assumption is that the plasma has no effect on the laser pulse, so that there is no change in laser frequency, the laser beam envelope remains constant during propagation

through the plasma and laser energy depletion is neglected [8]. These assumptions will befurther addressed in section 6.2.2. where the simulations will be compared to simulations by Luttikhof [5, 11], who used a different code to calculate the wakefield potential.

In the simulations, the laser wakefield (potential) starts behind the electron bunch and propagates at a speed equal to the group velocity of the laser pulse in the plasma. The wakefield will overtake the electron bunch inside the plasma and part of the injected electron bunch will be focused and accelerated by the wakefield. The length of the plasma was chosen to achieve maximum average acceleration of the injected electron bunch, i.e. to the point of dephasing. When injecting the electron bunch in front of the TW laser pulse, only one accelerated bunch is expected, trapped in the first trough of the wakefield behind the laser pulse. The measured transverse emittance of the injected electron bunch was taken into account during the simulations. To determine the optimal delay between the laser pulse and the electron bunch at the entrance of the plasma channel, the charge of the electron bunch at the exit of the plasma was taken as the criterion. The optimal delay was found to be ~2.5 times the RMS length of the electron bunch at the focus.

6.2.1 Accelerated charge

In these simulations, a 50 fs laser pulse (FWHM) with a power $P_l = 25$ TW and a central wavelength of 800 nm, focused to a waist $w = 30$ μm ($1/e^2$ intensity) in a plasma channel with a density $n_e = 0.7 \times 10^{24}$ m^{-3} was used (the normalized laser vector potential in this case is $a_0 = 0.9$). For this combination of parameters with an optimized plasma length (dephasing length) of 10 cm, the electrons are accelerated in one single bunch to ~900 MeV. Fig. 6.1 shows the result of the accelerated charge at the exit of the plasma channel versus the injected charge from the RF-photogun. The black dots represent simulations with electron bunches focused at the entrance of the plasma channel with the plasma surrounded by a capillary with a radius of 200 μm. The accelerated charge initially increases with increasing injected charge. As the charge is increased further, the electron bunches become longer due to the space charge forces, as explained in Section 5.5.6. The charge density at the center of the bunch at focus reaches a maximum around 7 pC. To collect maximum charge, the delay between laser and electron bunch also has to become larger for longer bunches. The larger delay together with a longer bunch results in a longer time for the laser to overtake the electron bunch. At the highest simulated charges, the electron bunch becomes so long that the laser will not completely overtake the injected electron bunch before the dephasing length is reached, where the front of the bunch already starts to be decelerated. The divergence of the electron bunch after the focus (caused by the emittance) also contributes to a decrease in the accelerated charge. For higher charged bunches (with larger initial emittance), the laser will overtake fewer and fewer electrons during propagation in the plasma channel, resulting in a lower accelerated charge. These effects together lead to a maximum accelerated charge of 0.4 pC at 7 pC initial bunch charge (black dots in Fig. 6.1).
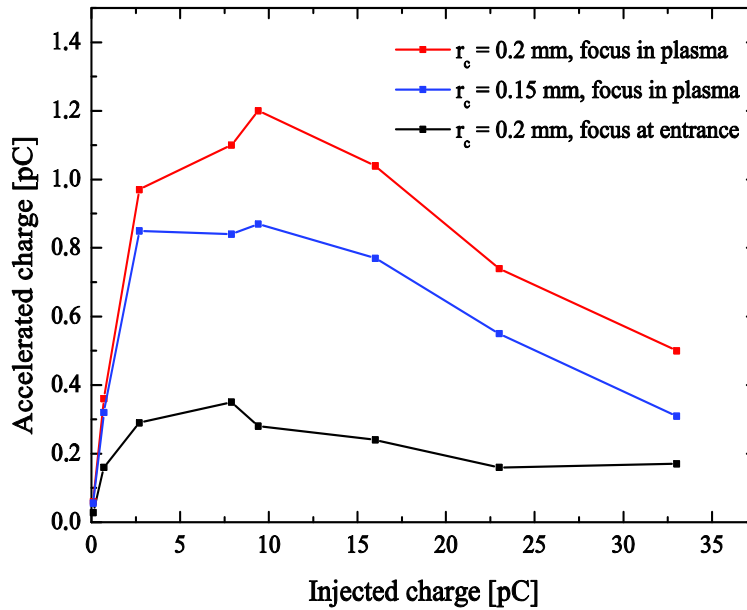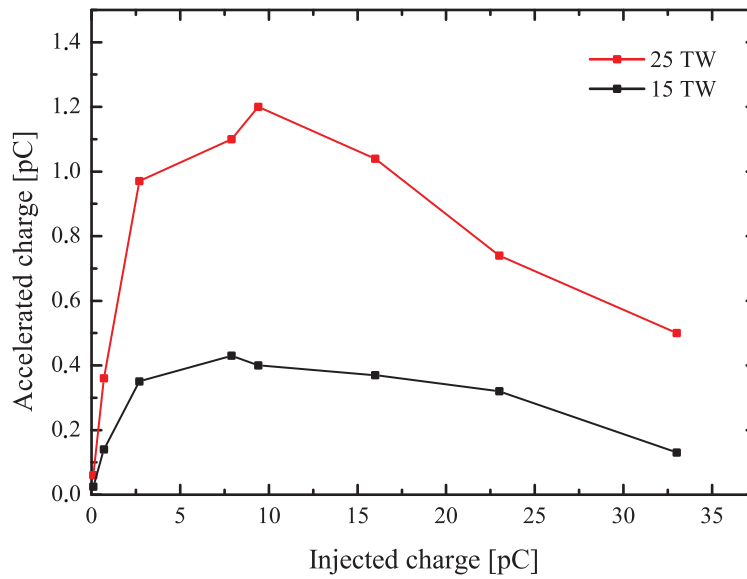
Figure 6.1: Simulations of the accelerated charge after LWA versus injected charge coming from the RF-photogun, based on realistic electron bunch parameters from the RF-photogun. $P_l = 25$ TW, $w = 30$ μm, $n_e = 0.7 \times 10^{24}$ m^{-3}, $E_{inj} = 3.7$ MeV. Black: electron bunch focus at the entrance of the plasma channel, radius capillary $r_c = 200$ μm. Blue: electron bunch focus 2 cm inside the plasma channel, $r_c = 150$ μm. Red: electron bunch focus 2 cm inside the plasma channel, $r_c = 200$ μm.

The effect of the divergence of the electron bunch after the focus can be reduced by focusing deeper inside the plasma channel. Focusing the electron bunch inside the plasma channel is effective because the average electron density of the electron bunch while being overtaken by the laser is higher compared to the case where the electron bunch is focused at the entrance of the plasma channel. The red dots in Fig. 6.1 represent simulations with the focus of the electron bunch 2 cm inside the plasma channel (which is the optimal setting). The red dots follow a trend similar to that of the black dots, but the collection efficiency is almost a factor of 3 higher. It must be noted that in these simulations the plasma is surrounded by a capillary with a 200 μm radius. When focusing 2 cm in the capillary, the electrons on the outer edge of the bunch are blocked when entering the capillary. This applies in particular to the higher charged bunches because they have a larger radius (see Sec 5.5.6). The blue dots in Fig. 6.1 are simulations with an electron focus 2 cm inside the plasma channel, but here the plasma is surrounded by a capillary with a radius of 150 μm. As the radius is smaller compared to the 200 μm case (red), more electrons are blocked by the capillary wall when the electron bunch is entering the capillary and therefore the accelerated charge is lower. Because the guiding experiments (chapter 3) were done with a capillary with a radius of 150 μm this is the most realistic setting for future experiments.
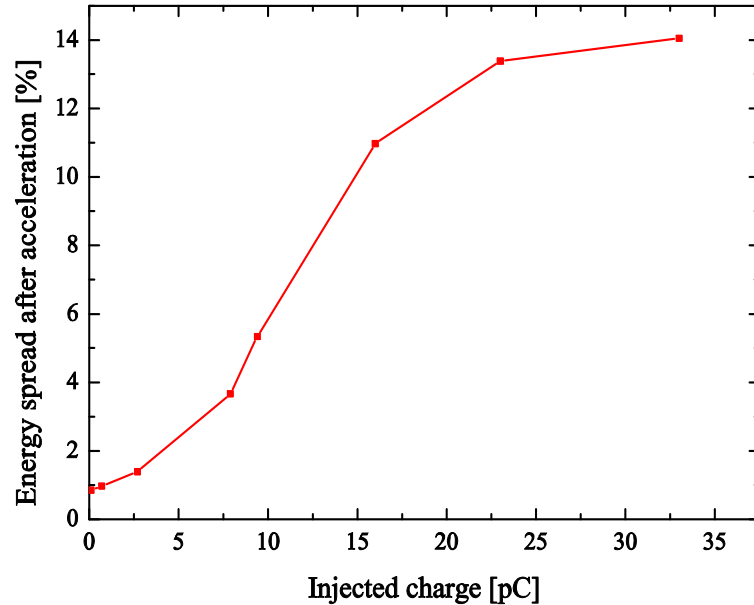
Figure 6.2: Simulations of the energy spread after LWA as function of injected charge when focusing f = 2 cm inside the plasma channel. P_l = 25 TW, w = 30 μm, n_e = 0.7×10^{24} m^{-3}, E_{inj} = 3.7 MeV, r_c = 200 μm, f = 2 cm.

Higher injected charge also results in a higher energy spread, because it takes longer to overtake the (longer) electron bunch, as can be seen in Fig. 6.2. This effect becomes significant for bunches longer than ~400 fs, or 10 pC. At the highest charges, the energy spread stabilizes at ~ 15% because the capillary is ended at the dephasing length.

As a result, for this set of plasma and laser parameters, electron bunches with RMS bunch length shorter than ~400 fs at focus and a transverse normalized emittance lower than ~2 μm are suitable for LWA with external injection in front of the laser pulse.

Simulations in Fig. 6.1 show a maximum accelerated charge around an injected charge of 10 pC. For these settings, there is no advantage in injecting electron bunches with a charge higher than 10 pC because not only does the accelerated charge decrease, but also the energy spread of the accelerated bunches increases at higher injected charges. At the optimized settings (focusing 2 cm inside the plasma channel) a charge of 1.2 pC can be accelerated to ~900 MeV with energy spread of ~5% in a 10 cm long plasma channel (dephasing length). The RMS radius of the accelerated bunch after acceleration is found to be 1.5 μm and the RMS bunch length is 2.5 μm (~8 fs), resulting in a peak current of ~ 100 A.

6.2.2 Effect of laser power

The effect of the laser power on the accelerated charge, energy and the energy spread is examined. A comparison is made for a 25 TW and a 15 TW laser pulse focused to a 30 μm

Figure 6.3: Simulations of the accelerated charge after LWA versus injected charge coming from the RF-photogun, based on realistic electron bunch parameters from the RF-photogun for a 25 TW (red) and a 15 TW (black) laser pulse. $n_e = 0.7 \times 10^{24}\,\mathrm{m}^{-3}$, $E_{inj} = 3.7$ MeV, $r_c = 200$ μm, $f = 2$ cm, $w = 30$ μm.

waist at the entrance of the plasma channel. Simulations have been done with a plasma density of $n_e = 0.7 \times 10^{24}\,\mathrm{m}^{-3}$. To guarantee maximal accelerated charge, the electrons are focused 2 cm inside the plasma as described in the previous section (6.2.1). The capillary surrounding the plasma has a radius of 200 μm.

The energy of the accelerated electrons can be modified by changing the laser power. A lower laser power generates a lower wakefield potential in the plasma and therefore a lower energy of the accelerated electrons can be expected. The energy of the electrons after LWA is found to be ~900 MeV for the 25 TW and ~ 600 MeV for the 15 TW laser pulse.

The accelerated charge after LWA as function of the injected charge can be seen in figure 6.3. Simulations with a 25 TW laser pulse are represented by the red dots. In Fig.6.1 and 6.3 the red simulations are identical. Simulations with a 15 TW laser pulse are given by the black dots in Fig.6.3. As expected, the trends are similar for the 15 TW and the 25 TW laser pulses. Both sets of simulations show a maximum around 7 pC injected charge, but the accelerated charge is almost a factor 3 lower for the 15 TW laser pulse. The reason for this is that for the 15 TW case the wakefield potential in the plasma is only high enough to collect and accelerate the 3.7 MeV injected electrons close to the axis of the plasma. For the 25 TW laser pulse, also electrons injected farther from the axis still experience a sufficiently high accelerating field to get accelerated, which therefore results in higher accelerated charge. Nowadays, laser systems up to 2 PW exist [12, 13] that can be focused to a much bigger waist (>100 μm) at the entrance of the plasma and still having the same intensity as for a 25 TW system on 30 μm waist. This would greatly increase the distance from the axis where electrons are still accelerated by the wakefield and would result in higher accelerated charge. A laser system with high power is therefore
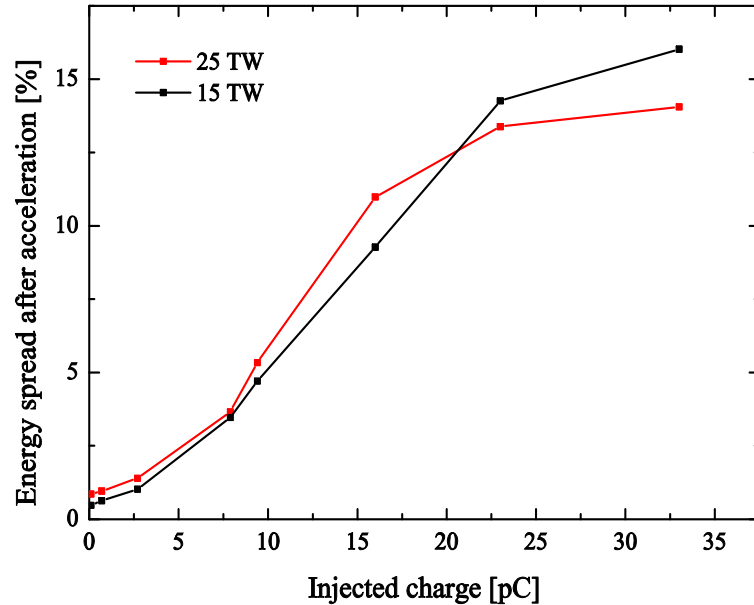
Figure 6.4: Simulations of the energy spread after LWA as function of injected charge for a 25 TW laser pulse (red) and a 15 TW laser pulse. $n_e = 0.7\times10^{24}\,m^{-3}$, $E_{inj} = 3.7$ MeV, $r_c = 200$ μm, $f = 2$ cm, $w = 30$ μm.

desirable. The energy spread for the 15 TW and 25 TW laser pulses is similar and is shown in figure 6.4. Lowering the laser power results in a lower energy and lower charge after acceleration but has little effect on the energy spread.

The collection efficiency for external injection of electrons in LWA was also simulated by Luttikhof [5, 11] using the code WAKE [14, 15], which takes laser pulse evolution during propagation in the plasma into account. With this code, the collection efficiency was found to be ~55 % for a 25 TW and ~27 % for a 15 TW laser pulse for the same plasma and laser setting and the same electron injection energy as used in this section. It was assumed in those simulations, that the injected electron bunch could be focused at the entrance of the plasma channel to a spot of 27 μm RMS radius, an RMS length of 85 fs and with a normalized RMS emittance of 1 μm in x- and y-direction. The bunch length, spot size of at focus and emittance were supposed to be independent of the charge. As a result the collection efficiency was found to be independent of the injected charge. However, the measured focus spot, bunch length and emittance as described in section 5.5 clearly depend on the charge (Sec 5.5.6) and will have an effect on the collection efficiency. In figure 6.5 simulations of the collection efficiency after LWA versus injected charge coming from the RF-photogun, based on the measurements are depicted. The red dots represent the simulations for a 25 TW laser pulse and the black dots for 15 TW. The collection efficiency decreases at higher injected charge as explained in the previous section. The collection efficiency found by Luttikhof for a 25 TW and 15 TW laser pulse are given by the dotted lines in figure 6.5. Both simulations are in agreement at an injected charge of less than 1 pC. In this region, the measured bunch properties approach the properties of the bunches used by Luttikhof in terms of bunch length and emittance (see also
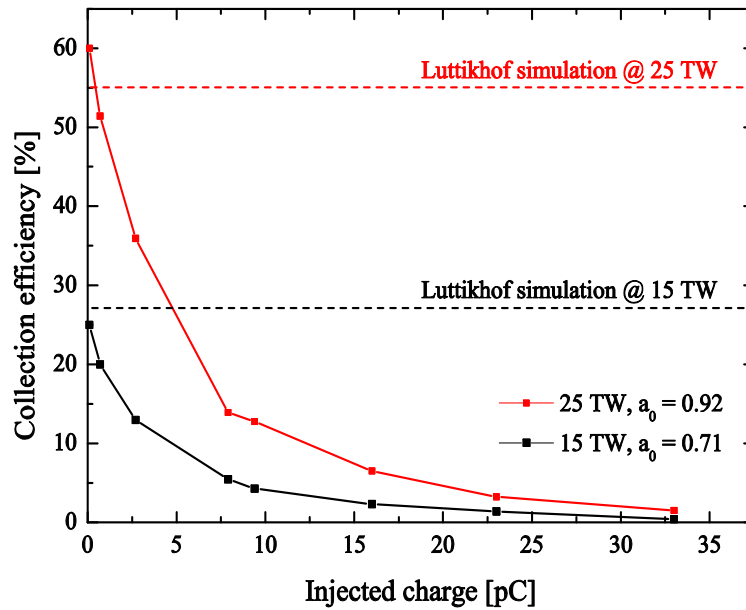
Figure 6.5: Simulation of the collection efficiency versus injected charge, based on measurements of the properties of the electron bunches from the RF-photogun, for a 25 TW (red) and a 15 TW laser pulse (black). Dotted lines represent simulations by Luttihof [5]. $n_e = 0.7 \times 10^{24}$ m^{-3}, $E_{inj} = 3.7$ MeV, $r_c = 200$ μm, $f = 2$ cm, $w = 30$ μm.

Table 5.1). From this comparison, it can be concluded that the simulations used in this chapter and the simulations done by Luttikhof, using a different code, give similar results. The assumptions made with regard to the laser pulse evolution apparently have little effect on the outcome of the simulations. However, the bunch properties of the injected electron bunches significantly influence the results and must be taken into account to make realistic predictions about the bunches after LWA.

6.2.3 Effect of the plasma density

In this section, the effect of the plasma density on the accelerated charge, the kinetic energy and the energy spread is examined. This is done for a 25 TW laser focused in a 30 μm waist at the entrance of the plasma channel. Again, the 3.7 MeV electrons are focused 2 cm inside the plasma channel with 200 μm radius to assure maximum collection efficiency. The dephasing length for a plasma density of 2×10^{24} m^{-3} is found to be 5 cm and 15 cm for a density of 0.5×10^{24} m^{-3}. Successful guiding experiments have been done for plasma lengths up to 8 cm with laser and plasma setting similar to those used in this chapter [16]. Simulations of the accelerated charge versus injected charge for plasma densities of 0.5, 0.7, 1 and 2×10^{24} m^{-3} are shown in figure 6.6. All four sets of simulations show the same tendency and have a maximum around an injected charge of 10 pC. Lowering the plasma density results in a higher
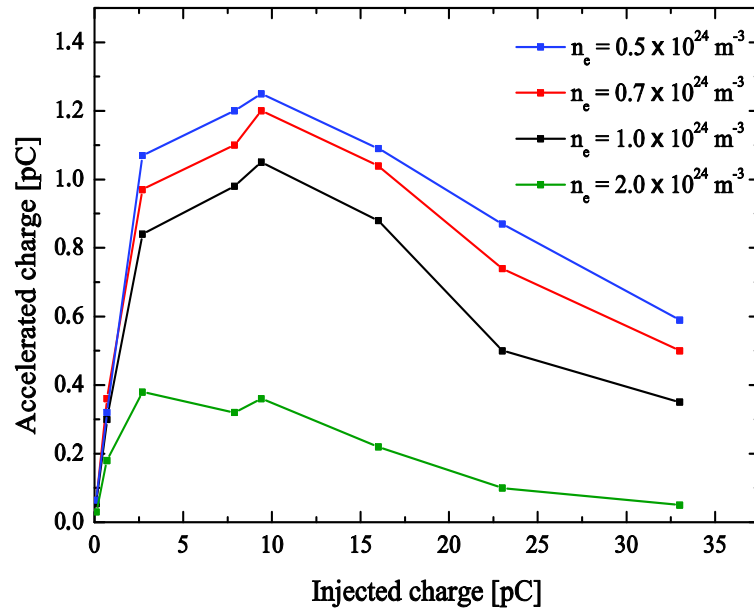
Figure 6.6: Simulations of the accelerated charge after LWA versus injected charge coming from the RF-photogun, based on realistic electron bunch parameters from the RF-photogun for different plasma densities. P_l = 25 TW, w = 30 μm, E_{inj} = 3.7 MeV, r_c = 200 μm, f = 2 cm.

collection efficiency, but changing the density to below 1×10^{24} m^{-3} has only a small effect on the accelerated charge. At lower plasma density, the group velocity of the laser in the plasma is higher and the laser pulse will more rapidly overtake the electron bunch in the plasma. In combination with the divergence of the electron bunch this results in higher collected charge at lower density.

The kinetic energy of the electrons after LWA as function of the plasma density can be seen in figure 6.7. Electrons can be accelerated to energies over 1 GeV at densities under 0.6×10^{24} m^{-3}. A large energy range is available when changing the density. The kinetic energy after LWA becomes higher at a lower density, even though the wakefield potential is lower at lower density. This may sound contradictory, but the dominant factor during this process is the higher group velocity of the laser pulse in the plasma at lower densities. It will take longer for the electrons to slip to the deceleration phase of the plasma wave and the electrons will therefore gain more energy at lower density. The length of the plasma channel is increased for the lower densities, to accommodate the longer dephasing length. Because the bunch is overtaken more rapidly by the laser pulse inside the plasma at lower density, also the energy spread is lower. This can be seen in figure 6.7. However, the simulations that lead to figures 6.6 and 6.7 assume a constant laser waist of 30 μm for the different plasma densities. Although good guiding properties are found in a plasma density between 0.5×10^{24} m^{-3} and 2×10^{24} m^{-3} with a constant laser spot size in section 3.5.3, it is known from experiments elsewhere and simulations, that the matched spot size of the plasma at which the laser pulse is guided through the plasma becomes larger at lower density [17, 18]. This can be compensated in part by using a
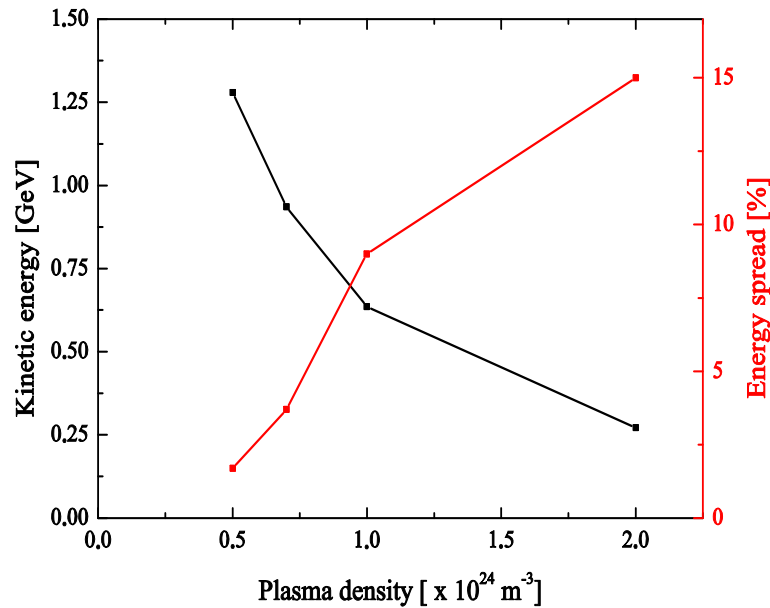
Figure 6.7: Simulations of the kinetic energy and energy spread versus plasma density for an injected charge of 10 pC. $P_l = 25$ TW, $w = 30$ μm, $E_{inj} = 3.7$ MeV, $r_c = 200$ μm, $f = 2$ cm.

capillary with a smaller radius, but if the radius of the capillary becomes too small, the plasma can not be ignited easily and the channel walls may erode, as was observed in some of the laser guiding experiments (see also Sec. 3.4.3). It is therefore likely that lower plasma density will lead to a larger matched spot size. This in turn requires a higher laser power to maintain the same maximum intensity of the laser pulse. PW laser systems that drive a laser wakefield in a meter-long plasma channel at low density are therefore foreseen for acceleration to the 10 GeV level [12, 13, 19, 20].

6.3 Conclusion

Simulations of LWA, using the measured bunch parameters as input, show that electrons can be accelerated in a single bunch to ~900 MeV with energy spread of 5% using a ~10 cm long plasma channel with an on-axis electron density of 0.7×10^{24} m^{-3} in combination with a 25 TW laser pulse focused on a 30 μm spot to drive the plasma wave.

The collection efficiency depends on the injected charge. Producing higher bunch charge in the RF accelerator leads to longer bunch lengths and larger focus spot size, due to space charge. For the parameters chosen in the simulation, there is no advantage to be gained from injecting bunches with charges above 10 pC. At higher charges, the electron bunches become too long at the focus and diverge during the time it takes for the laser pulse to overtake the electron bunch. As a result, the accelerated charge decreases and the energy spread of the accelerated bunch increases. To be specific, the RMS bunch length of the injected electron bunch at the focus

should not exceed 400 fs and its normalized transverse emittance should be lower than 2 μm.

To have an optimal overlap between the TW-laser pulse and the electron bunch, the optimal delay between them was found to be ~2.5 times the RMS length of the electron bunch at the focus. For the electron bunch of 10 pC, with RMS length of 400 fs, the optimal delay is 1 ps. To further optimize the collection efficiency, the position of the focus of the 10-pC injected electron bunch should be placed 2 cm deep inside the plasma channel. This will result in accelerated electron bunches with a charge of 1.2 pC, accelerated to ~900 MeV in a single bunch of ~8 fs (peak current ~ 100 A).

The energy of the accelerated electrons can be tuned by changing the laser power or the plasma density. Changing the laser power has little effect on the energy spread of the accelerated electrons, but has a considerable effect on the accelerated charge. Lower laser power results in less accelerated charge. Changing the plasma density has little effect on the accelerated charge, but has a significant effect on the energy spread. Lower plasma density will result in a higher electron energy after acceleration with a smaller energy spread. However, to achieve this, a longer plasma channel is needed, while the matched spot size to guide the laser is assumed to be the same at lower plasma density. Because it is questionable whether this can be realized in practice, it is expected that higher laser power is needed to accelerate to higher energy.

References

[1] W. van Dijk, S. B. van der Geer, M. J. van der Wiel, and G. J. H. Brussaard, *Parameter study of acceleration of externally injected electrons in the linear laser wakefield regime*, Phys. Plasmas, Vol. 15, 093102, (2008).

[2] W. H. Urbanus, W. van Dijk, S. B. van der Geer, G. J. H. Brussaard, and M. J. van der Wiel, *Front-to-end simulations of the design of a laser wakefield accelerator with external injection*, J. Appl. Phys., Vol. 99, 114501, (2006).

[3] A. G. Khachatryan, F. A. van Goor, K.-J. Boller, A. J. W. Reitsma and D. A. Jaroszynski, *Extremely short relativistic-electron-bunch generation in the laser wakefield via novel bunch injection scheme*, Phys. Rev. ST Accel. Beams, Vol. 7, 121301 , (2004).

[4] A. Irman, M. J. H. Luttikhof, A. G. Khachatryan, F. A. van Goor, J. W. J. Verschuur, H. M. J. Bastiaens, and K.-J. Boller, *Design and simulation of laser wakefield acceleration with external electron bunch injection in front of the laser pulse*, J. Appl. Phys., Vol. 102., 024513, (2007).

[5] M. J. H. Luttikhof, *Theoretical investigation of external injection schemes for laser wakefield acceleration*, PhD thesis University of Twente, ISBN: 978-90-365-3071-2, (2010).

[6] www.pulsar.nl/gpt.

[7] N. E. Andreev, E. V. Chizhonkov and L. M. Gorbunov, *Numerical modelling of the 3D nonlinear wakefield excited by a short laser pulse in a plasma*, Russ. J. Numer. Anal. Math. Modelling, Vol. 13, Nr. 1, pp. 1-11, (1998.)

[8] W. van. Dijk, *Simulations and Experiments on External Injection for Laser Wakefield Acceleration*, PhD thesis, Einhoven University of Technology, ISBN: 978-90-386-2316-0, (2010).

[9] W. van Dijk, J. M. Corstens, S. B. van der Geer, M. J. van der Wiel, and G. J. H. Brussaard, *Effects of timing and stability on laser wakefield acceleration using external injection*, Phys. Rev. ST Accel. Beams, Vol. 12, 051304, (2009).

[10] A.J.W. Reitsma, *Electron bunch quality in laser wakefield acceleration.* PhD thesis, Einhoven University of Technology, ISBN: 90-386-2029-2, (2002).

[11] M. J. H. Luttikhof, A. G. Khachatryan, F. A. van Goor, and K.-J. Boller, *The effect of the vacuum-plasma transition and an injection angle on electron-bunch injection into a laser wakefield*, Phys. Plasmas, Vol. 14, 083101, (2007).

[12] C. J. Hooker, S. Blake, O. Chekhlov, R. J. Clarke, J. L. Collier, E. J. Divall, K. Ertel, P. S. Foster, S. J. Hawkes, P. Holligan, B. Landowski, W. J. Lester, D. Neely, B. Parry, R. Pattathil, M. Streeter and B. E. Wyborn, *The Astra Gemini project - A dual-beam petawatt Ti : Sapphire laser* system, Journal de Physique IV, Vol. 133, pp. 673-677, (2006).

[13] S.Y. Kalmykov, S.A. Reed, S.A. Yi, A. Beck, A.F. Lifschitz, X. Davoine, E. Lefebvre, V. Khudik, G. Shvets, P. Dong, X. Wang, D. Du, S. Bedacht, Y. Zhao, W. Henderson, A. Bernstein, G. Dyer, M. Martinez, E. Gaul, T. Ditmire and M.C. Downer, *Laser wakefield electron acceleration on Texas petawatt facility: Towards multi-GeV electron energy in a single self-guided stage.* High Energy Density Physics, Vol. 6, Issue 6, pp. 200-206, (2010).

[14] T. M. Antonsen and P. Mora, *Self-focusing and Raman scattering of laser pulses in tenuous plasmas*, Phys. Rev. Lett., Vol. 69, pp. 2204-2207, (1992).

[15] P. Mora and T. M. Antonsen, *Electron cavitation and acceleration in the wake of an ultraintense, self-focused laser pulse*, Phys. Rev. E, Vol. 53, pp. 2068-2071, (1996).

[16] F. Wojda, K. Cassou, G. Genoud, M. Burza, Y. Glinec, O. Lundh, A. Persson, G. Vieux, E. Brunetti, R. P. Shanks, D. Jaroszynski, N. E. Andreev, C.-G. Wahlström, and B. Cros, *Laser-driven plasma waves in capillary tubes,* Phys. Rev. E, Vol. 80, 066403, (2009).

[17] B. H. P. Broks, W. van Dijk and J. J. A. M. van der Mullen, *Parameter study of a pulsed capillary*, J. Phys. D: Appl. Phys., Vol. 39, pp. 2377–2383, (2006).

[18] A. J. Gonsalves, T. P. Rowlands-Rees, B. H. P. Broks, J. J. A. M. van der Mullen, and S. M. Hooker, *Transverse Interferometry of a Hydrogen-Filled Capillary Discharge Waveguide*, Phys. Rev. Lett., Vol. 98, 025002, (2007).

[19] W. Leemans and E. Esarey, *Laser-driven plasma-wave electron accelerators*, Physics Today, Vol. 62, p. 44, Issue 3, (2009).

[20] C. B. Schroeder, E. Esarey, C. G. R. Geddes, C. Benedetti, and W. P. Leemans. *Physics considerations for laser-plasma linear colliders*, Phys. Rev. ST Accel. Beams, Vol. 13, 101301, (2010).

Chapter 7

General Conclusions and Recommendations.

The main purpose of this thesis is to show the feasibility of laser wakefield acceleration (LWA) with external electron injection. A setup has been specially built to carry out these experiments. The most important parameters of the laser, the plasma and the electron source necessary to inject electrons in a plasma channel resulting in successful acceleration have been measured and discussed. For these experiments an RF-photogun is used as external electron injector.

A 3 TW laser system has been designed to perform guiding and LWA experiments. It was found that the slow capillary discharge plasma channel used is able to guide TW scale laser pulses over distances of a few centimeters. During these experiment laser pulses were focused at the entrance of the plasma channel to a spot with a $1/e^2$ radius of 40 µm. Successful guiding experiments were done for plasma densities between 0.3×10^{24} m^{-3} and 2.2×10^{24} m^{-3}. This is within range of the planned LWA experiments with externally injected electrons, that require a plasma density around $\sim 1 \times 10^{24}$ m^{-3}.

The high voltage pulse source which creates a discharge through the plasma generates a train of current pulses (3 to 4) through the plasma. During experiments better guiding properties were observed on the second current pulse compared to the first current pulse. A better laser intensity profile was found at the exit of the capillary that contains the plasma. The transmittance was higher (up to $\sim 90\%$) but most importantly, a time window for guiding of ~ 600 ns was found. This is about 10 times longer compared to the time window for guiding on

the first current pulse. Using the second current pulse results in a better, more reliable and reproducible guided laser pulse.

The electron bunches coming from the RF-photogun were focused at the position of the entrance of the plasma channel. The spot size of the electron bunch at focus is on the order of the spot size of the laser pulse at focus at the entrance of the plasma channel. The RMS radius (standard deviation) of the focus spot of the electron bunch increases from 32 μm for a 1 pC bunch to 61 μm for a 33 pC electron bunch.

Important parameters to consistently inject electrons into a plasma channel for LWA are the shot-to-shot pointing stability of the electron bunch focus and the laser focus. The shot-to-shot stability of the centre of the focused electron bunch has a RMS spread of 5 μm and the laser focus a RMS spread of 4 μm. Those shot-to-shot stabilities are well below the measured RMS radius of the electron bunch and the $1/e^2$ laser radius at focus. Therefore it can be expected that a large fraction of the electron bunch can be consistently injected into a plasma channel.

The timing jitter between laser pulse and electron bunch at the entrance of the plasma channel, which is placed at 1.14 m distance from the cathode, is estimated to be ~ 150 fs. This is on the order of one plasma wavelength for a plasma density of 1×10^{24} m^{-3}. This is sufficiently small for LWA. When injecting behind the laser pulse in the linear regime, several troughs ('buckets') may exist behind the laser pulse, which could all be used to accelerate electrons, but the energy may fluctuate from shot to shot if different buckets are occupied in different shots. With injection behind the laser pulse, the jitter therefore needs to be of the order of the plasma wavelength to be sure that the electrons are trapped in the same buckets behind the laser pulse in each shot. In the nonlinear regime, with injection in front of the laser pulse, the energy spread of the accelerated electron bunch is mainly determined by the bunch length at the entrance of the plasma channel. As long as the timing jitter is smaller than this bunch length, the fluctuations in energy from one bunch to the next after LWA will be smaller than the energy spread for a single bunch. For both regimes, linear and nonlinear, with the plasma and laser parameters considered in this thesis, 150 fs jitter is therefore considered acceptable.

Laser pulses with a central wavelength of 266 nm or 400 nm can be used to photo-emit electrons from the cathode of the RF-photogun. The charge generated by the 266 nm laser pulses shows a first and second order dependency on the laser power, while the 400 nm laser pulses only show a second order dependency. Using the 400 nm laser pulse instead of the commonly used 266 nm laser pulse has no noticeable effect on the electron bunch properties at focus such as energy, energy spread, normalized emittance and smallest possible focal spot. The intensity of both 266 nm and 400 nm laser pulses is high enough to generate tens of pC of charge which is sufficient to externally inject electrons in a LWA.

The maximum achievable electron energy from the RF-photogun during measurements was 3.71 MeV with an energy spread (standard deviation) of ~0.5% and a normalized emittance of ~2 μm. The shot-to-shot energy fluctuation (standard deviation) was 20 keV, or 0.05%. In the current experimental setup, designed to drive a linear plasma wave by a 3 TW laser pulse in a plasma with a density of 0.7×10^{24} m^{-3}, electron bunches externally injected behind the laser pulse in the plasma with an energy higher than 6 MeV are required for successful plasma acceleration. Although the RF-photogun is designed to produce 6.7 MeV, this energy could not be reached. It was found that the RF-photogun was somewhat contaminated on the inside. It is recommended to make a new cavity in order to reach an electron energy larger than 6 MeV. Adding an extra cell to the cavity of the RF-photogun may be beneficial as acceleration to an electron energy over 6 MeV will be possible while using an accelerating electric field not too close to the breakdown limit. The drawback will be that the electron bunches will be longer than in the original design, which will result in less accelerated charge. However, this will be enough to demonstrate and investigate LWA with external injection.

It has to be noted that all measured properties of the photogun are in accordance with the simulated values. In its present condition, with 3.7 MeV electron energy, the RF-photogun can be used to inject electrons into the plasma in front of the laser pulse, in the nonlinear regime. However, this scheme requires a laser pulse with an energy of ~ 20 TW to drive a nonlinear plasma wave. An upgrade of the laser system is therefore recommended. Simulations have been done for LWA with externally injected electron bunches in front of the laser pulse. The measured electron bunch parameters at 3.7 MeV were used as input parameters for these simulations. The simulations show that electrons can be accelerated to ~900 MeV with energy spread of 5%, using a ~10 cm long plasma channel with an on-axis electron density of 0.7×10^{24} m^{-3}, in combination with a 25 TW laser pulse focused on a 30 μm spot to drive the plasma wave. The accelerated charge depends on the injected charge, with a maximum accelerated charge of 1.2 pC at 10 pC injected charge.

One can generally conclude that it is feasible to inject electrons from an RF-photogun into a LWA resulting in significant electron acceleration after plasma acceleration. This opens the way for LWA experiments in which the effects of injected electron bunches, plasma parameters and laser parameters on LWA can be studied separately.

Summary

Towards external injection in laser wakefield acceleration

In laser wakefield acceleration (LWA) a plasma wave is driven by a high intensity ultra short laser pulse and the longitudinal electric fields in the plasma wave are used to accelerate electron bunches. Electrons with an appropriate kinetic energy, injected on the right phase of the plasma wave, get trapped by the plasma wave and are accelerated. This thesis investigates experimentally the feasibility of LWA with injected electron bunches produced by a radio frequency photogun.

A laser system was developed which is able to focus 3 TW pulses on a spot with a $1/e^2$ radius of 40 μm and a shot-to-shot position stability of 4 μm. Accelerating distances exceeding the Rayleigh length of the laser are achieved by preforming the plasma density profile to obtain a collimated propagation of the laser pulse through the plasma (guided laser pulse). The laser pulses are guided over centimeter scale distances through a capillary discharge plasma with an on-axis electron density of $\sim 1 \times 10^{24}$ m^{-3}. The guiding properties of the plasma channel were investigated. It is found that a second discharge current pulse through the plasma, ~1 μs after the primary discharge, improves the guiding properties considerably. The transmittance is higher (>90%), the guided laser spot is more cylindrically symmetric at the exit of the plasma channel and the time-window for guiding becomes approximately 10 times longer (~600 ns).

An RF-photogun had been purpose-built as an injector of electrons into the plasma channel. Different properties of the RF-photogun and the electron bunches produced were measured to determine the optimal settings for LWA. For an electron bunch with 10 pC charge and 3.7 MeV kinetic energy, the energy spread is 0.5% and the transverse emittance is 1.9 μm. After focusing the electron bunch at the entrance of the plasma channel by a pulsed solenoid lens, the focal spot has an RMS radius (standard deviation) of 40 μm with a shot-to-shot position stability of 5 μm. The RMS length of this electron bunch, derived from simulations, is 400 fs at focus. The arrival time jitter between laser pulse and electron bunch at the entrance of the plasma channel was inferred from earlier work to be around 150 fs in the present setup. This implies consistent temporal overlap between the laser wakefield and the injected electron bunch. The shot-to-shot stability and focal spot of the laser pulse and electron bunch at focus shows that there is always good overlap in transverse direction between the injected electron bunch, the laser pulse and the plasma channel.

Due to technical difficulties, the energy of the electrons from the RF-photogun was limited to 3.7 MeV. With this energy, the injector can serve for one particular version of laser wakefield acceleration, i.e. injection ahead of the laser pulse. Using the actually measured electron bunch parameters and simulating the injection of a 3.7 MeV electron bunch of 10 pC in front of a 25 TW laser pulse with a waist of 30 μm in a plasma with a density of 0.7×10^{24} m^{-3}, the maximum accelerated charge was found to be 1.2 pC with a kinetic energy of ~900 MeV and an energy spread of ~5%.

These results show that laser wakefield acceleration of electrons injected by an RF photogun is feasible.

Dankwoord

Na enkele jaren promotieonderzoek komt men uiteindelijk op het punt om de laatste zinnen op papier te zetten en daarmee het proefschrift te vervolledigen. Tegelijk wordt een boeiend en turbulent hoofdstuk in het leven afgesloten. Veelal gebeurt dit in de vorm van een dankwoord en ook hier is dit niet anders. Doorgaans is het dankwoord het meest gelezen onderdeel van een proefschrift. Dit is zelden te wijten aan de literaire capaciteiten van de promovendus maar veeleer aan de specificiteit van het uitgevoerde onderzoek. Ondanks het enge domein waarin een promotieonderzoek zich doorgaans bevindt, is het toch steeds een samenwerking van meerdere personen die - direct of indirect - bij het onderzoek betrokken zijn. Daarom wil ik hier nog kort de personen bedanken die de laatste jaren een belangrijke bijdrage hebben geleverd aan het tot stand komen van dit proefschrift zoals het hier nu voor de lezer ligt.

Vooreerst wil ik mijn 1^e promotor Marnix van der Wiel en copromotor Seth Brussaard bedanken voor het feit dat zij mij hebben aangesteld voor dit promotieonderzoek.

Seth, jij bent ongetwijfeld de persoon die het meest heeft bijgedragen aan dit promotieonderzoek. Ik heb onze samenwerking altijd als bijzonder aangenaam ervaren. Bij jou kon ik steeds terecht voor uitleg en discussies over het effect van het 'wakefield' op de elektronen. De valkuilen hieromtrent waren legio en er onbewust intrappen was voor mij dan bijna onvermijdelijk. Gelukkig stond jij alvast klaar om mij voor dergelijke 'putten' te waarschuwen en waar nodig mij er terug uit te helpen. In het lab heb ik ons ook altijd beschouwd als een complementair team dat samen alles uiteindelijk wel aan de praat kreeg. Het corrigeren van dit proefschrift en het omzetten naar 'deftig' Engels zijn ook grotendeels van jouw hand. Voor al deze dingen ben ik je dan ook bijzonder erkentelijk.

Marnix, ondanks het feit dat je reeds op rust bent, hebben jouw professionalisme en de snelheid waarmee gecorrigeerde versies van dit proefschrift terug op mijn bureau belandden mij steeds verbaasd. Doordat de ingang van jouw pensioen nogal vroeg in mijn promotieperiode viel, was een nauwe samenwerking spijtig genoeg slechts van korte duur. Jou opmerkingsvermogen om knelpunten te lokaliseren in theorieën en wetenschappelijk opstellingen en daar vervolgens gewiekste vragen over te stellen vond ik altijd indrukwekkend.

Mijn tweede promotor en sinds kort nieuwe groepsleider, Jom Luiten, wil ik bedanken voor het doorvoeren van de laatste correcties van dit proefschrift. Jom, jouw aanstekelijk enthousiasme, aanmoedigingen en complimentjes hebben niet enkel mijn wetenschappelijke prestaties positief beïnvloed, ik ben er ook sterk van overtuigd dat dit ook de rest van de groep ten goede komt.

Curriculum vitae

10 januari 1977	Geboren te Roeselare, België
1989-1995	Algemeen Secundair Onderwijs, Wiskunde - Wetenschappen Klein Seminarie, Roeselare, België
1995-2000	Kandidaat Natuurkunde, Katholieke Universiteit Leuven, Leuven, België
2000-2004	Zelfstandig medewerker in familiezaak, Chauffage en Sanitair Stragier, Roeselare, België
2004-2004	Technisch commercieel medewerker, De Witte Technics, Oostakker, België
2004-2006	Industrieel Ingenieur Nucleaire Technologie, Nucleaire Technieken, Xios Hogeschool Limburg, Diepenbeek, België
2005-2006	Externe Stage, Studiecentrum voor Kernenergie, Mol, België
2006-2011	Promotie onderzoek, Technische Universiteit Eindhoven, Eindhoven, Nederland, Faculteit Technische Natuurkunde, Coherentie en Kwantum Technologie groep